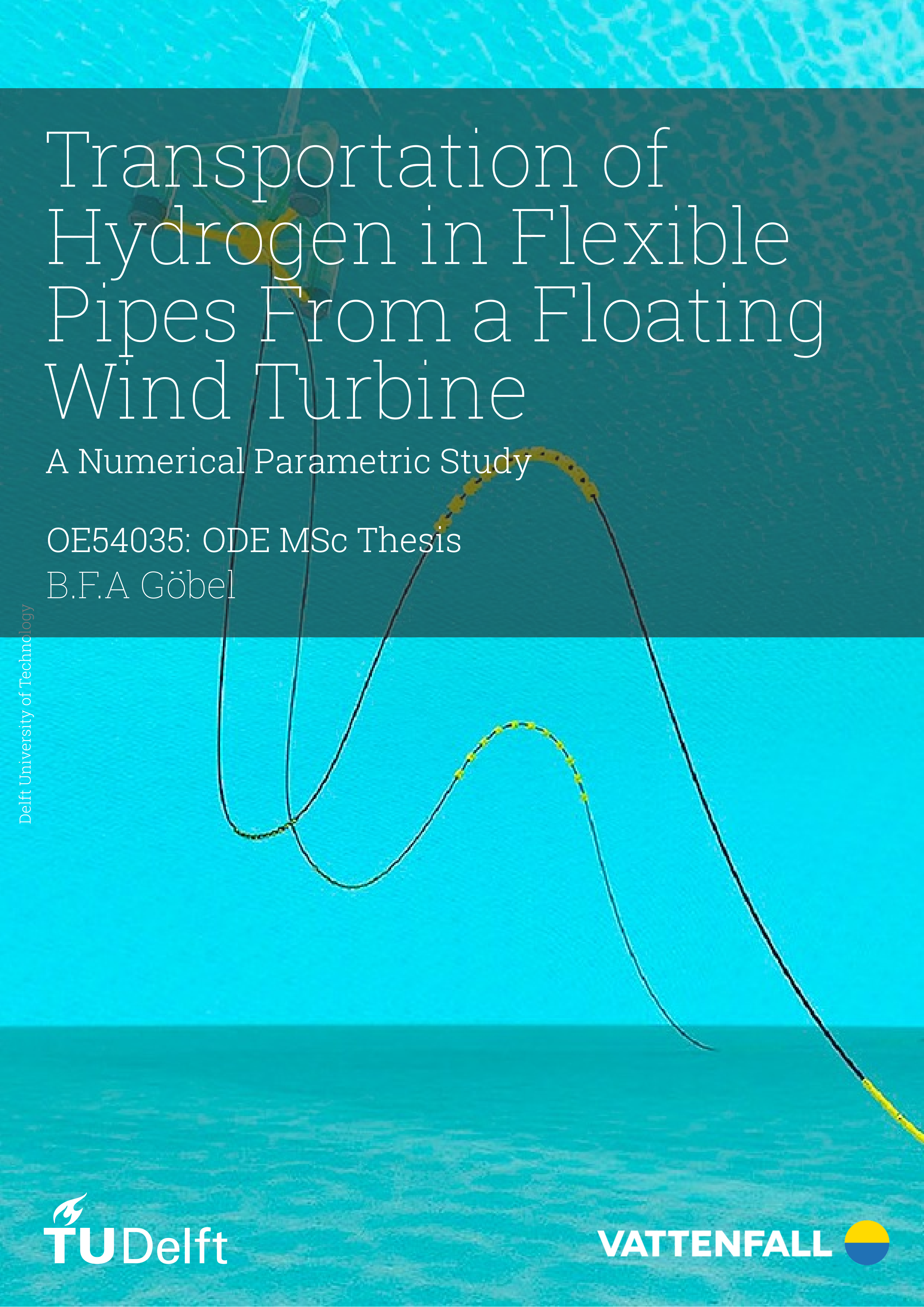

Transportation of Hydrogen in Flexible Pipes From a Floating Wind Turbine

A Numerical Parametric Study

OE54035: ODE MSc Thesis

B.F.A Göbel

Delft University of Technology

TU Delft

VATTENFALL

Transportation of Hydrogen in Flexible Pipes From a Floating Wind Turbine

A Numerical Parametric Study

by

B.F.A Göbel

Student Name	Student Number
Göbel	4683536

Thesis committee:	Dr.ir. A. Jarquin Laguna	TU Delft Chair
	Dr. M.B. Zaayer	TU Delft Committee Member
	Dr.ir. G.H. Keetels	TU Delft Committee Member
	G. Dixon	External Committee Member

Project Duration: November, 2023 - October, 2024
Faculty of Mechanical Engineering, Delft

Cover: Floating wind turbine protection systems for both inter-array and export cables by Bardot

Abstract

The increasing demand for renewable energy and the need to achieve global decarbonization goals have led the energy sector to explore remote areas where Floating Offshore Wind Turbines (FOWTs) are expected to play a significant role. These far from shore located turbines harness strong and consistent winds, but their deployment in deeper waters poses challenges. In addition, the intermittent nature of wind energy, grid congestion, and transmission losses further complicate meeting the energy demands. Combining FOWTs with offshore hydrogen production offers a promising solution by reducing reliance on electrical infrastructure. Green hydrogen, produced from renewable sources, provides a versatile and proven option for decarbonizing hard-to-abate sectors. The integration of hydrogen production directly from a FOWT presents a compelling alternative, but the transportation of hydrogen from Hang-Off Point (HOP) at the FOWT to the Termination Point (TP) at the seabed through flexible pipes requires ensuring the structural integrity under static and environmental loading.

This research evaluates the impact of various parameters in lazy wave configurations on the tension and curvature behavior of flexible pipes used for hydrogen transport in offshore wind-to-hydrogen systems, utilizing simulations performed in OrcaFlex (OF). The research shows that failure modes, tension, overbending, and compression, are only exceeded in non-optimal wave configurations, with the Minimum Bend Radius (MBR) being a more critical constraint than the Minimum Breaking Load (MBL). However, both limits are breached when compression, looping at the Touch Down Point (TDP), or collapse has already occurred, suggesting that the pipe may be overdesigned or that the lazy wave configuration represents a conservative design approach. Furthermore, research also finds that environmental factors have minimal impact on tension and curvature, with static effects contributing for 86% of total tension and 78% of total curvature. This indicates that static analysis can provide an initial configuration without the need for computationally demanding dynamic simulations, as the design limits of MBL and MBR are exceeded in similar static and dynamic scenarios. Lastly, the design of a lazy wave configuration can be simplified to three configurational parameters: a buoyant section parameter (the outer diameter of the Buoyancy Modules (BM), pitch between BMs, or the buoyant section length), the first section catenary length, and a total configuration parameter (total length or horizontal distance between the HOP and TP), since the parameters within each group exhibit similar behavior in terms of tension and curvature responses when varied individually.

Preface

This research was conducted to fulfill the graduation requirements for obtaining the degree of Master of Science in Offshore and Dredging Engineering at Delft University of Technology. The research was performed in collaboration with Vattenfall and TU Delft.

First and foremost, I would like to express my sincere gratitude to Graham Dixon, my supervisor at Vattenfall. I truly valued our meetings, which provided invaluable insights into both the approach and problem-solving strategies.

Secondly, I wish to thank Antonio Laguna for his continuous support, where his expertise greatly contributed to the devlopment of this research and the thesis process.

I would also like to extend my thanks to Michiel Zaayer for his supervision, guidance and constructive feedback throughout this project.

Next, I would like to acknowledge Geert Keetels for his role as part of my thesis committee and his interest in this work.

In addition, I would like to thank the entire Hydrogen Incubator team at Vattenfall for recognizing the importance of this research and offering me the opportunity to collaborate with such an inspiring team.

A special thanks to Olaf Otte, Matthias Dudek, and Max van Fulpen, whose support and assistance were invaluable in developing the necessary software skills.

I am also grateful to the team at NOV for their hospitality during my visit to Copenhagen and for offering real-world insights into the field of flexible pipes.

Lastly, I would like to thank my family and friends for their unconditional support throughout this journey, standing by me through all the blood, sweat, and tears.

Boudewijn Gobel
Delft, October 2024

Contents

List of Figures

List of Tables

Nomenclature

Abbreviations

Abbreviation	Definition
BM	Buoyancy Module
BS	Bend Stiffener
DCM	De-Coupled Method
DLC	Design Load Case
DPC	Dynamic Power Cable
FCM	Fully Coupled Method
FOWT	Floating Offshore Wind Turbine
HB	Hog Bend
HOP	Hang-Off Point
LC	Load Case
MBL	Minimum Breaking Load
MBR	Minimum Bend Radius
OF	OrcaFlex
RAO	Response Amplitude Operator
RNA	Rotor Nacelle Assembly
SBC	SeaBed Clearance
SB	Sag Bend
SSC	Sea Surface Clearance
TDP	Touch-Down Point
TLP	Tension-Leg Platform
TP	Termination Point
ULS	Ultimate Limit State
VIV	Vortex-Induced Vibrations
6DoF	Six Degrees of Freedom

Symbol	Definition	Unit
A	Surface area pipe	m^2
AI	Axial stiffness pipe	MN
C	Maximum curvature	rad/m
$C_{A,BM}$; $C_{A,BS}$; $C_{A,pipe}$	Added mass coefficients Buoyancy Modules; Bend stiffener; pipe	-
$C_{D,BM}$, $C_{D,BS}$, $C_{D,pipe}$	Drag coefficients Buoyancy Modules; Bend Stiffener; and pipe	-
D_{base}	Diameter base of Bend Stiffener	m
$C(p,v)$	Damping load	N
D_{tip}	Diameter tip of Bend stiffener	m

Symbol	**Definition**	**Unit**
d	Water depth	m
d_{BM}	Pitch between Buoyancy Modules	m
E	Energy content hydrogen	kWh/kg
EI	Bending stiffness pipe	kNm^2
E_{BS}	Young's Modulus Bend stiffener	GPA
F_1; F_2; F_3	Net force of part pipe 1; 2; 3	N
F_b	Buoyancy force of pipe or Buoyancy Module	N
F_g	Gravitational force of pipe or Buoyancy Module	N
$F(p,v,t)$	External load	N
$F_{subm,BM}$; $F_{subm,pipe}$	Net force of submerged Buoyancy Modules; submerged pipe	N
$F_{subm,tot}$	Net force of total submerged system	N
F_{thrust}; F_{drag}	Forces at nacelle thrust; drag	N
g	Gravitational constant	m/s^2
h	Vertical distance from Hang-Off Point to seabed	-
H_s & $H_{s,5-year}$; $H_{s,50-year}$	Significant wave heights at rated and cut-out wind speeds & 5-; 50-year return period	m/s
$h_{SB,B}$	Absolute vertical distance between Sag Bend and seabed	m
$h_{SB,E}$	Absolute vertical distance between furthest located Buoyancy Modules in section 2 and seabed	m
$h_{SS,D}$	Absolute vertical distance between Hog Bend and sea surface	m
ID_{pipe}	Inner diameter of pipe	m
$K(p)$	Stiffness load	N
L_1; L_2: L_3	Length of section pipe 1; 2; 3	m
$L_{3,cat}$	Catenary section part of L_3	m
L_{BM}	Length of Buoyancy Module	m
L_{BS}	Length of Bend Stiffener	m
L_{ST}	Static horizontal section part of L_3	m
L_{tip}	Length tip of Bend Stiffener	m
L_{total}	Total length of the pipe	m
m_{aux}	Mass of auxiliary components	kg
m_{BM}	Mass Buoyancy Module	kg
$m_{BM,H}$	Hardware mass Buoyancy Module	kg
m_{pipe}	Mass of pipe	kg
$M(p,a)$	Inertia load	N
$\dot{m}_{\mathrm{H_2}}$	Mass flow rate hydrogen	kg/s
n_{BM}	Number of Buoyancy Modules	-
η	Energy efficiency conversion to hydrogen	-
OD_{BM}	Outer diameter of Buoyancy Module	m
OD_{BMe}	Equivalent outer diameter of distributed buoyancy	m
OD_{pipe}	Outer diameter of pipe	m
P	Wind turbine capacity	MW
ρ_{BS}	Density Bend Stiffener	te/m^3
ρ_{BM}	Density of Buoyancy Module	kg/m^3
ρ_{sw}	Density of seawater	kg/m^3
μ_{SB}	Seabed friction coefficient	-
T	Draft semi-submersible	m
T_e	Maximum effective tensions	kN
T_p	Peak wave period	s
t_{tip}	Thickness tip of Bend Stiffener	m
U_{1-year}; U_{5-year}; $U_{50-year}$	Current speeds 1-; 5-; 50-year return period	m/s

Symbol	**Definition**	**Unit**
v_{BS}	Poisson ratio Bend Stiffener	-
V_{BM}	Volume of a Buoyancy Module	m^3
$V_{cut-out}$; V_{rated} & V_{5-year}; $V_{50-year}$	Wind speeds at cut-out; rated & 5-; 50-year return period	m/s
$V_{displaced}$	Displaced volume object	m^3
w_e	Equivalent specific mass per unit length of distributed buoyancy	kg/m
$w_{pipe,dry}$	Mass per unit length of pipe in air	kg/m
$w_{pipe,wet}$	Mass per unit length of pipe in seawater	kg/m
x_{TP}	Horizontal distance between the Hang-Off Point and the Termination Point	m
γ	Peak enhancement factor	-

1

Introduction

This chapter provides an overview of the research background in section 1.1, followed by the research motivation and objectives subsequently detailed in sections 1.2 and 1.3. It then briefly discusses the research approach in section 1.4 and outlines the scope in section 1.5. The structure of the report is delineated in section 1.6.

1.1. Background

In the past two centuries, the global population has increased significantly, growing from one billion in 1800 to over 8 billion today [1]. This exponential growth has led to a corresponding rise in energy demand, which is anticipated to increase by 50% by 2050 compared to 2020 [2]. To meet the objectives of the Paris Agreement — limiting global temperature rise this century to well below 2°C, with efforts to limit it to 1.5°C [3] — significant changes in the energy landscape are essential. As of 2020, fossil fuels accounted for 83% of global energy consumption, while renewables comprised only 13% [4]. To achieve net-zero fossil fuel use by 2050, renewable energy production needs to increase six- to eight-fold, resulting in renewables making up two-thirds of global energy consumption and 85% of power generation. This would result in renewables contributing to 90% of the climate mitigation needed to meet Paris Agreement targets [5].

Onshore renewable options are increasingly constrained by space limitations and public opposition, driving a shift towards offshore energy sources, particularly wind and ocean energy. Offshore wind is a key player in this transition, with a projected compound annual growth rate of 31% to 2027 and 12% to 2032. Offshore wind energy offers significant advantages over onshore wind, including stronger and more stable wind speeds, with turbines being larger and located where visual and noise impacts are minimal. However, these benefits come with increased costs related to marine foundations, grid integration, and more complex installation and maintenance processes [6, 7]. Despite these challenges, the sector is expected to grow rapidly, reaching an estimated 450 GW of capacity by 2030 [8].

The offshore wind industry is now venturing into more remote sea areas to explore new wind farm locations. Floating Offshore Wind Turbines (FOWTs) represent a crucial advancement in renewable energy, addressing the limitations of bottom-fixed wind farms in deep waters. Unlike traditional nearshore installations, FOWTs can be deployed in waters deeper than 50 meters, where stronger and more consistent wind speeds significantly enhance energy production, with examples showing higher capacity factors than in shallower waters [9]. Approximately 80% of the world's potential wind energy resources lie in these deeper waters [10, 11]. This flexibility allows FOWTs to be positioned farther offshore, minimizing visual and noise impacts [12], making them crucial due to their scalability and efficiency. Although the global floating offshore wind capacity is growing, commercialization is expected after 2027 [8]. The development of FOWTs presents technical and logistical challenges, including the need for optimized mooring systems, Dynamic Power Cables (DPC), and floating structures [13, 14]. Despite these challenges, FOWTs are expected to play a significant role in meeting future energy demands, with projects like Hywind Scotland and WindFloat Atlantic highlighting their potential [15].

While wind and solar power currently contribute a small fraction to global energy, their use is projected to grow significantly by 2050 [16]. However, the intermittent nature of wind power presents challenges such as grid congestion and the need for energy balancing, influenced by geographical factors [17].

Additionally, hard-to-abate sectors, like transportation, high-temperature industrial, and heavy industry processes may not be fully served by electrification alone, as they are difficult or even impossible to electrify. Green hydrogen, produced from renewable sources, offers a versatile solution by converting renewable electricity into a usable form for diverse applications. Hydrogen is already widely utilized in industries like refineries and ammonia production, but primarily in the form of grey hydrogen, which relies on fossil fuels. However, green hydrogen has demonstrated its viability as a substitute for fossil fuels in hard-to-abate sectors, exemplified by the steelmaking process in the HYBRIT (Hydrogen Breakthrough Ironmaking Technology) test facility. This initiative, part of a fossil-free steel project initiated by Vattenfall and other companies, has showcased significant potential transformations in steel production through the substitution of green hydrogen for coal [18]. In addition, the transportation industry has also seen changes where the replacement of fossil-fueled buses with hydrogen-fueled buses shows comparable driving ranges while there are no harmful emissions [19]. This transition to green hydrogen is essential for decarbonizing existing applications, making it crucial for areas where electricity alone cannot meet decarbonization goals [20].

Floating offshore wind presents a unique opportunity to produce green hydrogen. Offshore hydrogen production, particularly when combined with floating wind turbines, can address key challenges associated with renewable energy, such as grid congestion and transmission losses over long distances. Studies show that offshore hydrogen production, with transportation via pipelines located over 100 km from the coastline, is economically cheaper than onshore hydrogen production [21]. This approach reduces reliance on extensive electrical infrastructure and minimizes energy losses, offering a versatile energy carrier for the storage and transport of renewable energy, important for meeting increasing energy demands and adhering to the Paris Agreement's goals. Despite being in the early stages, the integration of floating wind and offshore hydrogen technologies presents a promising path toward a more resilient and sustainable energy system.

1.2. Research Motivation

The evolution of FOWTs represents a significant technological shift, driven by the need to harness stronger and more consistent winds located in deeper waters. This shift requires advanced DPCs that must withstand complex and fluctuating loading. As offshore developments move farther from shore, the increased costs associated with electrical infrastructure make offshore hydrogen production, transported via pipelines, economically more viable. Although FOWTs are expected to commercialize after 2027, research on their integration with hydrogen production units remains limited. Offshore green hydrogen production, using electricity generated by FOWTs, offers a promising solution to decarbonize sectors that are difficult to electrify. However, the technical feasibility of transporting hydrogen through flexible pipelines, especially in a floating wind-to-hydrogen setup, remains unexplored.

This research is motivated from the importance of flexible pipes in offshore applications, particularly in the context of the energy transition and increasing demand for renewable energy. As the energy sector advances toward deeper waters for offshore wind and hydrogen production, the need for robust and reliable umbilical systems becomes more critical. These systems are essential for maintaining connections between floating platforms and seabed installations, ensuring stability in dynamic environments. Given the anticipated commercialization of wind-to-hydrogen systems, it is important to assess the viability of the transportation of the hydrogen.

In the oil and gas industry, flexible pipes and their configurations have been extensively studied across various applications. However, there remains a gap in understanding the impact of various configurations on the design of flexible pipes. Existing research often focuses on case-specific scenarios with limited examination of the effects of various configurations in both static and dynamic environments. Additionally, there is a lack of research incorporating the transportation of hydrogen as an internal fluid in flexible pipes. Conversely, the floating wind industry has produced numerous studies aimed at optimizing DPC configurations to reduce global loads and prevent fatigue failure [22, 23]. This research bridges the knowledge from flexible pipe applications in the oil and gas sector with FOWT's, specifically focusing on hydrogen transport. This research seeks to enhance understanding of various lazy wave configurations of flexible pipes in wind-to-hydrogen applications under both static and dynamic conditions. Therefore, there is a necessity for a parametric study to examine the influence of different geometrical parameters on the design of flexible pipes

1.3. Research Objectives

The objective of this research is to determine how variations configurations influence the structural response behavior of the lazy wave configuration for flexible pipes. This is done through a parametric study of decision parameters influencing the global configurations, with a focus on evaluating system performance in terms of constraints, specifically tension and curvature response behavior. The research aims to provide insights into various configurations and their corresponding effects of specific constraints, which can serve as a basis for arbitrary scenarios. The main research question is:

What impact do parameters of lazy wave configurations have on the tension and curvature of flexible pipes connected to a semi-submersible FOWT in hydrogen applications?

To answer this research question, sub-research questions have been formulated as follows:

> *What is the difference in response in static and dynamic environments?*
>
> *What are the most relevant geometrical parameters influencing the configuration and how do they impact the response?*
>
> *What is the effect of different water depths on the variations of these parameters?*

1.4. Approach

To address the research question and its sub-questions, this section outlines the approach adopted. The analysis is conducted exclusively through numerical simulations using the commercially available software, OrcaFlex (OF), a leading tool in offshore dynamic applications. A pipe designed for hydrogen applications but not yet tested is utilized, provided by a pipe manufacturer. The configuration is determined based on rules of thumb from DPC studies that focus on minimizing tension and curvature. These recommendations specify the proportions of the total length as well as the non-buoyant and buoyant sections to establish the reference configuration. A single omni-directional metocean condition models the dynamic environment, simulating an irregular sea state combined with de-coupled aerodynamic loading and depth-varying current speeds, based on in-house data from Vattenfall. Water depths are varied across 200m, 400m, and 600m. The parametric study, focusing on configurational parameters, isolates single parameter changes to clearly understand their individual impacts. The effects are evaluated based on global tension and curvature metrics.

1.5. Scope

To scope of this research requires several assumptions to simply the numerical model. These are as follows:

- **FOWT model:** The model uses a pre-provided semi-submersible design. FOWT substructures are classified into three main types based on its stability: semi-submersible, spar, and Tension-Leg Platform (TLP). The spar-type foundation achieves stability by lowering the buoyancy center, while the TLP utilizes tensioned anchors to the seabed. The semi-submersible combines buoyancy control and anchored mooring, chosen for its widespread research, technological readiness, and global market presence.
- **System Configuration:** Offshore wind-to-hydrogen setups can be centralized, decentralized, or semi-centralized. A centralized configuration involves a single hydrogen production unit within the wind farm, whereas decentralized involves individual units per FOWT. Semi-centralized systems link multiple production units to clusters of turbines. The adoption of a decentralized offshore wind-to-hydrogen system is driven by its benefits and early developmental stage. This configuration eliminates high-voltage infrastructure, streamlining the system to focus solely on hydrogen transport via flexible pipes. Furthermore, it facilitates the easily scalable expansion of individual FOWTs.
- **Pipe configuration:** This research exclusively examines the lazy wave configuration, recommended for its effectiveness in DPC applications connected to FOWTs. This configuration is preferred due to its capability to decouple the motion of the floater from connection points. It adeptly

manages axial and bending stresses, particularly at the Hang-off Point (HOP) and Touch Down Point (TDP), facilitated by the use of Buoyancy Modules (BMs).

- **Failure Modes:** Focus is on mechanical failure modes including tension, compression, overbending, and collapse, rather than thermal, chemical, or accidental failures. Fatigue is not considered due to the multi-layered structure's complex interactions, where simplified beam theory is inadequate.
- **Operational and Environmental Conditions:** Lastly, the emphasis is on operating conditions and the Ultimate Limit State (ULS), which describes the maximum load a pipeline can endure without structural failure. This ensures that the pipe withstands severe loading during its operational life. Environmental considerations specifically exclude Vortex-Induced Vibrations (VIV) and marine growth. VIV, primarily caused by currents, can lead to oscillatory movements and potentially induce fatigue due to frequency lock-in. Marine growth alters the pipe's and BM's weight and hydrodynamic characteristics, affecting the pipe's configuration from its initial configuration.

1.6. Outline of the Report

To address the research question, this report is organized as follows. Chapter 2 provides a review and identifies suitable design considerations for flexible pipes used as umbilical systems. It explores current technologies in non-bonded flexible pipes, discusses possible configurations, and applies relevant ancillaries. This chapter also reviews various loads on pipe structures and explores hydrogen transportation through pipelines. The selection of components used throughout the research is elaborated on.

Chapter 3 details the methodology for the numerical simulations of the parametric study. It begins with an overview of the design conditions and processes, including design stages and accompanying failure modes, followed by design constraints and the theoretical foundations of all modeled components. A reference case study is then considered, forming the preliminary basis of the research. Subsequently, the numerical software is analyzed, integrating several simplifications and input requirements to finalize its base case scenario. This sets the foundation for the parametric study, where evaluation criteria for static and dynamic analysis are noted, concluding with the setup for parameter decisions at water depths of 200m, 400m, and 600m, and finalizing with the sensitivity analysis setup.

Chapter 4 presents the research results, discussing the impact of each parameter individually based on static and dynamic analyses and their effects at different water depths, followed by its sensitivity.

Finally, the discussion and limitations are addressed in chapter 5, followed by the conclusions and recommendations listed in chapter 6.

2

Flexible Pipe Design

This chapter provides an overview of the design and technological aspects of flexible pipes and the selection of aspects covered in this research. It begins with a detailed exploration of flexible pipe technology in section 2.1, covering the characteristics of non-bonded and bonded structures, the cross-sectional components that contribute to their functionality, and the selection of pipes used in this research. Section 2.2 examines various umbilical configurations, highlighting the advantages and limitations of different designs and noting the selected configuration. Additionally, section 2.3 describes the essential ancillary components required for flexible pipe systems, along with the selection of these components. Section 2.4 discusses the loads that a pipe structure is subjected to, detailing the selections made for this research. Finally, the chapter concludes with a discussion and on hydrogen transportation through flexible pipes in section 2.5.

2.1. Flexible Pipe Technology

Conventional steel pipelines, despite their maturity, face challenges in flexibility, corrosion protection, and installation costs, leading to the development of offshore flexible pipes. These pipes can be bent to small radii without losing mechanical strength and can be installed using the reel method, reducing overall costs [24]. In moderate and deep waters, flexible pipes are often the only viable solution. Since the 1980s, their use has expanded in offshore oil and gas exploration, now comprising over 80% of marine risers [25]. Dynamic flexible pipes are versatile, functioning as risers, flowlines, and jumpers, and are particularly useful for routing in congested subsea layouts, thus lowering installation costs. Its characteristics, types of structures, cross-sections, protection, and selection will be discussed.

2.1.1. Characteristics

Flexible pipes are crucial in riser applications due to their unique multilayered design, which offers lower bending stiffness compared to rigid steel risers. This allows them to accommodate smaller radii of curvature while maintaining the same pressure capacity. Their ability to endure significant deformations under various loads, such as ocean currents, waves, VIV, and vessel movement, makes them ideal for offshore production [26]. Flexible pipes are preferred over steel pipes for their compliant structure, enabling permanent connections between floating vessels and subsea installations, and their ease of transport and installation due to prefabrication in long lengths stored on reels [27]. The global strength of flexible pipes includes low bending stiffness, high volume stiffness and strength for containing fluids under high pressure, and high axial stiffness for deep-water deployment. However, these advantages are balanced by lower torsional and axial compressive stiffness and strength [27].

2.1.2. Non-bonded and bonded structures

Flexible pipes are composed of multiple layers, with the structure classified as either bonded or un-bonded. In un-bonded pipes, layers can slide independently, while bonded pipes have layers attached into a single structure, forming an elastomeric matrix [27]. Un-bonded structures, characterized by low bending stiffness, high axial stiffness, and high volume stiffness, are ideal for flexible risers, due to their ability to withstand significant flexure while maintaining axial strength and pressure integrity [28] [29]. Bonded pipes, known for their flexibility, small bend radius, and reliable couplings, are well-suited for confined spaces and customizable sections. However, they typically have lower axial and crush resistance, are prone to gas decompression, face thermal and chemical limitations, and require joints due to segment length constraints [30]. Appendix A.1 summarizes the advantages and disadvantages of both structures, while for this research the non-bonded flexible pipes are used.

2.1.3. Cross-section of non-bonded pipes

Each layer within a flexible pipe serves a specific function, with variations in composition to meet different pipeline requirements and accommodate manufacturer variations. The number of layers varies with the pipe's diameter and pressure rating, with up to 20 layers in high-pressure scenarios. The region between the outer sheath and internal pressure sheath is called the annulus, and the presence of a carcass determines whether the pipe has a rough or smooth bore. From the innermost to outermost layer in non-bonded pipes, as depicted in figure 2.1, the components include:

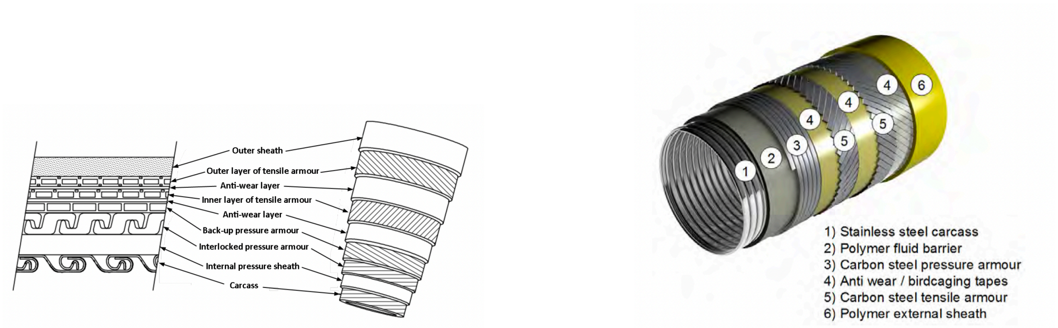

(a) Detailed cross-section of a non-bonded flexible pipe [27]

(b) Cross-section of a non-bonded flexible pipe, courtesy of GE Oil & Gas

Figure 2.1: Cross-sections of non-bonded flexible pipes

- **Carcass:** Helically wound interlocked wire, usually stainless steel, prevents inner sheath erosion and withstands external seawater pressure [24].
- **Polymer Layer:** Provides flexibility and acts as a fluid barrier, supported by steel armor and polymer to maintain low bending stiffness.
- **Internal Pressure Sheath:** Cylindrical polymer sheath, typically made from materials like HDPE, XLPE, PA, or PVDF, transfers internal pressure and seals the medium [24].
- **Pressure Armor Layer:** Steel or carbon steel section withstands internal and external pressures [24].
- **Tension Armor Layer:** Helically wound steel wire, resists axial tension and maintains torsional balance [24].
- **Anti-Wear Layer:** Low-friction polymer tape reduces wear and friction between metal layers [24].
- **Insulation:** Provides thermal insulation, if necessary.
- **Outer Sheath:** Similar to the internal sheath, seals against seawater and resists external pressure.

2.1.4. Protection methods

Pipeline design is influenced by fluid properties, including corrosion potential, density, gas diffusion, and internal friction. Materials like Super Duplex or AISI 316 are often used to resist corrosion. Fluid density changes can alter riser configurations, while gas diffusion in un-bonded pipes requires annulus ventilation to prevent pressure buildup. High-frequency vibrations, especially in rough bore pipes, pose challenges like noise and vibration. Pressure primarily determines armor wire dimensions, and temperature dictates polymer material selection. In instances transportation of liquids, vibrations induced by two-phase slug flow must also be considered [27, 31], however, in the transportation of purely gaseous hydrogen, slug flow is less common. For this research, a constant density, pressure and temperature is considered, where vibrations and slug-flow are left out of the scope. External corrosion risks, requiring careful material selection and protective measures like inhibitors, coatings, or cathodic protection. These measures are vital for maintaining pipeline integrity and uninterrupted operations [32].

2.1.5. Selection of the pipe

For the pipe that is being used in this research, a collaboration with NOV has been achieved. NOV is a worldwide company that produces flexible pipes for various offshore applications. Using in-house software specifically designed to combine various materials and layers in different cross-sectional configurations, a flexible pipe design has been constructed. This pipe is optimized to have as few layers as possible with low grades of strength. Testing of these materials still has to be performed to verify their applicability with hydrogen. The input parameters for this software require the water depth, design temperatures, and pressures. These design pressure and temperature of the pipe are determined by the output of the electrolyzer.

2.2. Umbilical System Configurations

The various possible configurations for umbilicals are listed in this section, followed by the configuration selected for this research.

2.2.1. Overview of umbilical configurations

In the current industries, the configurations are chosen based on factors like water depth, production unit movements, environmental conditions, and interference issues [27]. The simplest configuration is the free-hanging catenary, which is cost-effective but prone to fatigue and compression at the TDP. More complex configurations, like lazy and steep wave, incorporate buoyant sections to mitigate these issues but are more challenging to install. The selection of an optimal riser configuration depends on several factors, including geometry, structural integrity, and cost [33]. The available configurations, shown in figure 2.2, and their applications are summarized in table 2.1.

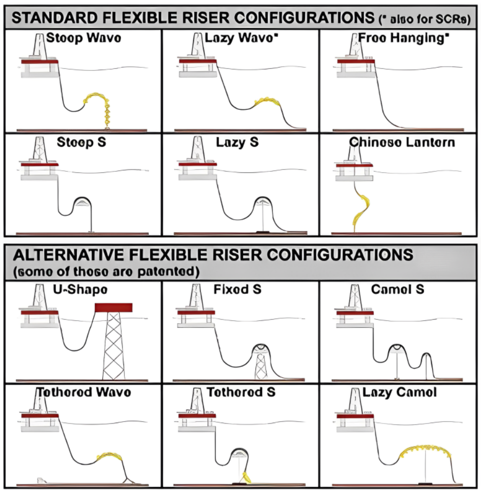

Figure 2.2: Flexible Riser System Configurations [34]

Risers and DPCs, denoted as umbilicals, have been extensively studied, particularly focusing on configurations such as the lazy wave and catenary shapes. [35] developed a matrix ranking riser configurations based on environmental conditions, installation, and cost, shown in appendix A.1. The lazy wave configuration is favored for reducing stress at critical points like the HOP and enhancing fatigue resistance, effectively decoupling substructure motions from the TDP [36]. [37] mentions that structural loading originates from the ocean waves combined with the intricate movements of the vessel. The study by [38] concluded that internal pressure led to a decrease in axial tension. [38] noted that internal pressure reduces axial tension, while [39] highlighted the minimal impact of current conditions on riser behavior, emphasizing the importance of optimal buoyancy module length. In contrast, the catenary configuration, though simpler and cost-effective, faces higher stress concentrations, making it less ideal in harsh environments due to its susceptibility to overbending at the TDP and significant loads at the HOP [40]. The lazy wave configuration is generally preferred for deepwater scenarios, as it ensures consistent stress distribution and better performance in varying sea states [39].

Table 2.1: Summary of riser configurations[27]

Configuration	Complexity	Typical Applications and Properties
Free Hanging Catenary	Low	Simple, low-cost, minimal infrastructure. Suitable for low to moderate motions with mild wave climate. Vulnerable to buckling at TDP, sensitive to fluid density changes.
Lazy Wave	Medium	Uses Buoyancy Modules (BM) to decouple motions. Reduces top tension and TDP loads. Suitable for larger substructure motions in more extreme conditions. Wave shape sensitive to current, waves and marine growth.
Steep Wave	Medium	Similar to Lazy Wave, but more compact. Vertically connected to seabed. Less seabed interference, higher tension at the base.
Tethered Wave	Medium	Variation of Lazy Wave with a tether anchor. Controls TDP movement, used when TP is beneath the platform. Moderate to large substructure motions, some seabed restrictions.
Lazy S	High	Subsea buoy for minimal interference; when BM are undesirable. Buoy instability due to riser weight and water absorption. Suitable for constrained spaces and multiple risers.
Steep S	High	Similar to Lazy S, but more compact. Riser interference expected. Used where seabed space is limited. Vertically placed into riser structure.
Chinese Lantern	High	Straight riser with a curved middle section due to BM. Most challenging configuration, requires precise computation. Unstable and achievement is difficult.
Vertical Tower and Jumper	Very High	Combines steel and flexible pipes. Used in deep water with moderate wave loading. Can facilitate disconnection. Low top tension, compact design. Thermal insulation required.
Dynamic Jumper	Low	Connects closely positioned platforms, vessels, or substructures. Absorbs relative motions and simple design

2.2.2. Selection of configuration

For flexible pipe applications in FOWT, configurations must meet specific demands, including suitability for deep waters, prevention of large stresses at critical points, allowance for FOWT offset, and cost-effectiveness. The most suitable configurations are the lazy wave and the catenary, which reduce stresses at the HOP due to buoyant elements and accommodate for offset. However, the downside of the lazy wave configuration is that it is not the most cost-effective solution due to the pricing and installation costs of the ancillary components. Consequently, while the catenary configuration may be suitable for less demanding applications, the lazy wave configuration is generally preferred for deepwater scenarios for both pipes and DPCs. Given that lazy wave configurations are currently being deployed for FOWT in practice, this research focuses on the lazy wave configuration.

2.3. Umbilical Ancillaries

The main ancillaries for an umbilical configuration are provided, followed by the selection of ancillaries.

2.3.1. Overview of umbilical ancillary components

Flexible pipe systems require several key auxiliary components. For visualizations of components, see appendix A.2.

- **End Fittings**: These are crucial for securely anchoring and sealing each layer of the flexible pipe, ensuring structural integrity. At the interface, the bending stiffness is significantly pronounced. End fittings are custom-designed to withstand applied loads, generally stronger than the pipe itself, and are made from materials like AISI 4130 steel. Key design aspects include maintaining tolerances, appropriate filling techniques, ensuring the correct functioning of annulus vent ports, and utilizing anode clamp designs for corrosion prevention. [41]
- **Bend Stiffeners (BS) and Bellmouths**: These components prevent overbending at critical points, particularly near the HOP. BS, made from polyurethane, provide smooth load transitions and are preferred for high-motion vessel applications. Bellmouths, typically made of steel, serve a similar function. [41]
- **Bend Restrictors**: Positioned at the top and bottom connections, these restrictors prevent excessive bending, especially at vulnerable points like the riser base. Made from hard plastic or steel, they are crucial for controlling tension and shear loads. [41]
- **Buoyancy Modules (BM)**: These modules shape the umbilicals configuration. They consist of syntactic foam within a durable polymer casing, clamped individually to the riser, typically two or three times the outer diameter of the pipe. Design considerations include water depth and service life to prevent water absorption and maintain the its configuration. [42]
- **Annulus Venting System**: Over time, fluids transported through the pipe can diffuse into the annulus (e.g., water, CO2, and H2S), potentially causing corrosion, fatigue, or hydrogen-induced cracking and sulfide stress cracking in steel. This system prevents gas buildup, which could lead to pressure collapse and pipe failure. The venting mechanism ensures the safe release of gases, protecting the structural integrity of the pipe. [41]
- **Riser Bases**: Riser bases connect flexible risers to flowlines and support subsea buoy systems. The type of riser base, whether gravity-based or anchored, depends on the applied loads and soil conditions. [41]

2.3.2. Selection of ancillary components

Since the ancillaries focusing on the end fitting and annulus venting system are primarily concerned with material selection, they are beyond the scope of this research. The focus here is on designing the dimensions of the BM and BS to accommodate a suitable configuration. The riser base is specified as the termination point and is also not investigated further.

2.4. Load Analysis of Umbilicals

An overview of different types of loading on umbilicals is provided, followed by an examination of the selected loads considered for the flexible pipe structure.

2.4.1. Types of loading

The flexible pipe is subjected to various loads during its lifetime, including gravity, buoyancy, waves, currents, hydrostatic pressure, hydrodynamic drag, added mass, marine growth, and VIV. These loads are crucial for ensuring structural integrity, as illustrated in figure 2.3.

- **Gravitational and Buoyancy Forces**: Gravity imposes significant axial stresses, particularly at

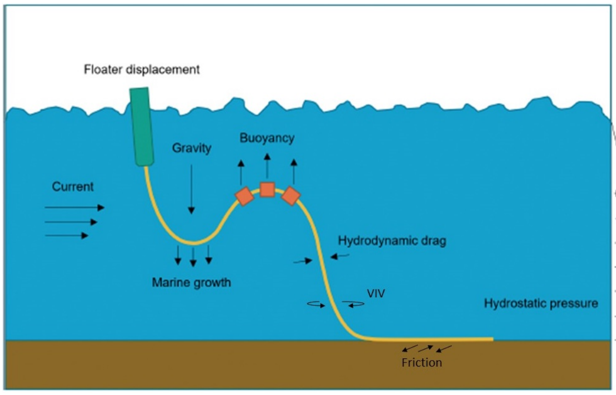

Figure 2.3: Loads on riser structure [43]

the HOP, influencing the pipe's load distribution and geometry. Buoyancy, provided by the pipe and BM's, counteracts gravity and contributes to the formation of the Hog Bend (HB) and the Sag Bend (SB). The net force on the submerged pipe is summation of gravity and buoyancy forces of pipe and BM.

- **Wave Loads**: Waves impact the dynamic behavior of structures. Realistic ocean wave conditions are modeled using a superposition of regular waves to represent irregular sea states, employing the JONSWAP spectrum. Waves exert oscillatory forces with important parameters being wave height, period, and directionality. [44, 45]
- **Current Loads**: Currents contribute to hydrodynamic drag, similar to waves. These loads vary with depth and are influenced by both tidal and wind-generated currents. In the absence of empirical data, profiles are modeled using empirical or theoretical methods, taking into account depth-dependent variations. Important parameters include current speed and direction. [44]
- **Hydrostatic Pressure**: Hydrostatic pressure increases linearly with depth, exerting compressive forces on the pipe. This pressure is must be accounted for to prevent collapse. The collapse limit defines the maximum allowable depth beyond which the pipe could fail due to external pressure.
- **Hydrodynamic Drag and Added Mass**: Hydrodynamic forces from waves and currents generate drag and added mass effects on the pipe. These forces are typically estimated using the Morison equation, which incorporates drag, inertia, and Froude-Krylov forces. Calibration of these coefficients ensures accurate load predictions. [46, 47]
- **Marine Growth**: The accumulation of marine organisms over time changes the pipe's weight and geometric shape, affecting its hydrodynamic characteristics and load distribution. [44]
- **Vortex-Induced Vibrations (VIV)**: VIV occurs when alternating vortices shed from the pipe, inducing vibrations. When the vortex shedding frequency aligns with the natural frequency of the pipe, lock-in occurs, leading to resonance and amplified oscillations. These oscillations increase the risk of fatigue failure. [47]
- **FOWT Displacement**: The motion of the FOWT (surge, sway, heave, roll, pitch, yaw) is driven by hydrodynamic and aerodyanmic forces and influences the pipe through its connection point at the HOP. Prediction of the six degrees of freedom (6DoF) is important for simulating the pipe's dynamic response
- **Friction**: Continuous interaction between the pipe and the seabed results in frictional loading, which can lead to wear and tear over time. This friction arises from the pipe's movement under environmental forces, with the severity influenced by both the seabed's composition and conditions.

2.4.2. Load considerations and selection

The loadings discussed in present multiple challenges to pipe structure, requiring careful design and material selection. Gravitational forces induce axial stresses, while buoyancy modules are designed to counteract these stresses without increasing stress concentrations. An increasing hydrostatic pressure with depth challenges structural integrity under compressional loads. Dynamic stresses from wave and current loads necessitate robust designs, especially due to irregular wave patterns and depth-dependent current profiles. Hydrodynamic drag and added mass effects demand coefficient selection for effective stress management. Additionally, the motion of the floating platform, influenced by six DoF, is integral to the overall design and the friction is a continuous factor at the contact of seabed. For simplification, certain loads were excluded from the design considerations. Marine growth, which alters the structure's weight, shape, and hydrodynamic characteristics over its lifetime, was omitted due to its gradual impact, considered minor within the context of a single operational load case. Similarly, VIV, while important in fatigue analysis, involves extensive computational studies and are beyond the scope of this research.

2.5. Hydrogen Transportation

This section provides an overview of the challenges associated with hydrogen transport through flexible pipes and addresses considerations related to the properties of hydrogen.

2.5.1. Challenges of transportation of hydrogen

Hydrogen transportation via pipelines presents several challenges due to its unique physical properties, such as low density, high compressibility, and low viscosity. The low density of hydrogen necessitates larger volumes or additional risers for equivalent energy storage or transport, which not only complicates infrastructure and increases costs [48] but also affects the buoyancy characteristics of the system. In wind-to-hydrogen scenarios, space limitations require optimized sizing solutions. High compressibility enhances storage and transport efficiency but leads to significant pressure variations, affecting other properties like density and viscosity with changing pressure and temperature [49]. While low viscosity reduces frictional losses and improves transport efficiency [50], it also raises the risk of flow-induced vibrations and potential erosion within the pipeline [51]. Additionally, hydrogen's high diffusivity and flammability present safety concerns, requiring the use of robust materials and stringent safety measures to prevent leaks and ignition. These factors demand careful design and material selection to ensure the safe and efficient transport of hydrogen in pipelines.

Gas flow in pipelines is primarily driven by pressure differences, with internal friction leading to pressure drops influenced by factors such as pipe roughness and length. The general flow equation, which accounts for these variables, accounts for accurately calculating pressure drops in gas pipelines [52]. For hydrogen transport, determining the minimum pipeline diameter involves balancing pressure drops, velocity limits, and maximum flow rates [53]. The total pressure drop is affected by friction, elevation changes, and delivery pressure. Hydrogen's flow rate is governed by its unique properties [54], and managing velocity constraints are important to prevent vibration-induced fatigue and erosion [51].

Hydrogen transportation in flexible pipes involves several failure risks, including fatigue from cyclic stress, erosion due to high flow velocities, and hydrogen embrittlement. Effective material selection and design constraints, requires materials with high resistance to hydrogen embrittlement HE and control of flow velocities to avoid erosion and vibration-induced fatigue. Embrittlement can lead to rapid crack propagation and material failure, making the use of HE-resistant materials essential. A recent study evaluated the suitability of flexible pipes for hydrogen transport, providing optimal material solutions for different layers in un-bonded flexible pipes [55]. The dynamic nature of flexible pipes, with repetitive bending, further increases fatigue risks when combined with embrittlement. Additionally, implementing safety measures, such as effective grounding and regular monitoring, is needed to mitigate the risks associated with hydrogen leaks and ignition during transport.

2.5.2. Selection of hydrogen properties

In this research, constant pressure, temperature, and density are assumed throughout the entire length of the pipeline. Flow-induced vibrations and other risk factors, such as hydrogen embrittlement and erosion from high flow velocities, are not included in this analysis. Moreover, the gas flow rate is also considered to be constant.

3

Methodology

This chapter outlines the framework used to analyze flexible pipe systems. It begins with an overview of the design conditions and processes in section 3.1, including the design stages of flexible pipes, failure modes, and pipe limitations. Section 3.2 provides the theoretical foundation and basis of the design, covering specifications on simulation tool, configurations, and of all components used in this research. Section 3.3 details the reference case study used as the preliminary design, describing all the required input parameters for its configuration layout, simulation, and the capacity for hydrogen production. The software tool used is analyzed in section 3.4, covering the techniques, motion equation, and its verification, after which all integrated analysis techniques are evaluated. The development of the base case scenario leads to a discussion of the evaluation criteria for its boundary conditions, as well as a comparison between the static and dynamic analyses in section 3.5. Finally, the chapter discusses the parameter setup for different water depths based on the exploration of key parameters, ending with the setup for sensitivity analysis.

3.1. Design Conditions and Process

This section presents the process used in the design of flexible pipes. The following subsections outline the essential stages of the design overview, failure modes, and its constraints and limitations.

3.1.1. Overview design stages

The design process for flexible pipe applications in dynamic environments follows a series of well-defined stages, as outlined by [26] (see appendix B.4 for the complete flow chart [26]). These stages include:

1. **Material Selection:** Choose materials that are compatible with the transported product and meet functional requirements. This step involves specifying materials for all layers, as discussed in section 2.1.5.
2. **Cross-Section:** Select the pipe's cross-sectional structure and dimensions based on functional needs. Various layers and orientations can be developed for flexible pipes.
3. **System Configuration:** Determine the system layout and geometrical shape from available options, as described in section 2.2.2. Ancillary components like the buoyancy section and BS are also considered at this stage.
4. **Dynamic Analysis:** Evaluate the riser's dynamic response under different loading conditions, addressing potential interferences with other systems, tensions, and curvatures.
5. **Detail and Service Life:** Focus on the detailed design of ancillary components and assess corrosion protection, including a full service life analysis of the pipe and all components.
6. **Installation:** Finalize the design by selecting and designing all installation systems, including vessels, equipment, and methodologies. Detailed global and local analyses ensure the chosen system's feasibility.

Stage 1 and 2 are carried out using in-house software from NOV [56], resulting in the hypothetical pipe tailored to this study's needs. The selection of materials and cross-sections is based on hydrogen parameters, location specifics, pipe length, and water depth. While material selection for stage 1 is based on applicability for hydrogen conditions, validation has not been fully conducted. Similarly, stage 2 relies on previous experiences with other applications, keeping the design as simple as possible. Consequently, the pipe has not undergone all required testing in facilities before being recommended for real-life application, and is thus constructed based on knowledge and experience from previous applications.

The completion of stage 2 leads to the focus on stages 3 and 4 of the design process. This research specifically addresses these stages, where the output of stage 2 serves as the input requirements. The system configuration design focuses on the lazy wave shape with the use of BM, while the dynamic analysis considers location-specific environmental conditions. The output of stages 3 and 4 verifies whether the pipe can operate within the limits specified at the end of stage 2, ultimately determining the pipe's suitability for supporting the system and dynamic design as the end-purpose.

If stages 3 and 4 show successful outcomes, the detailed and installation design follows, which focuses on end fittings, corrosion protection, monitoring provisions, vessels, equipment, etc. If the response based on the outcome of stage 4 is not recommended, various configurations can be checked, or it may be concluded that the material of the cross-section unbonded flexible pipe is not sufficient. The success of stage 4 is verified by exploring the various failure modes.

3.1.2. Potential failure modes

Designing the pipe requires careful consideration of potential degradation and failure modes for the intended application. Failure of a flexible pipe can occur during different life phases, including operational, manufacturing, transportation, and decommissioning. Table 3.1 outlines specific mechanical failure modes relevant to the operational life phase, including accompanying failure mechanisms and possible design solutions. Other failures include hydrogen embrittlement, impacts, pigging, aging wear, and vibrations [57], as well as issues related to thermal properties, permeation characteristics, or material compatibility [31].

The table specifies potential failure mechanisms and their corresponding design solutions, which involve modifying certain design stages. For instance, modifying stage 1 or 2 may include adjustments to specific layers prone to failure, such as increasing layer thickness, changing the material selection, enhancing the material's strength, modifying the layer build-up, or adding additional layers. Stage 5 modifications include designing protection systems or additional support ancillaries. During stages 3 and 4, changes to the system configuration are necessary, which involves altering the system's shape by adjusting different configurational parameters. [31]

Table 3.1: Listing of failure Modes for flexible pipes [31]

Global Failure Mode	Potential Failure Mechanisms	Design Solutions
Collapse	Collapse of carcass/pressure armor due to tension, external pressure or installation loads or internal pressure sheath	Modify stage 1/2 or 3/4
Burst	Rupture of pressure or tensile due to excessive internal pressure.	Modify stage 1/2
Tension	Rupture of tensile armors or collapse of carcass/pressure armor/internal sheath	Modify stage 1/2 or 3/4
Compression	Birdcaging of tensile armor wires	Modify stage 1/2 or 3/4
Overbending	Collapse of carcass/pressure armor/internal pressure sheath or unlocking of interlocked layers	Modify stage 3/4
Torsion	Failure of carcass/tensile armor/internal pressure sheath or birdcaging	Modify stage 1/2 or 3/4
Fatigue	Tensile armor/pressure armor wire fatigue	Modify stage 1/2 or 3/4
Erosion	Internal carcass	Modify stage 1/2
Corrosion	Internal carcass or pressure/tensile armor exposed to seawater or internal fluid	Modify stage 1/2 or 5

3.1.3. Design constraints and pipe limitations

The design constraints for flexible pipes are defined by the parameters specified in stages 1 and 2, as determined by the manufacturer. Specific design criteria for unbonded flexible pipes are provided by design codes [58]. To prevent mechanical failure modes listed in table 3.1, modifications of different stages are possible, yet, stages 1 and 2 are taken as constant provided by the in-house software of NOV. Additionally, stages 5 and 6 can only be completed if stages 3 and 4 are successfully executed. This narrows the focus to failure modes that can be prevented during stages 3 and 4, such as collapse, tension, compression, overbending, torsion, and fatigue.

The multi-layered structure of the pipe complicates the application of the proposed combined loading criteria method by [59], as each layer has its limitations and failure modes. The interaction of different layers makes this capacity more complex than that of single-layer dynamic or steel risers used in the oil and gas industry. For example, fatigue-susceptible layers are not made of continuous homogeneous material, with pressure layers having interlocked structures and armor wires wound helically, indicating that the fatigue of these local structures requires finite-element analysis models for accurate calculation. Therefore, the fatigue life will not be evaluated due to its extensive nature.

Similarly, the decision not to focus on torsion is based on the nature of the flexible riser, which is less subjected to torsional motions. As the pipe is connected to the FOWT, which imposes 6DOF, the primary governing wave and aero-induced motions are surge, heave, and pitch [60] [61]. This results in torsion-induced motion being minimal at both end points due to minimal generation of torsion-induced axial motion. However, gyroscopic effects of the Rotor Nacelle Assembly (RNA) can influence the yaw motion of the FOWT [60], and furthermore torsion-induced pressure can occur [62], but these are outside the scope of this research. Therefore, the primary focus is on failures caused by collapse, tension, compression, and overbending.

These four drivers are the requirements for input at stage 3 of the design process. These failure modes can be addressed during the design stages of stages 3 and 4. Tensile and overbending failures are governed by tensile forces and bending moments, while collapse failure is governed by external pressure limiting the pipe to a specific water depth, and compression is governed by ensuring the axial load is not negative. The hypothetical flexible pipe is therefore governed by its maximum capacity, defined by the Minimum Breaking Load (MBL) and the Minimum Bend Radius (MBR). These specifications, provided by the pipe manufacturer, outline limits that must not be exceeded:

- Minimum Breaking Load (MBL): 531 kN
- Minimum Bend Radius (MBR): 1.69 m
- Maximum allowable depth: 510 m

3.2. Basis of Design and Theory

This section provides an overview of the foundational design and theoretical aspects relevant to this research. It includes subsections on the simulation tool, the geometric configurations of the lazy wave, and detailed specifications for the configurations, the FOWT model, pipe, buoyancy sections, and BS.

3.2.1. Simulation tool

The analysis of the effects on pipes in both static and dynamic environments can be performed through analytical calculations, numerical simulations, or physical testing. This research focuses on numerical simulations, where precise modeling and simulation are crucial for accurately predicting the behavior of offshore systems. The commercially available software OF is utilized. OF is a fully 3D, non-linear, time-domain finite element dynamic analysis software, widely employed in the offshore industry. Umbilical systems display nonlinearity due to factors like hydrodynamic forces, geometric stiffness, extensive 3D rotations, material inconsistencies, and seabed interactions. The nonlinear approach effectively captures potential non-Gaussian behaviors in response to environmental and operational conditions [63].

To achieve reliable results, it is important to balance simulation accuracy with computational efficiency. The response from these simulations provides insights into the motion and loads on a pipe, identifying locations where loads are highest. These analyses often include range graphs, which display mean, minimum, and maximum values along the length, and time histories, which track load variations over time. Normalized results are particularly useful for visualizing areas at risk of failure by comparing loads or motions against their limits. Steps for creating a precise design and its operating environment include:

- Implementing environmental parameters accurately, ensuring that load cases represent typical and realsitic conditions.
- Accurately representing FOWT motions, whether through full modeling or pre-obtained motion time histories.
- Inputting realistic parameters for the pipe and auxiliary components, using validated values from existing literature or in-house data from similar deployed pipes.

3.2.2. Geometrical configuration of the lazy wave

The configuration of the lazy wave consists of multiple sections to generate this particular shape. Figure 3.1 visualizes the different sections of the lazy wave shape. The pipe is connected at HOP on the semi-submersible and its ending point at the TP. The generated wave shape is created by the BMs, denoted as the buoyancy section, or section 2. The non-buoyant section from the HOP to the buoyant section is denoted as section 1, and the non-buoyant section from the buoyant section to the TP is denoted as section 3. The generated wave shape in the configuration features the HB, a vertically higher bend due to the buoyant section, and the SB, a vertically lower bend due to the non-buoyant part of the pipe. Furthermore, at the beginning, a BS is present, although it is not visualized in this figure. The FOWT, pipe (non-buoyant sections), buoyant section, and BS will be elaborated on in the subsequent sections.

3.2.3. Floating offshore wind turbine model specifications

The FOWT is the K03 semi-submersible, equipped with a 15 MW reference wind turbine, developed as part of the International Energy Agency's Wind Task 37 [64], as visualized in figure 3.2. The turbine's RNA is designed with a three-bladed rotor; however, in this research, the coupled aerodynamic model has been de-assembled, meaning the RNA and the blades are not modeled. To compensate for the

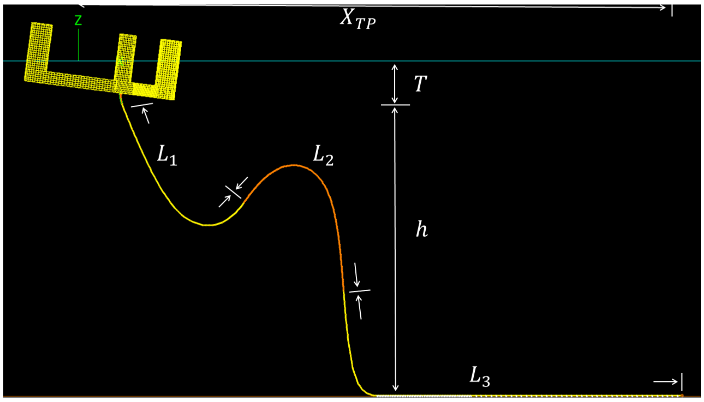

Figure 3.1: Overview of the lazy wave shape

lack of blades, the thrust force or drag is modeled at hub height. The nacelle is supported by a tower mounted on the Umaine Volturn US-S semi-submersible platform. The specific design details of the platform, mooring, and tower are provided in [65]. The model does not account for the dimensions or weight of an electrolyzer, as this is not yet developed.

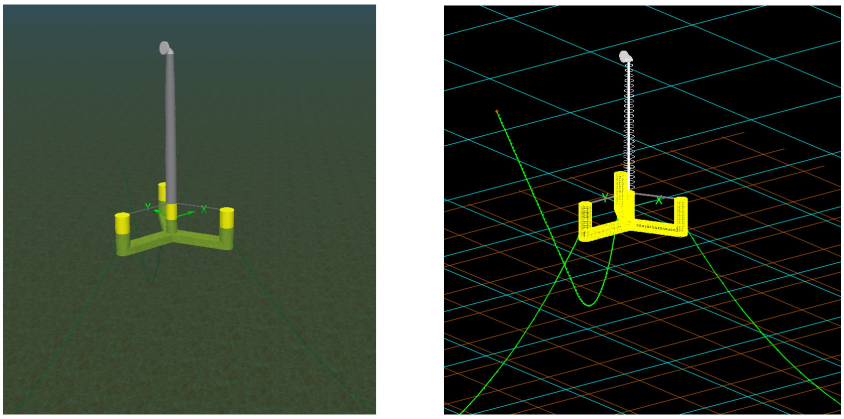

Figure 3.2: K03 15MW semi-sub FOWT

3.2.4. Pipe specifications

The in-house software from NOV provides the structural parameters of the pipe, which are listed in table 3.2. These parameters are provided by the manufacturer, and not varied throughout this research. The derivation of the hydrodynamic drag coefficients in the normal direction is shown in appendix B.1 [66], whereas the coefficients in the axial direction are not specified and are thus taken as default values in the software of OF. Furthermore, the pipe is connected to the center of the platform.

To determine the net force on a submerged section of the pipe, the difference between buoyancy and gravity forces can be expressed with equation 3.1. Since the wet mass per unit length is known, the equation for the dry mass per unit length can be simplified using these properties as follows:

$$\begin{aligned} F_{subm,pipe} &= F_{b,pipe} - F_{g,pipe} = \rho_{sw} g V_{displaced} - m_{pipe} g \\ &= \rho_{sw} g A L - w_{pipe,dry} g L = -w_{pipe,wet} g L_{total} \end{aligned} \tag{3.1}$$

where $F_{subm,pipe}$ is the submerged weight of the pipe in N, $F_{b,pipe}$ and $F_{g,pipe}$ are the buoyancy and gravity forces on the pipe in N, ρ_{sw} is the density of seawater in kg/m^3, g is the gravitational constant in m/s^2, $V_{displaced}$ is the displaced volume of the object m^3, m_{pipe} is the mass of the pipe in kg, A is the surface area of the submerged part in m^2, L_{total} is the total length of the submerged part in m, $w_{pipe,dry}$ is the dry mass per unit length in air in kg/m, and $w_{pipe,wet}$ is the wet mass per unit length in seawater in kg/m.

The pipe consists of multiple sections, each with a different net force. The total net force is the combined net force of these sections, derived using equation 3.2. This consists of three sections, where the second

Table 3.2: Structural specifications of the pipe

Properties	Symbol	Unit	Value	Comment
Outer diameter	OD_{pipe}	m	0.1622	4 inch
Inner diameter	ID_{pipe}	m	0.1016	6.4 inch
Mass per unit length in air empty	$w_{pipe,dry}$	kg/m	36.3	Operational = 36.5
Mass per unit length in sea empty	$w_{pipe,wet}$	kg/m	15.1	Operational = 15.3
Bending stiffness	EI	kNm^2	20	
Axial stiffness	EA	MN	160	
Torsional stiffness	GJ	kNm^2/deg	6	
Normal & axial drag coefficients	$C_{D,pipe}$	-	1.05, 0.008	[35], [66], Default
Normal & axial drag coefficients	$C_{A,pipe}$	-	0.6, 0	[66], Default
Poisson ratio	v_{BS}	-	0.3	[67]
Seabed friction	μ_{SB}	-	0.5	[68], Default

section is the buoyancy section of the pipe. The first and third sections simplify F_1 and F_3 to $F_{subm,pipe}$, respectively.

$$F_{subm,tot} = F_1 + F_2 + F_3 = -w_{pipe,wet} g L_1 + F_2 - w_{pipe,wet} g L_3 \tag{3.2}$$

where F_1 and F_3 are the submerged weights of the pipe in sections 1 and 3 respectively in N, L_1 and L_3 are the lengths of sections 1 and 3 in m, and F_2 is the net force of the buoyancy section in N, which will be elaborated upon in the following section.

3.2.5. Buoyancy section specifications

BM are important in the lazy wave configuration, positioned between the HOP and TDP of the pipe to generate an upward buoyancy force that exceeds the pipe's gravitational force in water. Typically, for deepwater lazy wave risers, the buoyancy force is double the combined weight of the steel pipe and its contents [69]. Various BM geometries are available for riser and DPC configurations, installed at consistent intervals or pitch, and can be customized to specific requirements [70, 71]. Fewer BM units reduce costs and simplify installation. Figure 3.3 shows the application of BM's. These are typically made from composite foams with low water absorbency to maintain the lazy wave configuration and must be securely attached to the riser to prevent changes in configuration.

(a) BM clamped on pipe structure model [41]

(b) BM application on pipe [35]

Figure 3.3: Buoyancy Modules on a pipe structure

The net force on a single submerged BM can be calculated with the following equation:

$$F_{subm,BM} = F_{b,BM} - F_{g,BM} = (\rho_{sw} g V_{displaced}) - (m_{BM} g) = (\rho_{sw} - \rho_{BM}) g V_{BM} \tag{3.3}$$

where $F_{subm,BM}$ is the submerged weight of the BM in N, $F_{b,BM}$ and $F_{g,BM}$ are the buoyancy and gravity forces on the BM in N, m_{BM} is the mass of the BM in kg, ρ_{BM} is the density of the BM in kg/m^3, and V_{BM} is the volume of the BM in m^3.

The net force on a submerged BM depends on its volume, calculated using equation 3.4 where the BM is assumed to be a hollow cylinder. Figure 3.4 illustrates single BM's attached to the pipe, denoted as a discrete buoyancy BM.

$$V_{BM} = \frac{\pi}{4}(OD_{BM}^2 - OD_{pipe}^2) L_{BM} \tag{3.4}$$

where OD_{BM} is the outer diameter of the BM in m, OD_{pipe} is the outer diameter of the pipe in m and L_{BM} is the length of BM in m.

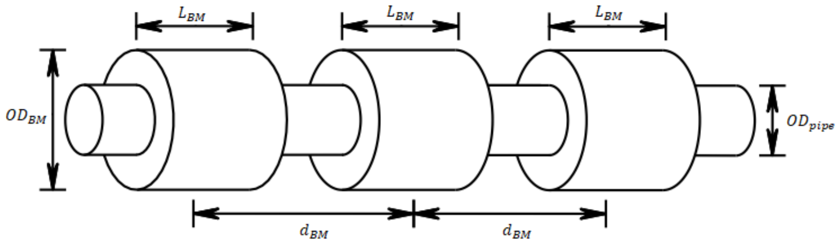

Figure 3.4: Schematic overview of a discrete buoyancy section [69]

In OF, there are two methods to implement BM's on a pipe: as discrete BMs attached at pre-determined locations (figure 3.4) or as distributed buoyancy, where BM's are uniformly distributed along the pipe's length (figure 3.5). Within OF, a specialized tool configures the distributed buoyancy section by the derivation of implemented data from the discrete buoyancy method. The distributed method is particularly useful for global analysis as it converts the properties of individual BM's into a uniform section, bypassing the design constraints of individual modules. This approach allows for a combined buoyancy force to create geometries tailored to specific applications [72].

Figure 3.5: Schematic overview of a distributed buoyancy section

For this research, the distributed method is employed rather than the discrete buoyancy to simulate an equivalent buoyancy section. The buoyancy section is treated as a simplified structure with a uniform external diameter. The equivalent outer diameter and mass per unit length are defined with equations 3.5 and 3.6, respectively. The equivalent drag coefficients are provided in appendix B.2, with the added mass calculated using the same process. For the equivalent buoyancy section's diameter, the tool within OF directly calculates the drag and added mass coefficients using data from the discrete method, determining equivalent coefficients appropriate for the distributed buoyancy section.

$$OD_{BM,e} = \sqrt{(OD_{BM}^2 - OD_{pipe}^2) * \frac{L_{BM}}{d_{BM}} + OD_{pipe}^2} \tag{3.5}$$

where d_{BM} is the constant pitch be between the BM's in m.

$$w_e = w_{pipe,dry} + \frac{\pi}{4}(\rho_{BM} L_{BM}(OD_{BM}^2 - OD_{pipe}^2) + m_{BM,H})g/d_{BM} \tag{3.6}$$

where ρ_{BM} is density of BM's in kg/m^3 and $m_{BM,H}$ is the mass of teh hardware of the BM kg.

The distributed method necessitates adjusting the force from equation 3.3 from single BM to distributed data. By incorporating the equivalent outer diameter and mass per unit length, the net vertical force for the buoyancy section is calculated using equation 3.7. In this research, potential buoyancy losses, anticipated at around 10% [69], are disregarded.

$$F_2 = \rho_{sw} g \frac{\pi}{4}(OD_{BM,e}^2)L_2 - w_e g L_2 \tag{3.7}$$

where ρ_{sws} is density of the sea water in kg/m^3 and L_2 is the length of the buoyancy section in m.

3.2.6. Bend stiffener specifications

The section after the HOP is critical due to its susceptibility to overbending caused by significant motion responses of the FOWT. To mitigate this, a BS is integrated to reinforce the pipe's stiffness, preventing it from bending beyond its allowable radius. This increases performance by ensuring a smooth transition between the pipe and its end connection, as illustrated in figure 3.6. Typically made from polyurethane, BS are anchored in a steel collar to facilitate load transfer and strengthen the connection point. Key design considerations include fatigue and creep characteristics, which determine the optimal conical dimensions [41]. Bell mouths and bend restrictors also serve to prevent excessive bending at various points along the pipe length.

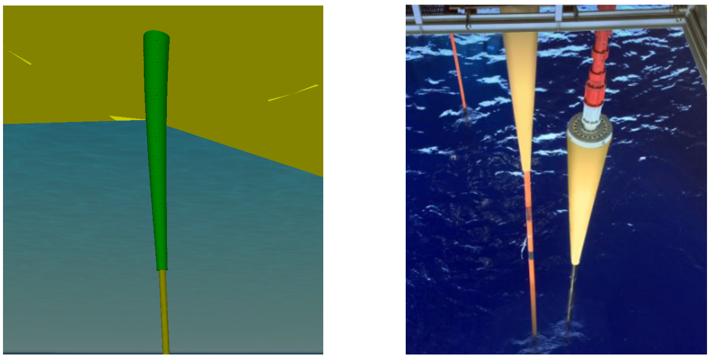

(a) BS clamped on pipe model **(b)** BS application on pipe

Figure 3.6: Bend Stiffener on a pipe structure

BS are highly recommended to provide additional support against bending without inducing tension. Previous studies indicate that these stiffeners are tailored to specific end-use applications and lack a uniform design [73] [74]. However, the density and Young's modulus are typically held constant at 1200 kg/m^3 [75] and 45 MPa [76], respectively. The dimensions of the BS are shown in figure 3.7, where the OD_{pipe}, L_{tip}, t_{tip}, and clearance gap between the BS and the pipe are fixed.

3.3. Reference Case Study

This section establishes the reference case for this research, used as the preliminary design, incorporating parameters of configuration, system layout, simulation requirements, and the capacity of hydrogen production.

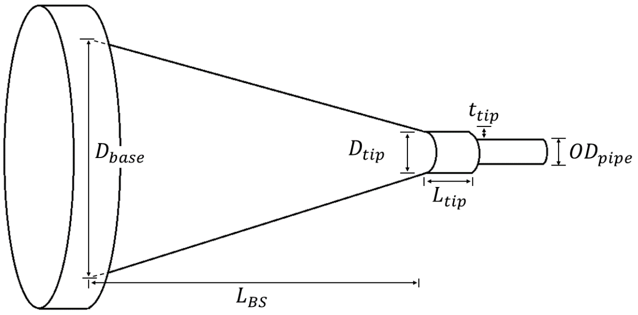

Figure 3.7: Schematic overview of a Bend Stiffener

3.3.1. Configuration and ancillaries properties

For various configurations, it has been demonstrated that the lazy wave configuration is superior to the catenary configuration. In optimizing a DPC, initial recommendations for umbilical design are provided based on specific DPC properties, including buoyancy section weight and submerged weight. These recommendations offer a balanced solution for tension and curvature [23, 76]. The following generalized rules of thumb form the reference case for this research:

- Total length of the umbilical is 2.8 times the vertical distance from seabed to HOP
- The first second, second section and third section for the umbilical are in ratios of 1:1:2
- The horizontal distance between HOP and termination point is 2 times the vertical distance from seabed to HOP

At a water depth of 200 meters, the reference case configuration yields the following properties specified in table 3.3.

Table 3.3: Properties of the geometrical shape for the reference case

Properties	Symbol	Unit	Value	Comment
Water depth	d	m	200	
Draft	T	m	20	
Vertical HOP distance	h	m	180	$h = d - T$
Total length	L_{total}	m	504	$L_{total} = 2.8 * h$
Length first section	L_1	m	126	$L_1 : L_2 : L_3 = 1 : 1 : 2$
Length second section	L_2	m	126	$L_1 : L_2 : L_3 = 1 : 1 : 2$
Length third section	L_3	m	252	$L_1 : L_2 : L_3 = 1 : 1 : 2$
Termination point	X_{TP}	m	360	$X_{TP} = 2 * h$

To maintain an identical geometrical shape of the pipe at 200-meter water depth to a DPC, adjustments in the buoyancy section are necessary, as a flexible pipe has its own specifications. BM are typically produced for specific end-use, based on the amount of buoyancy needed to achieve the required geometrical shape [77]. Studies show variations in density, hardware mass, and dimensions of BMs depending on the configuration [78, 79]. To replicate the configuration of the reference case for the DPC, the length and diameter are set to 0.9 m and 0.73 m, respectively. Table 3.4 lists these specifications of the parameters. The length, density, hardware mass, and coefficients remain constant, while OF translates these into properties for the distributed buoyancy section, as specified in section 3.2.6. For the reference case, the BS parameters are adopted from [23]. Typically, only the length and the tip and base diameters are provided, but not all geometrical parameters are specified. These include the thickness at the tip, the length of the tip, and the clearance gap. These will be further developed in section 3.4.7 during the BS geometric development. Throughout the parametric study, the density, Young's modulus, and coefficients will remain constant with properties from this reference case.

Table 3.4: Properties of ancillaries for the reference case

	Properties	**Symbol**	**Unit**	**Value**	**Comment**
BM	Length	L_{BM}	m	0.9	
	Diameter	OD_{BM}	m	0.73	
	Pitch	d_{BM}	m	6	[43]
	Hardware mass	$m_{BM,H}$	te	0.025	Default
	Density	ρ_{BM}	te/m^3	0.5	Default
	Normal & axial drag coefficients	$C_{D,BM}$	-	0.209, 1	[80]
	Normal & axial added mass coefficients	$C_{A,BM}$	-	0.459, 0.6	[80]
BS	Length	L_{BS}	m	3	[76]
	Diameter base	D_{base}	m	0.7	[76]
	Diameter tip	D_{tip}	m	0.38	[76]
	Length tip	L_{tip}	m	-	NA
	Thickness tip	t_{tip}	m	-	NA
	Clearance gap	-	m	-	NA
	Density	ρ_{BS}	te/m^3	1.2	[23]
	Young's Modulus	E_{BS}	GPa	0.45	[23]
	Drag coefficient	$C_{D,BS}$	-	1	Default
	Added mass coefficient	$C_{A,BS}$	-	1	Default
	Poisson ratio	v_{BS}	-	0.45	[75]

3.3.2. Overview of complete system lay-out

The FOWT by [65] features a pre-modeled layout for the mooring lines, which are typically oriented and dimensioned to withstand ultimate load conditions [81]. While the orientation of the platform relative to metocean conditions is not specified, it is important for a FOWT with DPCs to avoid contact with mooring lines by establishing a safe distance between components. Contact is unacceptable due to the risk of damage and operational failure. To prevent such interactions, a minimum angular clearance of 12 degrees between the DPC and mooring lines is recommended [82], serving as a safety measure to avoid interactions.

The semi-submersible platform is symmetrically designed in the xy-plane, with mooring lines spaced 120 degrees apart. This symmetry allows for potential pipe orientations ranging from 12 to 108 degrees relative to the mooring lines. A single pipe orientation was chosen, positioned precisely between two mooring lines to minimize the probability of contact and interference with the mooring lines.

The lay-out supports decentralized offshore wind-to-hydrogen configuration where electrolysers are placed at each FOWT seperately, minimizing the need for extensive electrical infrastructure and enhancing operational resilience [53]. Figure 3.8 illustrates the top view of the complete system layout, showing the selected orientation in relation to the mooring lines. This system layout is applied in the reference case and across the entire research. No alternative layouts will be considered or developed in subsequent analyses.

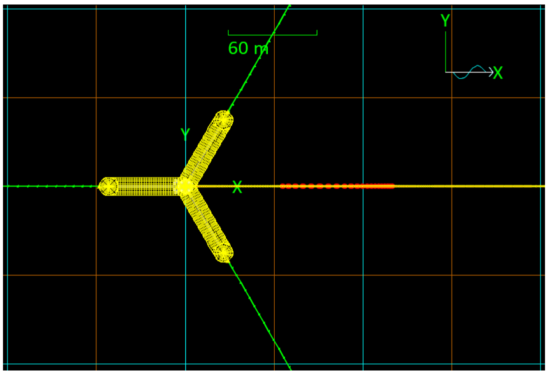

Figure 3.8: Top-view orientation of the complete system lay-out

3.3.3. Required input for simulations

For the reference case, additional input data is required, encompassing environmental conditions and simulation parameters. Both inputs will be thoroughly investigated in the next section, which includes an environmental study and a convergence study. However, before these analyses are conducted, preliminary simulations require these parameters to be implemented with specific values. The environmental parameters are adopted from the similar study of recommendations for the configurational parameters [23], while the simulation parameters are based on a combination of internal recommendations from Vattenfall and NOV.

For explanations of all parameters listed in table 3.5, refer to the designated sections of the environmental study in section 3.4.6 and the convergence of simulation parameters in section 3.4.8, where the development of these parameters is discussed in detail. These preliminary parameters are thus not used in the parametric study. They are provided for the complete implementation of the reference case and will be applied only in the initial analyses presented in the following section, until further development.

The peak enhancement factor was not provided by [23]; hence, it was decided to set this value at 2 [82]. For the simulation parameters, the target segment length of 1m defines the segment length for the non-buoyant section, while the recommendation of the buoyant section uses half this resolution to minimize unrealistic behavior due to its bending characteristics [82]. Furthermore, the resolution for the BS is always set to 0.05m, as this is a highly sensitive component to curvature [76].

Table 3.5: Properties of simulation input for the reference case

	Properties	**Symbol**	**Unit**	**Value**	**Comment**
Environmental parameters	Wind speed	V_{rated}	m/s	10	[23]
	Thrust force	F_{thrust}	MN	2.9	[23]
	Significant wave height	H_s	m	5	[23]
	Peak wave period	T_p	s	11.2	[23]
	Peak enhancement factor	γ	-	2	[82]
	Current speed	U	m/s	0	[23]
	Wind/wave/current direction	-	°	0	[23]
Simulation parameters	Time step	-	s	0.1	[82]
	Target segment length non-buoyant section	-	m	1	[23][56][82]
	Build-up time	-	s	600	[82]
	Simulation time	-	s	10800	[82] [83]

3.3.4. Hydrogen production and capacity

Hydrogen production is based on the design requirements of 40 barg and 50 °C as the output from the electrolyzer, with hydrogen's energy content being 55 kWh/kg and the wind turbine capacity rated at 15 MW, operating with an efficiency of approximately 60% [82]. The internal fluid velocity is estimated at 15 m/s [84]. The mass flow rate of hydrogen is estimated at 0.04545 kg/s using the following equation:

$$\dot{m}_{\mathrm{H_2}} = \frac{P \times \eta}{E} \tag{3.8}$$

where P is the power output in MW, η the efficiency factor and E is the energy content of hydrogen in kWh/kg.

The density of hydrogen can be approximated using the ideal gas law. While higher temperatures favor ideal gas behavior, the high pressures involved lead to compressed behavior and intermolecular forces. This provides a reasonable approximation, but greater accuracy can be achieved by using compressibility factors to account for deviations from the ideal gas law. However, using the ideal gas law, the density is estimated to be 3.00 kg/m^3. Combining the mass flow rate and density yields an maximum estimated volumetric flow rate of 0.01515 m^3/s.

Assuming the turbine and electrolyzer are running at full capacity, a pipe with an internal diameter of $0.0359m$ (1.4 inches) would be sufficient for transporting all the produced hydrogen. If the hypothetical pipe specified in section 3.2.4 is used, it would thus sufficiently accommodate the required transport capacity, given its inner diameter of $0.1016m$ (4 inches). Therefore, the reference case with a single pipe can be employed. For detailed calculations, see appendix B.3.

Comment: During this research, the derived density was not used in simulations due to an implementation error, resulting in a density value that was ten times higher.

3.4. Numerical Software Analysis

This section provides a comprehensive evaluation of the software analysis. It begins with techniques and the equation of motion, followed by the verification of the pipe to ensure accurate interpretation. The analysis then compares the De-Coupled Method (DCM) and the Fully-Coupled Method (FCM) modeling approaches, along with a comparison between discrete and distributed buoyancy methods. An environmental study is conducted to determine the conditions that excite the worst response from the system, followed by the development of the BS. Finally, the simulation parameters are determined through a convergence study. Although the analyses in this section are performed sequentially in the specified order, the convergence study did not incorporate the developed BS.

3.4.1. Modeling techniques

OF uses the lumped mass model for the simplification of the pipe. This approach enhances computational efficiency by dividing the line into straight, massless segments defined by nodes at both ends. The axial and torsional properties of the line are directly modeled, while other properties like mass, weight, buoyancy, and drag are concentrated at the nodes. Each node combines the properties of the adjacent half-segments, where forces and moments are applied. Fluid-related forces, including buoyancy and drag, are calculated based on the varying wetted length relative to the water surface. Each segment is modeled as two co-axial telescoping rods linked by axial and torsional spring-dampers, while bending properties are simulated through rotational spring-dampers at the segment ends. The discretized model is illustrated in figure 3.9.

OF employs a global modeling approach, representing the pipe with a uniform, solid cross-section. This method does not capture internal dynamics such as inter-component movement and friction. However, it enables the estimation of its global loads without delving into effects on different layers. For local analysis, specialized software would require global load data as input for a 3D local finite-element analysis model, which applies stress factors to convert these loads into detailed stress and strain responses. This research will not explore local analysis methods due to time constraints and the unavailability of suitable software, but it recognizes the physical limitations associated with this modeling approach.

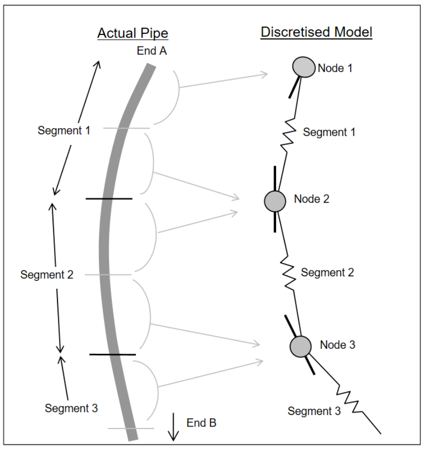

Figure 3.9: Finite element model in OrcaFlex [85]

3.4.2. Equation of motion

Understanding pipe configurations requires analysis of both their equilibrium states and responses in dynamic environments. Static analysis determines the equilibrium configuration necessary for subsequent dynamic analysis [86]. This focuses on the pipe's weight and buoyancy while assuming external loads are zero. Dynamic analysis, on the other hand, incorporates external environmental forces such as wave action, wind, currents, FOWT motions, and seabed friction. These factors influence the system's behavior under operational conditions. This analysis adopts a nonlinear time-domain approach to model the response. The outcomes of this complete section are governed by the results of the dynamic analysis. The equation of motion used to model the system's response, detailed in equation 3.9, is applied node by node. This creates a localized equation for each node rather than a collective system equation.

$$M(p,a)+C(p,v)+K(p)=F(p,v,t)[85] \tag{3.9}$$

where $M(p,a)$ represents the inertia load, $C(p,v)$ denotes the damping load, and $K(p)$ the stiffness load. $F(p,v,t)$ corresponds to the external excitation load, with p, v, and a referring to the position, velocity, and acceleration, respectively, and t the simulation time.

3.4.3. Verification of software assumptions

In OF, certain design modeling decisions require verification. This is achieved by comparing theoretical loads with the results from numerical OF simulations. The discrepancy between theoretical and numerical results is calculated using the following formula:

$$Discrepancy=\frac{|Numerical-Theoretical|}{|Theoretical|} \tag{3.10}$$

Gravity and Buoyancy Forces: The first verification involves end-forces due to gravity and buoyancy on a pipe without a buoyancy section. The pipe is suspended in both air and water (see figure 3.10a). For the scenario suspended in air, there are no buoyancy forces, whereas, in water, buoyancy forces are present. The endpoint forces are calculated using equation 3.11, where w_{pipe} represent $w_{pipe,dry}$ and $w_{pipe,wet}$, the mass when the pipe is suspended in air and water, respectively. The discrepancies in the dry and wet weight forces are 0.068% and 0.85%, confirming that the gravitational and buoyancy forces are accurately modeled in OF.

$$F_{end}=\frac{1}{2}w_{pipe}Lg \tag{3.11}$$

Buoyancy Section: The second verification concerns the forces on a distributed buoyancy section, modeled using the equivalent outer diameter $OD_{BM,e}$ and equivalent mass per unit length w_e (equations 3.6 and 3.5). The buoyancy force is calculated using equation 3.12 and visualized in figure 3.10b, where the pipe is only suspended in water. The discrepancy in the endpoint forces for the buoyancy section is 1.85%, higher than that of the non-buoyant section.

$$F_{end}=\rho_{sw}g\frac{\pi}{4}(OD_{BM,e}^2)L-w_egL \tag{3.12}$$

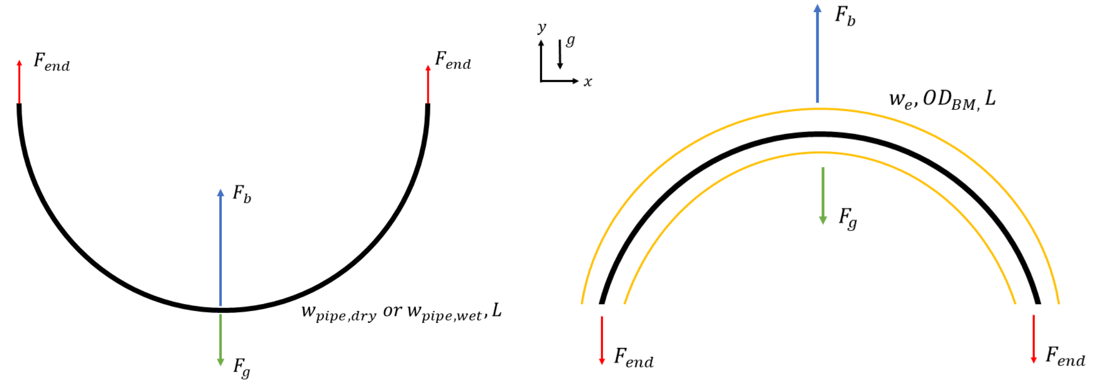

(a) Pipe suspended in air or water **(b)** Buoyancy section suspended in water

Figure 3.10: End-forces for gravity and buoyancy test scenarios

Beam Theory Verification: The Euler-Bernoulli beam theory is used in OF to analyze the behavior of beam-like structures. This theory assumes linear elasticity, small deformations, neglects shear deformation and assumes that place sections remain plane. However, flexible pipes are far more complex, with multiple layers and non-homogeneous materials. For more information on this theory, see appendix B.5. While computationally efficient, these simplifications can introduce inaccuracies:

- **Material Homogeneity:** OF treats the multi-layered pipe as homogeneous and isotropic, assuming material properties uniform throughout the structure and behave identically in all directions.
- **Constant Cross-Section:** The assumption of a constant cross-section along its length neglects the complex interaction between layers, potentially leading to inaccurate stress distributions.
- **No Layer Separation:** The theory does not account for relative movement or separation between layers when subjected to loading, affecting structural integrity.
- **Neglecting Non-Linearities:** The beam theory assumes linear elasticity, which may not hold under high stress or strain conditions, leading to inaccuracies in response predictions.
- **Neglecting Shear and Warping Effects:** The theory assumes that plane sections remain plane, neglecting potential warping and shear deformation in flexible pipes, and underestimating the deformation.

The beam theory simplifications might leads to discrepancies between the simulation results and actual pipe behavior in the field, resulting in less accurate predictions for overall pipe performance. Yet, the application of beam theory in OF is verified by comparing the modeled axial and bending stiffness with theoretical predictions. Axial stiffness is tested by applying an axial force, resulting in pipe elongation, while bending stiffness is tested by applying a bending moment to the pipe's end. These tests are shown in figure 3.11. The discrepancies for axial and bending stiffness were 1.85×10^{-4}% and 7.12×10^{-2}%, respectively, confirming that OF closely models these stiffnesses according to beam theory.

$$F_{axial} = EA\frac{\Delta L}{L} \tag{3.13}$$

$$M_{bend} = \frac{EI}{R} \tag{3.14}$$

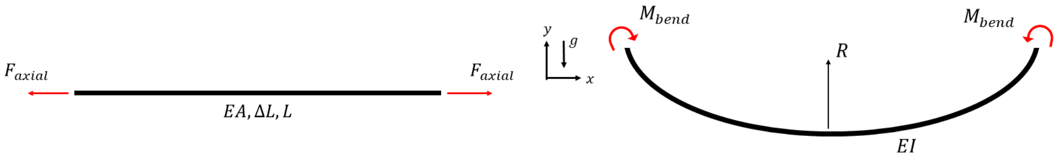

(a) Axial force **(b)** Bending moment

Figure 3.11: Axial and bending stiffness test scenarios

3.4.4. De-coupled and coupled method comparison

This section explores the differences between the DCM and FCM. The FCM approach models the entire system, integrating the FOWT's motion with the connected pipe and mooring system, allowing for the interaction of all components. This method accounts for forces such as restoring, damping, and inertia, which influence the response of the FOWT [87]. Restoring forces include hydrostatic horizontal and angular restoration due to pipe and mooring displacement, while damping forces account for hydrodynamic drag interactions influencing the flow among components. Additionally, the inertia forces from the mass of the pipe and mooring affect the system's behavior under environmental loads. In contrast, the DCM evaluates these components separately, neglecting these coupling effects. Typically, the FOWT's motion is first assessed, either through numerical simulations or experimental data, which are then used as an input for simulating the pipe's response [88]. While the FCM is comprehensive, it is also computationally demanding, whereas the DCM is more efficient but may introduce slight inaccuracies.

The study by [88] compares the two methods for mooring lines connected to a wave energy converter. The DCM involved hydrodynamic analysis to determine the FOWT's RAOs, which were then used in mooring simulations. The FCM, on the other hand, considered the entire system's response within the same software. Although both methods produced comparable motion responses at the HOP, differences emerged further along the mooring due to coupled effects. The FCM showed higher stress cycles and fatigue damage, leading to a preference for this method. Additionally, [89] found that the DCM tends to overestimate maximum motion responses.

Although these studies provide insights into the dynamics of mooring systems connected to wave energy converters, the applicability of these findings to flexible pipes connected to FOWT requires consideration. Mooring lines and flexible pipes, for example, show different properties leading to different restoring effects. Furthermore, wave energy converters are designed to harness energy through motion, typically optimized for high amplitude oscillations in heave, pitch, and surge. In contrast, FOWTs, are designed to minimize these motions to stabilize the platform. The mass of FOWTs is substantially larger than that of most wave energy converters, contributing to significantly higher inertia. This larger inertia moderates the response to environmental forces, reducing the relative motion between the platform and the pipe. In addition, while mooring lines are typically deployed in catenary configurations, the pipe configuration in this study uses a lazy wave setup. The use of BMs is specifically intended to decouple the pipe's motion from that of the FOWT, mitigating the impact of platform movement on critical points like the TDP and HOP [40].

These differences suggest that the DCM, while introducing inaccuracies due to its separate consideration of component interactions, might be adequate for the simulation of flexible pipes in FOWT setups, especially when buoyancy aids are employed. This approach offers a practical balance between computational efficiency and the need for accuracy. Given these possible differences, an examination of these coupling effects in the context of an FOWT is provided.

Simulations were conducted using the reference case. Two scenarios were simulated over a 3-hour sea state, focusing on differences in design constraints of tension and curvature. The discrepancies between the two methods were analyzed at every time step at the the transition form buoyant to non-buoyant section for tension and at the TDP for curvature. These two locations were chosen as they exhibited the largest response differences over a 3-hour sea state simulation. The maximum observed differences were 5% for tension and 10% for curvature at similar time steps (averaged over the simulation time; 0.25% for tension and 0.75% for curvature). When comparing the maximum tension and curvature across the entire simulation period, the largest discrepancies were 0.5% for tension and 4% for curvature.

In the following section, the comparison between the DCM and FCM, along with an analysis of discrete versus distributed buoyancy, will be further explored. In the following section, the analysis will delve deeper into these peak differences between the DCM and FCM, as well as the impacts of discrete and distributed buoyancy. This aims to demonstrate how the most realistic and simplified scenarios affect the accuracy and reliability of the response.

3.4.5. Discrete and distributed buoyancy section comparison

As detailed in section 3.2.6, the BM in the buoyancy section can be configured either as distributed or discrete buoyancy. Distributed buoyancy uniformly spreads buoyancy along the pipe's entire section, whereas discrete buoyancy places BMs at specific intervals. This distinction is important as discrete buoyancy provides a more realistic representation by capturing the variable responses based on BM placement and spacing.

For this comparative analysis, figures 3.12 display the tension and curvature for two scenarios: one employing the FCM with discrete buoyancy and the other using the DCM with distributed buoyancy (similar locations as mentioned in 3.4.4). The FCM scenario simulates the most realistic conditions possible, whereas the DCM scenario is a simplified method.

These differences indicate that while the simplified scenario used throughout this research provides lower response outputs in both tension and curvature, it necessitates adjustments in design constraints to accommodate these discrepancies. The maximum observed differences were 5% for tension and 30% for curvature at similar time steps (averaged over the simulation time; 0.75% for tension and 25% for curvature). When comparing the maximum tension and curvature across the entire simulation period, the largest discrepancies were 0.5% for tension and 22% for curvature. These measurements were taken at a single point along the pipe, which showed the largest differences. Therefore, they may not represent variations across other locations.

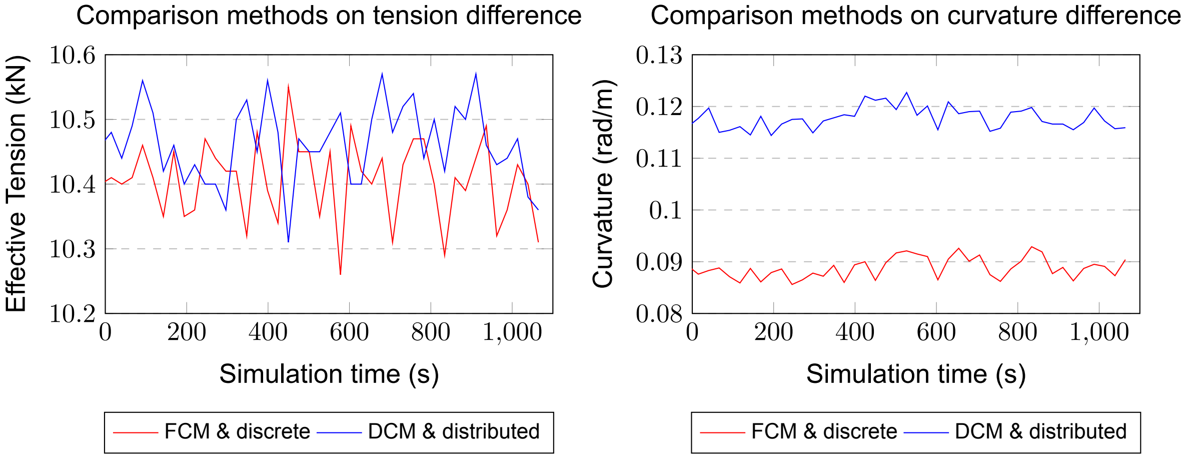

(a) Effect on tension

(b) Effect on curvature

Figure 3.12: Comparison for the FCM with discrete buoyancy and DCM with distributed buoyancy

The comparison of discrepancies from section 3.4.4 with those previously mentioned shows that tension discrepancies remain consistent. For both comparisons, the maximum observed differences at a single time step and their overall maximum during the simulation show discrepancies of 5%. This indicates that the replacement to distributed buoyancy has a minor effect on tension, and thus primarily influenced by the shift to the DCM method. Conversely, for curvature, replacing to distributed buoyancy significantly impacts the results, suggesting that this change affects curvature more than the shift of coupling method. The discrepancies in curvature increased three times for the maximum observed difference at a single time step and five times for the maximum difference across the full simulation. This suggests that curvature discrepancies are mainly influenced by the replacement of distributed method, while tension discrepancies are predominantly driven by the shift of coupling method.

In response to these findings, a utilization factor of 30% is applied to the predefined MBL and MBR limits to account for the simplifications introduced by using DCM with distributed buoyancy. This factor is based on dynamic analysis, where the differences in surface area between distributed and discrete buoyancy influence the drag and added mass forces acting on the pipe. A smaller utilization factor might be more suitable for static scenarios, given the absence of dynamic external forces. However, the 30% approach is considered conservative, especially considering the lower observed maximum differences across the simulation time. However, these measurements were taken at a single location, while the largest curvature discrepancies between distributed and discrete buoyancy configurations are likely to occur at the pipe-to-BM connection in the discrete method. This effect would be more pronounced in dynamic scenarios, potentially leading to larger differences. Therefore, applying the most conservative discrepancy observed is considered a reasonable precaution to account for unobserved locations where greater variances may arise

3.4.6. Environmental study

The environmental conditions impacting the system's performance are examined. The metocean conditions, design codes for an FOWT, load cases, and FOWT responses also explored.

3.4.6.1. Modeling of metocean conditions

For the metocean data, in-house sources from Vattenfall provided a 23-year time series with a 3-hour interval, although the specific location used in this research remains confidential.

In this research, wind conditions are simplified due to the disassembly of the turbine blades, which affects the RNA. Here, wind is modeled solely as thrust or drag force (F_{thrust} or F_{drag}). Consequently, wind effects are only on the platform, tower, and struts. This approach reduces the influence of wind since the aerodynamic force is concentrated at RNA, and other structural exposed surfaces to wind are relatively small. A constant wind profile, derived from the API spectrum, calculates wind speeds above sea level using the power law, utilizing wind speed measurements as input. The wind speed, denoted by V with corresponding subscripts to the conditions, is measured at 10 meters above sea surface. This model does not account for wind gusts, as their impact is minimal on the relatively small exposed surface areas.

The behavior of water surface waves is inherently complex and stochastic, often represented in sea state models as a random superposition of waves with varying amplitudes, frequencies, and phases. This randomness is captured by spectral density functions, for which the JONSWAP spectrum is particularly suitable [45]. This spectrum models the energy distribution across wave frequencies for a fully developed sea, employing parameters such as the significant wave height H_s, peak wave period T_p, and peak enhancement factor γ. The enhancement factor describes the peakedness of the wave spectrum, with higher values indicating a greater concentration of energy around the peak frequency, resulting in more pronounced waves. At this location, the significant wave height does not exceed 9 meters, and the peak period is less than 18 seconds.

Ocean currents are influenced by a variety of factors [90]. In the absence of detailed field measurements, a simplified method using a depth-averaged (2D) model can be employed to approximate current speeds.This model integrates the surface current speeds with a depth-average factor to effectively simulate the conditions expected at various depths. This method is especially effective in regions known for complex current patterns, such as this location. Current speed, denoted by U with appropriate subscripts, is measured at the surface and averaged down to 200m, where at depths beyond 200m, current magnitudes are assumed to be similar to those at 200m.

The location-specific wave, wind, and current roses, and wave scatter diagram are depicted in figure 3.13. The prevailing wind and wave direction is South-West, while the current flows Northeast, directly opposite. The alignment between wind and wave suggests that the waves are locally wind-generated. The misalignment of the current with respect to the wind and wave can be explained by the mixture of two seas where local wind, density, and pressure influence the currents. To determine which conditions and directions will be used in this research, further simplifications will be made. Simulating every possible combination is computationally impractical. Therefore, an alternative approach is taken by calculating a single metocean condition derived from omni-directional conditions. This will be further discussed in the coming sections.

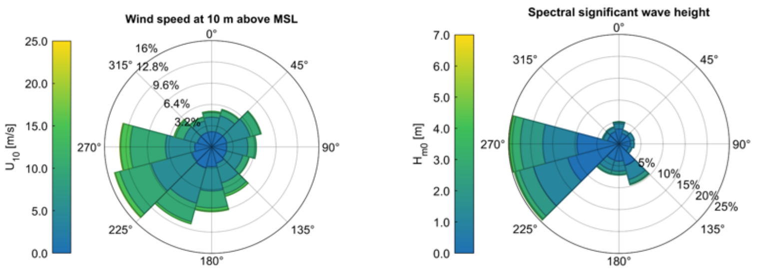

(a) Wave rose

(b) Wind rose

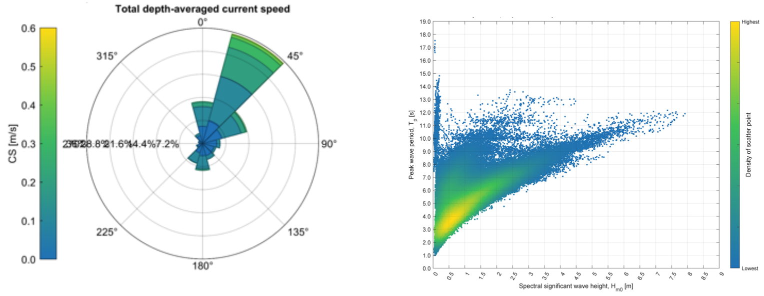

(c) Current rose

(d) Wave scatter plot

Figure 3.13: Metocean data

3.4.6.2. Design codes FOWT

The design process for flexible pipes requires compliance with criteria formulated in four limit states: serviceability, ultimate, accidental, and fatigue limit states [91]. The serviceability limit state ensures that the pipe remains operational. The ULS requires that the riser withstand extreme environmental conditions, without rupture but not necessarily remain operational. The accidental limit state addresses ULS due to infrequent, accidental loads and the fatigue limit state concerns damage from cyclic loading. This research focuses on design concerning the ULS.

Environmental conditions considered in the design process, as outlined by [92], include all natural phenomena such as wind, waves, current, and water level. These phenomena may be interdependent, with their respective directions potentially governing the design. The standard categorizes environmental conditions into an “environmental class”. Load Cases (LCs) for flexible pipes in the oil and gas industry, as specified by [42], involve functional, environmental, and accidental loads during installation, normal, or abnormal service conditions. Typically, a global analysis combines a 100-year wave with a 10-year current in mean, near, and inline offset positions. However, this approach is specifically designed for floating oil platforms and does not account for the unique conditions of FOWTs. Therefore, the decision is made to adhere to the Design Load Cases (DLCs) specified for FOWTs. This approach is also applied to the design of mooring lines [93]. In this context, a variety of LCs must be evaluated under different conditions. Relevant standards [44] [94] provide minimum DLCs that account for these environmental factors.

Therefore, an important aspect of the design basis is transforming site-specific conditions into relevant LCs. Several design conditions are listed in [92] as DLCs: power production, power production with a fault occurrence, startup, normal shutdown, emergency shutdown, parked (idle), parked with fault conditions, and transport, assembly, maintenance, and repair. However, not all DLCs are equally applicable. Therefore, two main DLCs are considered particularly relevant: power production and parked condition [93] [95]. The power production (DLC 1.6a and 1.6b) is associated with a severe sea state and a normal wind and current model, while the parked condition (DLC 6.1a and 6.1b) is associated with an extreme sea state combined with an extreme wind and current model. The overview of these DLCs is presented in table 3.6.

Table 3.6: Design load cases

Design situation	DLC	Wind	Turbine thrust/drag	Sea state	Current	Directional
Power production	1.6a	V_{rated}	F_{thrust} at V_{rated}	H_s at V_{rated}	U_{1-yr}	Co-& Uni-directional
	1.6b	$V_{cut-out}$	F_{thrust} at $V_{cut-out}$	H_s at $V_{cut-out}$	U_{1-yr}	
Parked condition	6.1a	$V_{50-year}$	F_{drag} at $V_{50-year}$	$H_{s,50}$	U_{5-yr}	Misaligned & Multi-directional
	6.1b	V_{5-year}	F_{drag} at V_{5-year}	$H_{s,5}$	U_{50-yr}	

To limit the number of possible environmental conditions, the design scenario inducing the highest loading and bending on the pipe will be investigated. The DLCs focus on different directionalities with respect to different combinations of wind, wave, and current. The roses in figure 3.13 show that the wind speed, wave height, and current speed do not have their highest probability of occurrences in similar directions. However, omni-directional metocean conditions are used, which result in wave/wind/current parameters with their values in every direction specified as their highest observed [96]. The probability of these three parameters to have their absolute highest value in similar directions is thus low, however, most interesting as this provides the most extreme response resulting in a conservative approach. The design scenario that has the most significant impact on design constraints is identified and used for the parametric study. Taking omni-directionality into account, the environmental conditions are as follows listed in table 3.7.

Table 3.7: Omni-directional environmental conditons

	Paramater	Symbol	Unit	Value	Comment
Wind speed	Rated	V_{rated}	m/s	10.59	[65]
	Cut-out	$V_{cut-out}$	m/s	25	[65]
	50-year	V_{50-yr}	m/s	33.1	[82]
	5-year	V_{5-yr}	m/s	29.7	[82]
Thrust/drag	at V_{rated} & $V_{cut-out}$	F_{thrust}	MN	2.9	Operating condition [65]
	at V_{50-yr} & V_{5-yr}	F_{drag}	MN	1.27	Parked condition [65]
Wave height	at V_{rated}	$H_{s,rated}$	m	4.2	T_p = 8.3 s & γ = 2 [82]
	at $V_{cut-out}$	$H_{s,cut-out}$	m	8.1	T_p = 11.7 s & γ = 2.3 [82]
	50-year	$H_{s,50-yr}$	m	8.1	T_p = 12.2 s & γ = 2.3 [82]
	5-year	$H_{s,5-yr}$	m/s	7.3	T_p = 11.6 s & γ = 2.3 [82]
Current speed	1-year	$U_{1,yr}$	m/s	1.04	Extreme current model; Normal current model unavailable [82]
	5-year	$U_{5,yr}$	m/s	1.18	[82]
	50-year	$U_{50,yr}$	m/s	1.4	[82]

3.4.6.3. Simulation load cases and selection of environmental parameters

In power production, the wind, wave, and current directions are aligned (uni-directional), while in the parked condition, a misalignment of ±30 degrees between the wind and wave directions is considered as per [44]. This misalignment is applied across 30-degree intervals for wind, wave, and current directions. Given the symmetrical layout of the FOWT, directionality is evaluated from 0 to 180 degrees in 30-degree increments for both power production and parked conditions. The directional LCs for power production (DLC 1.6a and 1.6b) have 7 cases each, while the parked condition setups (DLC 6.1a and 6.1b) have 36 cases each. The environmental conditions are misaligned as wind/wave/current at 30/0/0, 0/30/0, 0/0/30, 30/30/0 degrees, etc. In total, 84 LC are analyzed for their impact on tension and curvature, as shown in figures 3.14a and 3.14b. Tension is evaluated at the HOP, SB-HB transition (transition from non-buoyant to buoyant section), HB-TDP transition (transition from non-buoyant to buoyant section), and TP, while curvature is assessed at the BS, SB, HB, and TDP. Each load case is represented by specific wind, wave, and current directions indicated by three coordinates on the x-axis in the figures. These coordinates follow the same sequence for wind, wave, and current directions, respectively.

The analysis indicates that tension is generally less impacted by environmental conditions than curvature. The most significant tension variations occur at the HOP, while curvature is most affected at the BS and TDP. Large variations in curvature are observed due to the FOWT's offset. Comparing DLC 1.6a and 1.6b (power production) and DLC 6.1a and 6.1b (parked conditions), higher responses were consistently noted in the ”b” scenarios. For power production, the stronger wind and wave conditions contribute to increased tension at the HOP and curvature at the BS. In parked conditions, smaller wind and wave forces, combined with stronger currents, primarily impact the curvature at the BS, leading to increased output results, while tension remains relatively unchanged.

Consequently, due to the larger responses in both tension and curvature, only DLC 1.6b and 6.1b are considered for further analysis. For these scenarios, when comparing different environmental direction combinations within each design situation, a clear trend emerges. At a 0-degree environmental alignment, the largest curvature responses are observed at the BS and TDP. Misaligned conditions result in a reduction in curvature response, with minimal changes in tension. This holds for both uni-directional and misaligned situations. At a 180-degree directionality, the pipe is stretched, leading to a smoother curvature at the HOP and TDP, but with a slight increase in tension. Thus, the largest curvature responses are observed when the environmental conditions are aligned with the pipe layout.

The significant curvature response at the BS suggests that this is not developed adequately. Due to the impact on curvature and the relatively consistent tension response, the decision is made to prioritize DLC 1.6b with inline metocean conditions (0,0,0 direction). This choice is further supported by the fact that the parked condition simulations do not account for an empty pipe; instead, they assume similar internal fluid conditions as in power production. As a result, the empty pipe conditions in the parked scenario have not been fully captured, making power production the most reliable scenario for this decision.

Comment: During this analysis, the decoupled aerodynamic loading with the single-point force at the RNA had not been implemented with correct directionality. Therefore, only the wind loading on the surface components changed direction, while the point force remained fixed at a 0-degrees.

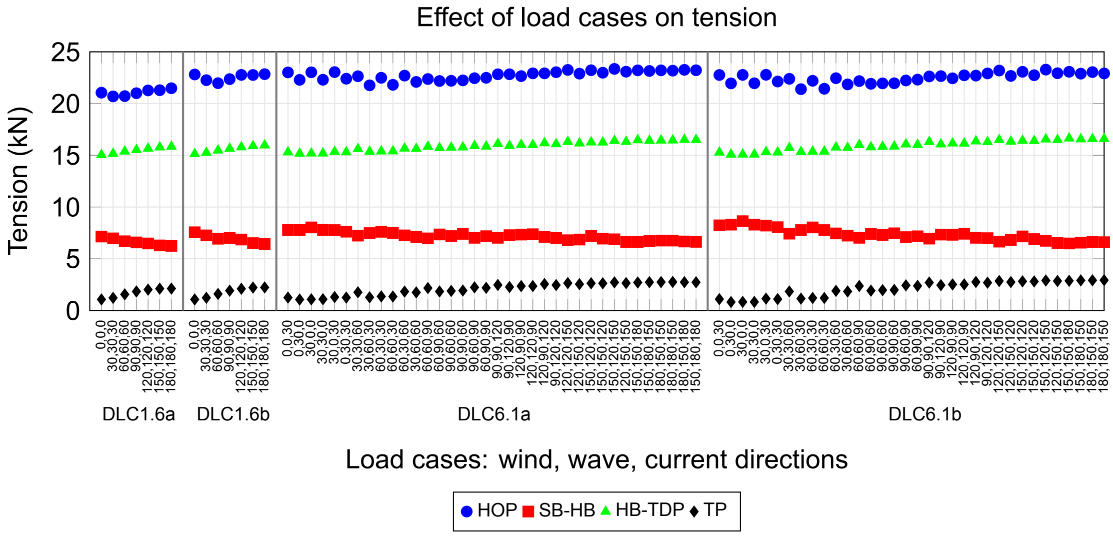

(a) Tension metric

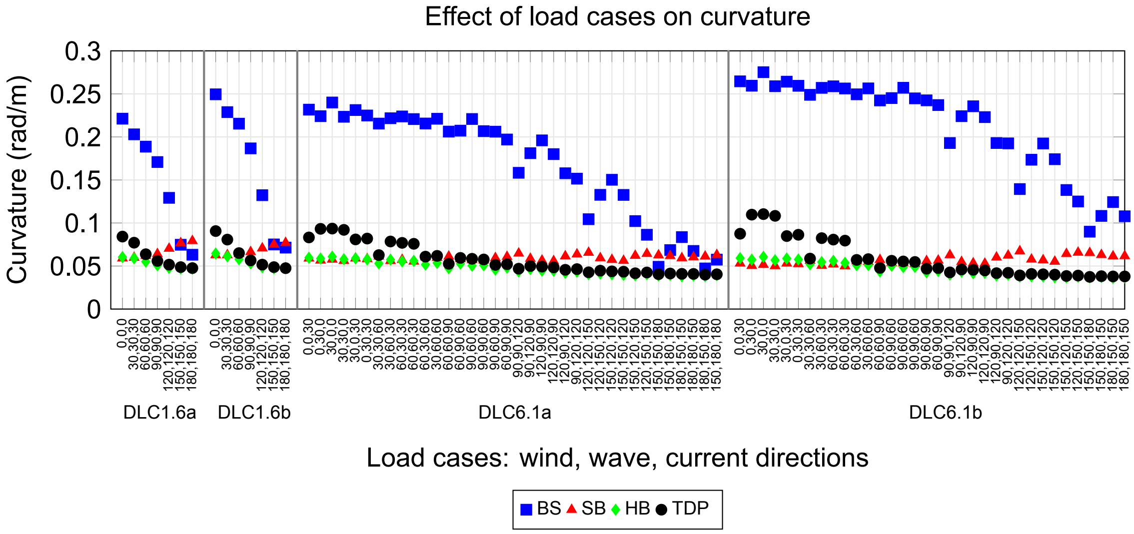

(b) Curvature metric

Figure 3.14: Results of various load cases on tension and curvature along different points of the pipe length

DLC 1.6b, characterized by in-line environmental conditions, exhibits the most significant impact on this specific configuration and layout. The selected environmental parameters further used in this research are detailed in table 3.8, and visualized in figure 3.15

Table 3.8: Selected environmental parameters

Paramater	**Symbol**	**Unit**	**Value**
Wind speed	V_{rated}	m/s	25
Thrust force	F_{thrust}	MN	2.9
Significant wave height	H_s	m	8.1
Peak wave period	T_p	s	11.7
Peak enhancement factor	γ	-	2.3
Current speed	U	m/s	1.04
Wind/wave/current direction	-	°	0

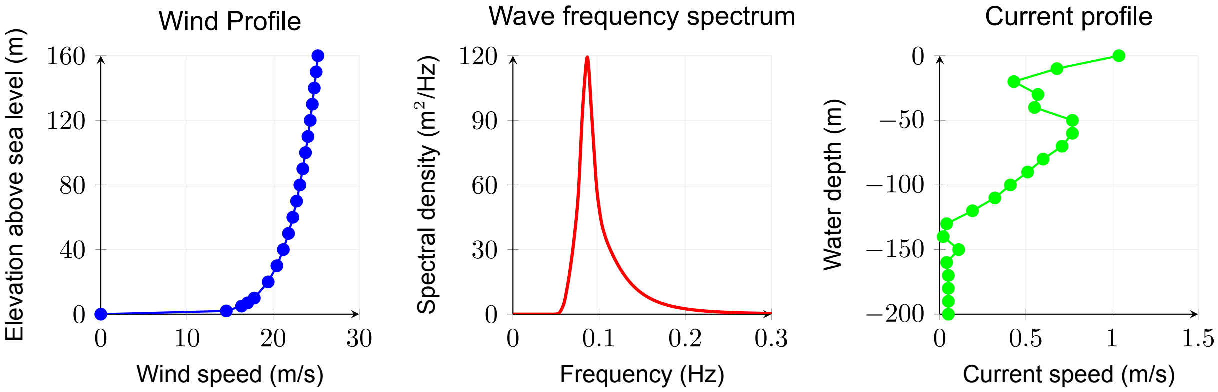

(a) Wind speed profile **(b)** Spectral density of wave **(c)** Horizontal current profile

Figure 3.15: Environmental profiles for selected environmental parameters

3.4.6.4. FOWT responses to wave conditions

To identify potential sea states causing motions at the connection point, the FOWT's response to various wave frequencies is analyzed using RAOs (Response Amplitude Operators), which depend on the vessel's size, mass, wave direction, and period [97] (see appendix B.6).

Given the symmetrical design of the semi-submersible in the x-y plane, wave directions at 0, 60, and 90 degrees are evaluated. For translational motions, resonance peaks are observed at wave periods exceeding 19 seconds. For rotational motions, resonance peaks in pitch and roll are also above 18 seconds across all directions. However, at 0 and 90 degrees, there is a response amplitude at a wave period of 8 seconds—specifically for pitch at 0 degrees and roll and yaw at 90 degrees. The yaw amplitude could potentially induce torsional motions, but based on [97] and [72], the primary influence is the heave motion, as it generates the largest forces on the connected pipe. Therefore, these smaller amplitude peaks in rotational motions are noted but not further investigated.

According to the wave scatter diagram, the peak wave period at this location has its lowest probability at 18 seconds. Resonance peaks for all motions, except yaw, are above 19 seconds, making resonance unlikely due to the infrequent occurrence of such wave periods. While extreme sea states could still pose a risk, a comprehensive assessment based on extreme value theory [98] is beyond the scope. The analysis of wave frequencies and RAOs thus did not align since different peak periods are observed. Consequently, the LC analysis provided the environmental conditions governing the metocean conditions that excited the most extreme responses.

3.4.7. Development of bend stiffener

In previous analyses in this section, the from BS from the reference case was adopted, however, these components are typically customized for specific applications. Therefore, this requires development of the BS for the hypothetical flexible pipe in combination with the selected environmental conditions specified in section 3.4.6.3. Material properties like density, Young's modulus, and Poisson's ratio are consistent with those used in the reference case. Additionally, parameters like the tip length (L_{tip}), tip thickness (t_{tip}), and clearance gap between the pipe and BS are based on in-house DPC applications, derived at 20 mm, 20 mm, and 30 mm, respectively [82]. The tip dimensions must ensure a smooth transition from the BS to the pipe while maintaining sufficient thickness to prevent vulnerability, and the clearance gap allows for water exchange between components.

For the BS development, the primary design parameters are the length (L_{BS}) and base diameter (D_{base}) [99]. The pipe must not experience over-bending, suggesting that larger dimensions might be preferable to minimize fatigue. However, smaller lengths and diameters are often preferred for several reasons:

- Reduced shear force and bending moment at the base connection.
- Easier connection, installation, and spacing.
- Lower costs.
- Fewer thermal issues.

For this development, BS lengths between 1 and 10 m and base diameters between 0.3 and 1 m were simulated, resulting in 80 different BS dimensions. Maximum dimensions are based on manufacturer availability and recommendations [56] [82], while minimum dimensions are based on the reference case BS, which showed curvature peaks indicating it was not suitably developed. The goal is to achieve minimal curvature along the BS length, with the peak curvature centered in the middle. If the peak curvature occurs at the connection point or tip, the BS is ineffective, as it fails to dissipate the bending moment properly, making these points prone to fatigue failure. Therefore, successful BS designs are those where the peak curvature is centered along the length of the BS.

Figure 3.16 presents the results of all BS dimension combinations regarding base diameter and length. In figure 3.16a, the maximum normalized curvature is shown, while figure 3.16b illustrates the position along the length where this maximum curvature occurs.

The maximum curvature varies from 0 (the lowest curvature) to 1 (the limit). A color gradient from green (lowest) to red (highest) is used to visually represent these values. Green cells indicate lower curvature compared to other scenarios, and from this figure, it is evident that larger base diameters and lengths result in lower maximum curvature. The position is expressed as a percentage relative to the total length, measured from its based. A curvature peak at 50% is ideal, as it suggests optimal distribution of bending moments. Consequently, the color gradient is green at 50%, transitioning to red as the peak moves farther from the center. Furthermore, some scenarios show a position outside the length of the BS, coloured in black, which makes these designs ineffective. A higher percentage value indicates that the peak curvature is closer to the tip. For example, for a BS with a 7 m length, base diameters of 0.8 and 0.9 m result in the curvature closer to the tip, making smaller base diameters more desirable as they center the peak. The figures also reveal a clear distinction between suitable and unsuitable combinations. Larger base diameters with shorter lengths tend to push the curvature outside the BS, while smaller diameters and longer lengths bring the peak curvature closer to the base. Only a few BS designs pass the criteria of having the curvature near the middle, further emphasizing the need for a careful design process.

From a financial perspective, shorter lengths are preferred. In figure 3.16b, the green, yellow, and orange cells represent scenarios where the curvature does not occur near the ends, making them more favorable. Among these, scenarios with green and yellow are of particular interest, resulting in six potential BS designs. To determine the best design, the BS with the lowest maximum curvature is selected, leading to the choice of a BS with a length of 6 m and a base diameter of 0.7 m. In comparison to other suitable BS designs, smaller lengths and diameters resulted in higher curvature peaks, while larger dimensions had little effect on the maximum curvature. This combination demonstrates that curvature values stabilize while the position remains near the center, making it the most optimal BS for this base case configuration.

Note that different configurations or environmental conditions may require adjustments to the dimensions, as BS designs must account for factors such as tension, angle, temperature, interface details, riser end-fitting profiles, diameter, stiffness, MBR, and fatigue requirements [82]. The BS dimensions used further in this research are listed in table 3.9. For the complete dataset of curvature magnitudes and peak positions, see appendix B.7.

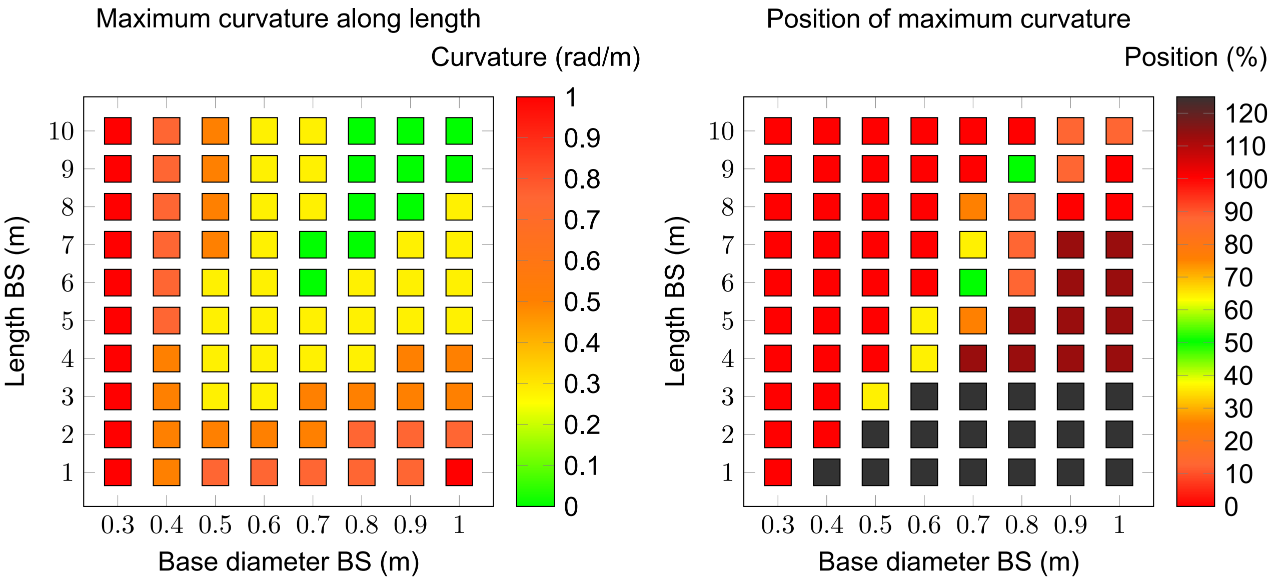

(a) Maximum normalized curvature along the length of the BS (0 = best, 1 = worst)

(b) Position of maximum curvature along the length of the BS (0% = base, 100% = tip)

Figure 3.16: Comparison of 80 test scenarios showing maximum normalized curvature (left) and the corresponding positions where this curvature occurs (right)

Table 3.9: Properties for the developed BS

Properties	Symbol	Unit	Value
Length	L_{BS}	m	6
Diameter base	D_{base}	m	0.7
Diameter tip	D_{tip}	m	0.2622
Length tip	L_{tip}	m	0.2
Thickness tip	t_{tip}	m	0.02
Clearance gap	-	m	0.03

3.4.8. Convergence study of simulation parameters

Finally, OF simulations require various simulation parameters which are sensitive to its performance. This evaluation focuses on two main criteria: the accuracy of results and computational efficiency. Accuracy refers to the closeness of simulated results to expected outcomes, while computational efficiency relates to the time required to run a single simulation. A balance between these two criteria is essential, as improving one often compromises the other. Therefore, a convergence study was conducted to identify parameter values that achieve converging results while minimizing computational time. The key simulation parameters considered include:

- **Time step:** This parameter discretizes the time domain for simulations. Smaller time steps improve accuracy but increase computational costs, while larger steps may cause numerical instability. Adjusting the time step to capture dynamic events accurately while avoiding numerical errors is important.
- **Target segment length:** This determines the segment size in the lumped mass model. Smaller segments enhance accuracy but demand more computational resources, while larger segments

reduce computational load at the cost of realism.

- **Build-up time:** The build-up period gradually introduces the sea state and vessel motions, smoothing the transition into the simulation. To avoid peak stresses from abrupt initialization, a longer build-up time is recommended, typically set to at least one wave period.
- **Simulation time:** The total simulation duration must be sufficient to capture the system's response under varying conditions. OF allows the simulation to be divided into stages, ensuring a smooth transition from static to dynamic conditions (see appendix B.8). The time-stepping algorithm evaluates mass, damping, stiffness, and loads at each step, reflecting the time-varying geometry of the system.

Table 3.10 outlines the simulation parameters and their respective test values. These values are selected based on the authors knowledge and prior recommendations [76, 82] (see appendix B.8 for all test values). Each parameter is adjusted individually to evaluate its effect on simulation performance, ensuring that the impact of each variable is clearly understood. To select applicable simulation parameters, the base values are initially used, and each parameter is varied sequentially. Once a developed parameter value, such as the time step, is identified, it is applied consistently in all subsequent tests. The next parameter is then varied while using the previously developed paramter(s), with base value(s) maintained for those yet to be varied. This approach fine-tunes the simulation to achieve the best balance between accuracy and computational efficiency.

Table 3.10: Simulation parameters and properties for the convergence study

Parameter	**Unit**	**Base value**	**Min value**	**Max value**	**Number of test values**
Time step	s	0.1	0.05	0.6	10
Target segment length non-buoyant section	m	1	0.2	10	12
Build-up time	s	120	60	1000	9
Simulation time	s	120	120	10800	12

The outcomes of the convergence study evaluate the simulation performance based on various metrics, presented in two distinct graphs as follows:

- **Wall clock time for the FOWT and the pipe:** This metric reflects the actual time taken to complete one simulation for the FOWT or the pipe, measured in seconds. Since the platform and pipe simulations are de-coupled, the wall clock time is shown separately for each. The FOWT's time focuses on motion analysis, while the pipe's time focuses to structural analysis.
- **Tension and Curvature Accuracy:** This metric measures tension and curvature at the same eight locations as described in the environmental study (tension at HOP, the SB-HB transition, the HB-TDP transition, and TP; curvature at BS, SB, HB, and TDP). The visualization in the graphs represents the percentage differences in curvature and tension separately for two test values. These percentage differences are averaged over the four locations, resulting in a single outcome for the relative differences between the compared test values. This visualization identifies the test values at which the relative differences converge, highlighting the converged simulation parameters. For the full dataset of all outcomes per test value, rather than the averaged relative difference, see appendix B.8.

This convergence employs the reference case configurational parameters (section 3.3) in combination with environmental parameters selected from the environmental study (section 3.4.6). However, the developed BS (section 3.4.7) is not adopted due to faulty simulation implementation. The convergence analysis focuses on multiple locations for metric comparison and measures the relative increase between test values, which helps mitigate this error. The simulation parameters are individually reviewed based on the aforementioned metrics.

Time step

The time step has minimal impact on tension and curvature results, as the percentage difference between the smallest and larger values remains below 0.5%, as shown in figure 3.17. For lower values, the computational cost is low, but as the time step increases, the computational time also rises due to the recalculation required for missed iterations, indicating instability. This is evident from time steps beyond 0.4 seconds. Larger values than 0.6 seconds resulted in failed simulations. The time step between 0.2 and 0.35 seconds shows the lowest wall clock times for both the FOWT and the pipe. Although the most accurate representation is at 0.05 seconds due to the large number of iterations, the closest percentage difference to this value is observed at 0.2 seconds. Therefore, a time step of 0.2 seconds is chosen as the optimal value, aligning with previous studies [74].

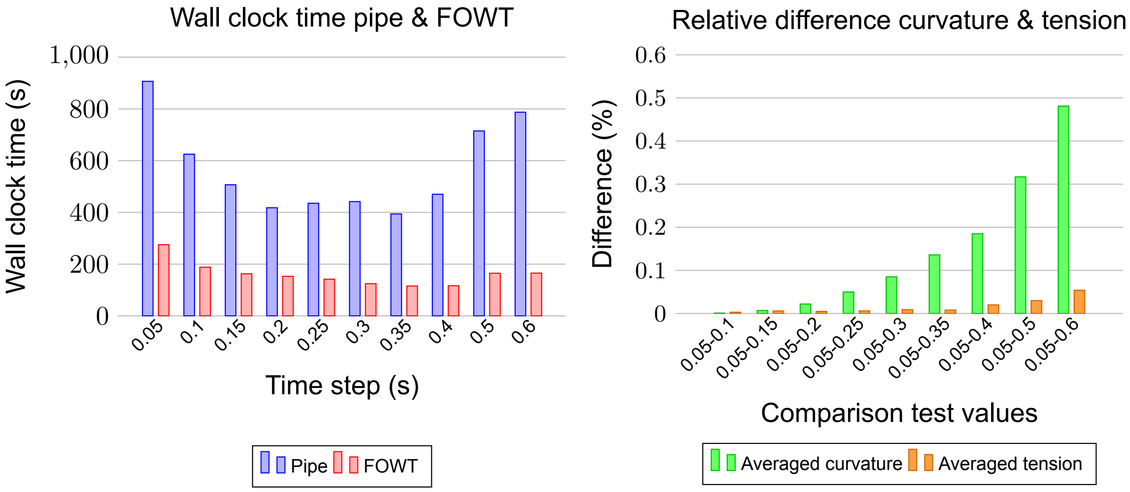

(a) Comparison of wall clock times for the pipe and FOWT simulations across different time steps

(b) Relative difference in curvature and tension between two time steps

Figure 3.17: Convergence on time step

Target segment length

The resolution of the buoyant section is always half the segmentation length compared to the non-buoyant section [82], and the resolution of the BS is consistently set to 0.05 m [23]. The target segment length shows a noticeable influence on tension and curvature, as depicted in figure 3.18. The most significant difference is observed in the wall clock time of the pipe for lower segmentation lengths (does not affect the FOWT). Smaller segment lengths result in a larger number of nodes, leading to more iterations, while larger segment lengths result in higher inaccuracies, as indicated by greater differences in curvature explained by unrealistic bends in the pipe. Based on a compromise where the wall clock time converges and curvature differences are minimal, a segment length of 2 meters is chosen. Larger values could reduce accuracy without significantly improving computational efficiency.

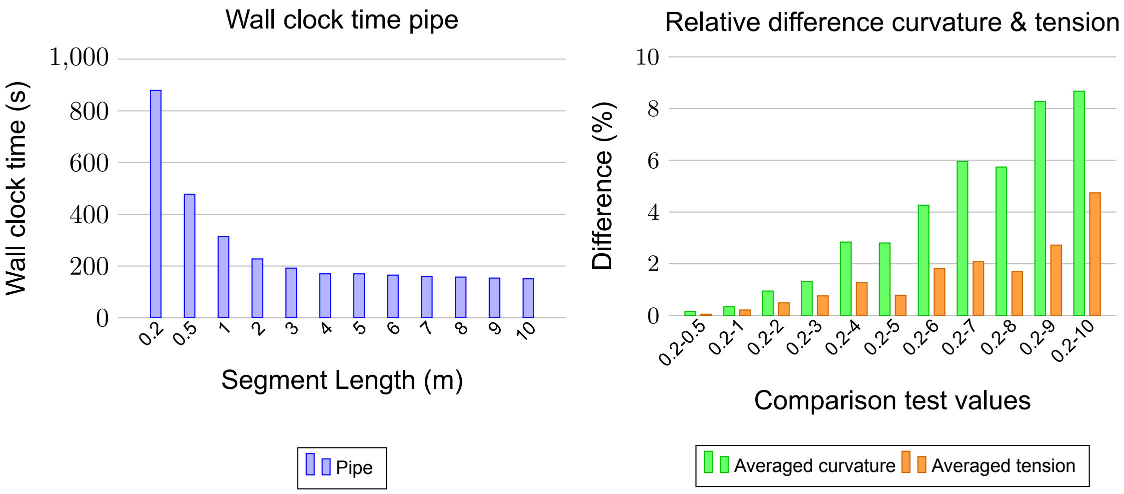

(a) Comparison of wall clock times for the pipe and FOWT simualtions across different segment lengths

(b) Percentage difference in curvature and tension between two segmentation lengths

Figure 3.18: Convergence on segmentation length

Build-up time
Figure 3.19 shows that varying the build-up time has a minimal effect on wall clock time, but it impacts tension and curvature. A longer build-up time is recommended as it provides a smoother transition to the simulation phase, thereby reducing the occurrence of peak motions early in the simulation. The slight decrease in computational cost from reducing build-up time does not justify the potential loss in accuracy. The difference between short and long build-up times may seem minor, but it can significantly influence curvature and tension. The minimum build-up time is typically set at least one wave period [85], with no maximum explicitly defined. At 720 seconds, the wall clock time is minimized, while the percentage difference is close to the 1000-second mark. This provides accurate results without significantly increasing computational costs. Although larger values than 1000 seconds could have been tested since tension and curvature have not fully converged.

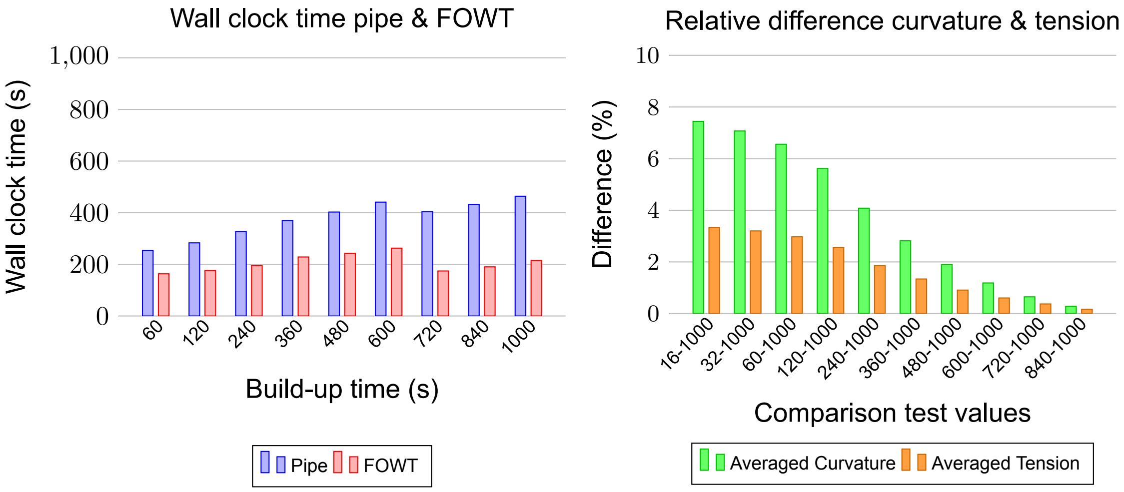

(a) Comparison of wall clock times for the pipa and FOWT simulations across different build-up times

(b) Relative difference in curvature and tension across two build-up times

Figure 3.19: Convergence on build-up time

Simulation time
For the simulation time, computational time increases significantly with longer durations. The simulation time must be sufficient to capture different wave frequencies and amplitudes, which provide a good representation of long-term operation. This is typically defined as a 3-hour sea state in wave statistics [100, 101], after which the sea state is assumed to be stationary. At 3600 seconds, the curvature and tension begin to stabilize, while extending the simulation time further increases computational cost without significantly improving accuracy. Shorter simulations drastically reduce wall clock time but at the

cost of increased inaccuracies in tension and curvature. See figure 3.20 for the results of the simulation time.

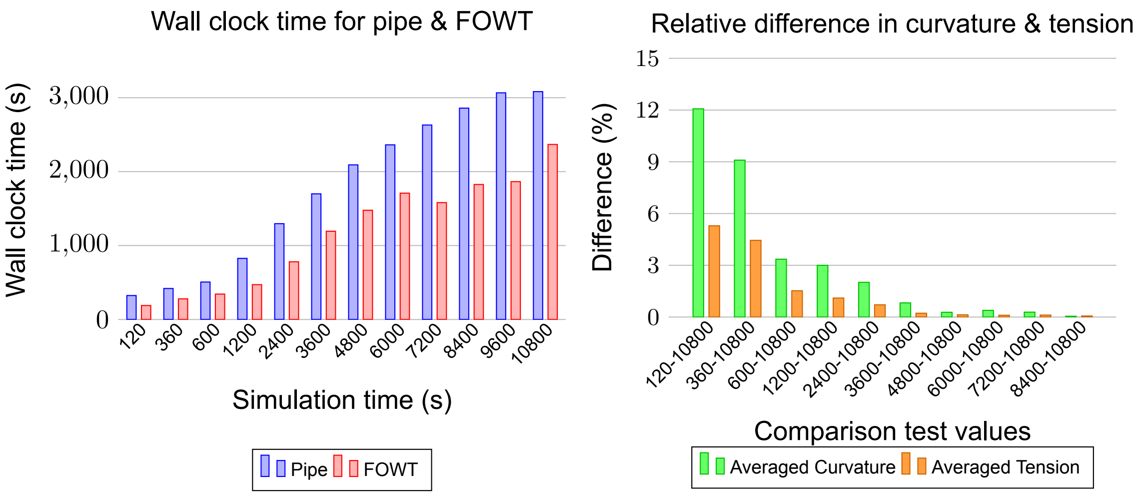

(a) Comparison of wall clock times for the pipe and FOWT simulations across different simulation times

(b) Percentage difference in curvature and tension across two simulation times

Figure 3.20: Convergence on simulation time

The developed simulation parameters further used in this research are outlined in table 3.11. While it is essential to explore the impact of different environmental and geometrical conditions on these simulation parameters, the values identified here will be used throughout the remainder of this research.

Table 3.11: Developed simulation parameters

Parameter	**Unit**	**Value**
Time step	s	0.2
Target segment length non-buoyant section	m	2
Build-up time	s	720
Simulation time	s	3600

3.5. Evaluation Criteria

To assess various configurations, the global configuration of a lazy wave is first explained, followed by the established boundary conditions. Additionally, distinctions between static and dynamic contributions are discussed.

3.5.1. Global configuration

The free-hanging catenary method is fast and accurate, making it preferred for representing configurations [86]. The lazy wave configuration can be obtained using the catenary method since it is inherently a catenary with BM's. The internal force acting on point B is equal to that at points D and F since there is no vertical shear force. This results that the gravity of segment BC is equal to the buoyancy of segment CD, and the buoyancy of segment DE is equal to the gravity of segment EF. This ensures that the gravity of segment BC equals the buoyancy of segment CD, and the buoyancy of segment DE matches the gravity of segment EF. Consequently, this leads to the catenary segmentation of lengths AB, CD, DE, and EF, see figure 3.21

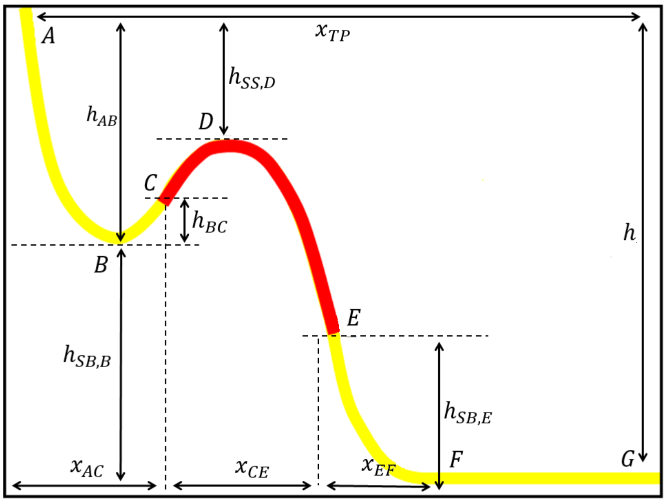

Figure 3.21: Configuration distances for the lazy wave configuration

3.5.2. Boundary conditions

The boundary conditions differentiate between physical and operational constraints, detailed in table 3.12. Physical constraints are denoted as the boundary conditions provided by the limits of the pipe, while operational constraints are denoted as the conditions imposed by the limits of movement during operation.

Regarding the operational criteria: A clearance of 50 meters from the sea surface is maintained to prevent collisions, maritime traffic disruptions, and reduce wind-driven current impacts [102], denoted as the Sea Surface Clearance (SSC). Additionally, a 10-meter clearance from the seabed is required to mitigate hydrodynamic effects [103] and prevent structural failure due to potential seabed collisions, denoted as the SeaBed Clearance (SBC).

Regarding the physical criteria, as discussed in section 3.4.4, the DCM with distributed buoyancy exhibited a 30% discrepancy compared to the FCM with discrete buoyancy. To account for this, a 30% utilization factor is applied to both the MBL and MBR as a conservative measure. According to industry standards [31, 104], a safety factor of 1.5 is recommended for the MBR, and a 67% safety factor for the MBL under operational conditions. The maximum allowable curvature is determined by the inverse of the MBR.

Table 3.12: Boundary conditions of the pipe

Properties	**Symbol**	**Unit**	**Safety Factor**	**Utilization Factor**	**Value**
Sea Surface Clearance	SSC	m			50
Seabed Clearance	SBC	m			10
Minimum Breaking Load	MBL	kN	2/3	30%	251
Minimum Bend Radius	MBR	m	3/2	30%	3.3

The evaluation criteria can simplified into normalized equations with maximum allowable values set to 1. The normalized tension and curvature are given by equation 3.15 and 3.16. For the SSC, only point D in section 2 is likely to exceed this limit, as shown in equation 3.17. For the SBC, sections 1 and 2 can exceed the limit at SB (point B) and the furthest BM (point E), as shown in equation 3.18. The SSC and $h_{SS,D}$ are measured as absolute values from the sea surface, while the SBC, $h_{SB,B}$, and $h_{SB,E}$ are measured as absolute values from the seabed.

1. $$\frac{T_e}{MBL} < 1 \tag{3.15}$$

   where $T_e > 0$

2. $$\frac{C}{MAC} < 1 \tag{3.16}$$

   where $MAC = \dfrac{1}{MBR}$

3. $$\frac{SSC}{h_{SS,D}} < 1 \tag{3.17}$$

4. $$\frac{SBC}{h_{SB,B}} < 1 \quad \text{and} \quad \frac{SBC}{h_{SB,E}} < 1 \tag{3.18}$$

$$\tag{3.19}$$

3.5.3. Static vs dynamic contribution analysis

To evaluate a configuration, differences between static and dynamic analysis are addressed. Static analysis accounts for the weight and buoyancy of the pipe, while dynamic analysis considers additional external forces such as wind, waves, currents, and FOWT motion. This dynamic loading influences the pipe's shape, altering curvature and tension. Both operational and physical criteria are thus evaluated to ensure structural integrity.

The results of these analyses, discussed in section 4.1, compare the static contributions derived from static analysis with the dynamic contributions calculated from the differences between the dynamic and static analyses. For scenarios under consideration, it is essential that the pipe avoids contact with the seabed or sea surface and maintains a lazy wave configuration throughout.

For example, dynamic conditions can alter the pipe's effective tension and configuration, leading to increases in maximum effective tension during dynamic scenarios compared to static conditions, as observed in [105]. This underscores the importance of understanding dynamic contributions under external loading conditions. Additionally, from the simulation time in the dynamic analysis the maximum value of the output response is used, representing the greatest potential dynamic contribution and assessing the system's maximum capacity.

3.6. Parametric Study

This section presents an evaluation of the parametric study. It begins by explaining the decision on the configurational parameters of the the lazy wave. Next the setup for the parametric study is outlined, including variations in water depth. Finally, preliminary responses are shown, and the setup for the sensitivity analysis is provided.

3.6.1. Decision configurational parameters

This section discusses the variance of parameters included in the parametric study. To limit the scope and address the impact of these variables effectively, the set of variable parameters is determined. The pipe properties, provided by the manufacturer NOV (section 3.2.4), are kept constant. The environmental study (section 3.4.6), focuses on the load case, with environmental parameters held constant to reflect. Additionally, the developed BS (section 3.4.7) remain unchanged, as they are are not the primary focus of this research. Consequently, the focus of this parametric study is on the configuration shape of the lazy wave, with the following list of parameters shaping the analysis:

- The outer diameter of the BM (OD_{BM}).
- The number of BM (n_{BM}).
- The pitch between the BM (d_{BM}).
- The length of the first section of the pipe (L_1).

- The length of the second section of the pipe (L_2).
- The length of the third catenary section of the pipe ($L_{3,cat}$).
- The length of the static horizontal section of the pipe (L_{st}).
- The total length of the pipe (L_{total}).
- The horizontal distance between HOP and TP (X_{TP}).

The BS has a specified constant length L_{BS} adjusted to the model of the developed scenario, which is included in the length of the first section L_1.

The total length of the pipe is given by equation 3.20 and illustrated in figure 3.22a. The lengths $L_{3,cat}$ and L_{st} are interdependent, such that $L_{3,cat} + L_{st} = L_3$. Given that L_{total} is determined based on the recommended vertical distance from HOP to seabed and considering the analysis of parameters L_1 and L_2, L_3 can be disregarded according to this equation's criteria.

$$L_{Total} = L_1 + L_2 + L_3 \tag{3.20}$$

To investigate the second section of the pipe, interdependence on the length of its section and the number and pitch of the BM is given in equation 3.21 and shown in figure 3.22b. Rather than examining the three parameters separately, it is decided to consider the number of BM as the variable parameter, correlated with the length of the buoyancy section itself.

$$L_2 = (n_{BM} - 1) * d_{BM} \tag{3.21}$$

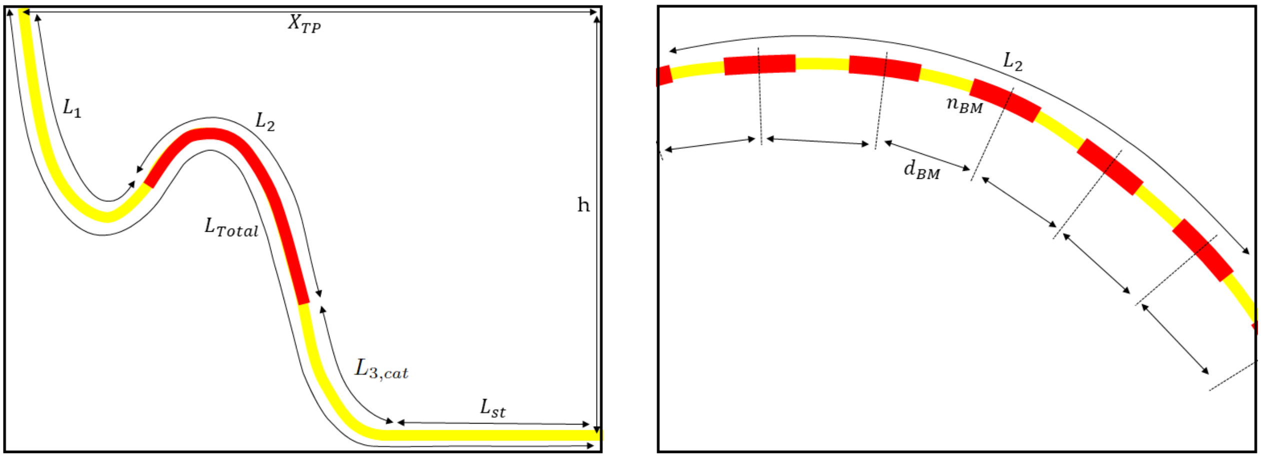

(a) Parameters for the lazy wave configuration

(b) Parameters for the second section

Figure 3.22: Configuration parameters

Finally, this results in six parameters being important for investigation, which provides the basis for the parametric study.

3.6.2. Parametric set-up for 200m water depth

For the parametric study, the reference case is adopted, incorporating all developed components and conditions as specified in the subsequent analyses in section 3.4. This developed scenario is now denoted as the base case, which contains base values for the six configurational parameters. Table 3.13 provides an overview of the parameters utilized with their accompanying base value and test scenarios. The minimum, maximum, and step size chosen are guided by the author's intuition. This results in a total of 137 tested scenarios. The fifth parameter variation, L_{total}, is is linked to the variation of L_3. For the full dataset of all test values, see appendix C.2.

Table 3.13: Parametric variable set-up for 200m water depth

Parameter	Symbol	Unit	Base value	Min value	Max value	Step size	Number of scenarios
Outer diameter BM	OD_{BM}	m	0.73	0.2	1	0.025	32
Pitch BM	d_{BM}	m	6	1	12	1	12
Length first section	L_1	m	126	10	200	10	30
Length second section	L_2	m	126	10	200	10	20
Total length*	L_{total}	m	504	354	624	10	31
Termination point	X_{TP}	m	360	230	480	25	11
* Length third section	L_3	m	252	102	402	10	31

To provide a generalized output, the decision parameters will be presented as ratios relative to other key parameters. These ratios are detailed in table 3.14 (for the full range of test values see appendix C.1). The decision parameters are varied according to the test scenarios outlined in 3.13, while the related parameters are held constant at their base values. Specifically, the outer diameter of the BM is related to the pipe's outer diameter, which is 0.16022m. The pitch of the BM is related to the length of the second section, the lengths of the first, second, and third sections are related to the total pipe length, and both the total length and the TP are related to the vertical distance from the HOP to the seabed, all as specified at their base values in table 3.3 and table 3.13.

Table 3.14: Parametric variable set-up in ratios

Parameter	Ratio	Base value	Min value	Max value	Step size
Outer diameter BM	$\frac{OD_{BM}}{OD_{pipe}}$	0.73	1.2	6	0.15
Pitch BM	$\frac{L_2}{d_{BM}}$	6	126	10	-
Length first section	$\frac{L_1}{L_{total}}$	126	0.02	0.6	0.02
Length second section	$\frac{L_2}{L_{total}}$	126	0.02	0.4	0.02
Total length*	$\frac{L_{total}}{h}$	504	2	3.6	0.06
Termination point	$\frac{X_{TP}}{h}$	360	1.3	2.7	0.14
* Length third section	$\frac{L_3}{L_{total}}$	252	0.3	0.6	0.02

The variations in the geometrical shape of the pipe are visualized based on the static analysis in figure 3.23 for all parameters. Not all ratios and scenarios are depicted; only a selected few are shown. This is illustrated for a water depth of 200m, where the mean positions are represented on the x and y axes.

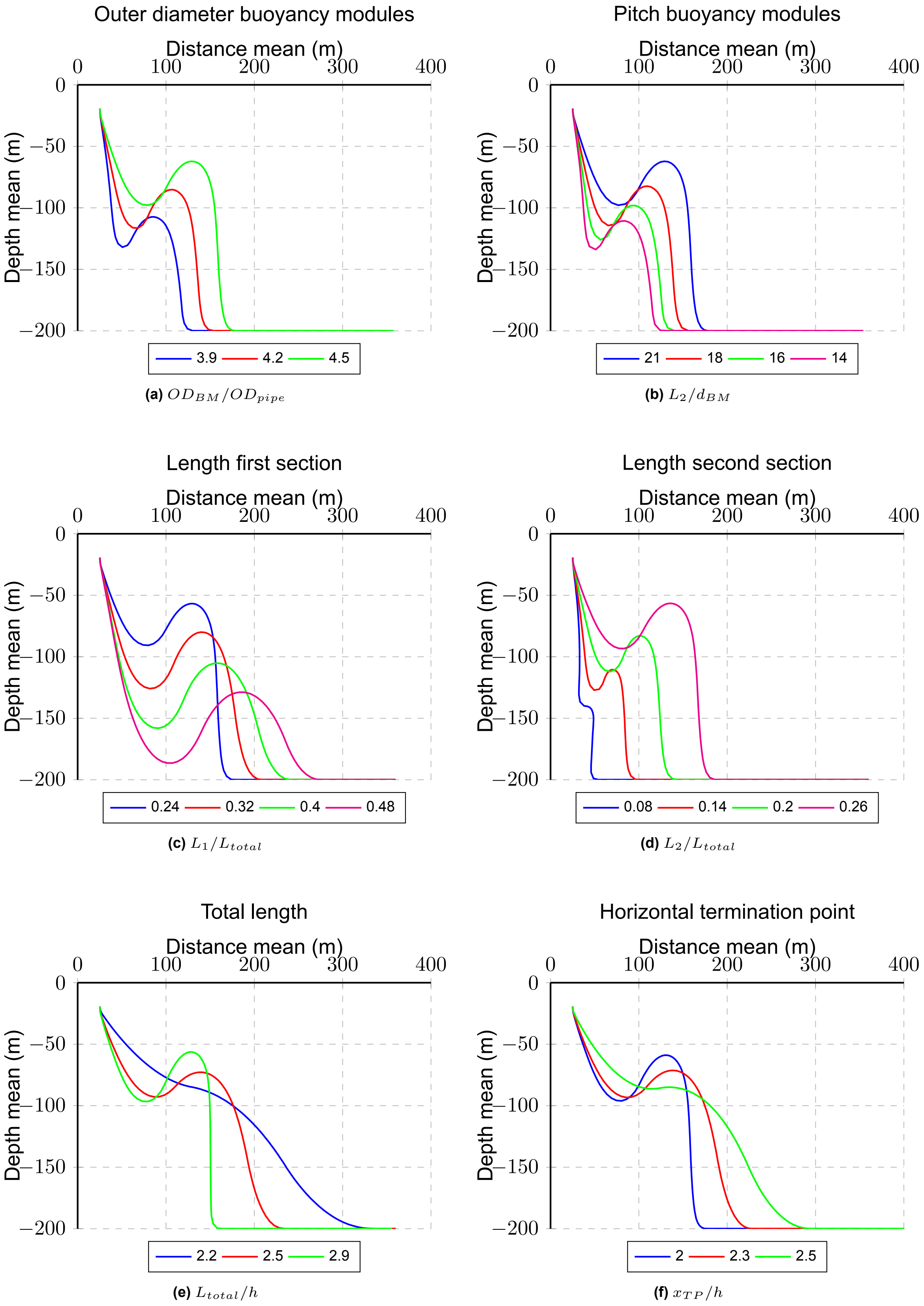

(a) OD_{BM}/OD_{pipe}

(b) L_2/d_{BM}

(c) L_1/L_{total}

(d) L_2/L_{total}

(e) L_{total}/h

(f) x_{TP}/h

Figure 3.23: Geometrical shapes of parameter variations

3.6.3. Parametric set-up for 400m and 600m water depth

To examine the influence of water depth, the base case is adapted to depths of 400m and 600m, using the same rule of thumb applied at 200m, while maintaining consistency in all other parameters. The adjusted parameters for the 400m and 600m depths are listed in table 3.15.

Table 3.15: Properties of the base case for 400m and 600m water depth

Properties	Symbol	Unit	Value		Comment
Water depth	d	m	400	600	
Draft	T	m	20	20	
Vertical distance	h	m	380	580	$h = d - T$
Total length	L_{total}	m	1064	1624	$L_{total} = 2.8 * h$
Length first section	L_1	m	266	406	$L_1 : L_2 : L_3 = 1 : 1 : 2$
Length second section	L_2	m	266	406	$L_1 : L_2 : L_3 = 1 : 1 : 2$
Length third section	L_3	m	532	812	$L_1 : L_2 : L_3 = 1 : 1 : 2$
Termination point	X_{TP}	m	760	1160	$X_{TP} = 2 * h$

In table 3.13, the parametric setup for a 200m water depth is presented with decision parameters expressed as ratios. These same ratios will be applied to the water depths of 400m and 600m. The test scenarios, including their base values, minimums, maximums, and step sizes, are detailed in table 3.16. See appendix C.2 for the full data set of test values for 400m and 600m water depth.

Table 3.16: Parametric variable set-up for 400m and 600m water depth

Parameter	Symbol	Unit	Base value	Min value	Max value	Step size	Number of scenarios
			Water depth = 400m				
Outer diameter BM	OD_{BM}	m	0.73	0.2	1	0.025	32
Pitch BM	d_{BM}	m	6	2.1	27	2	12
Length first section	L_1	m	266	21	633	21	30
Length second section	L_2	m	266	21	422	21	20
Total length*	L_{total}	m	1064	747	1381	21	31
Termination point	X_{TP}	m	760	486	1013	53	11
*Length third section	L_3	m	532	215	849	21	31
			Water depth = 600m				
Outer diameter BM	OD_{BM}	m	0.73	0.2	1	0.025	32
Pitch BM	d_{BM}	m	6	3	41	3	12
Length first section	L_1	m	406	32	967	32	30
Length second section	L_2	m	406	32	644	32	20
Total length*	L_{total}	m	1624	1141	2107	32	31
Termination point	X_{TP}	m	1160	741	1547	81	11
*Length third section	L_3	m	812	329	1295	21	31

3.6.4. Visualisation of output responses

The base case of 200m water depth is illustrated in figure 3.24. It assesses the geometrical shape along with the the absolute maximum tension and curvature throughout the full length of the pipe. Observations indicate that the highest tension value is present at the HOP, designated as point A. Subsequent significant peaks in tension occur at point E, the transition from section 2 to section 3, and point C, the transition between section 1 and section 2. Curvature analysis reveals peaks at several points: point A (the BS), point B (the SB), point D (the HB), and point F (the TDP). Therefore the subsequent results focus specifically at Points A, C, E, G for tension, and Points A, B, D, F for curvature.

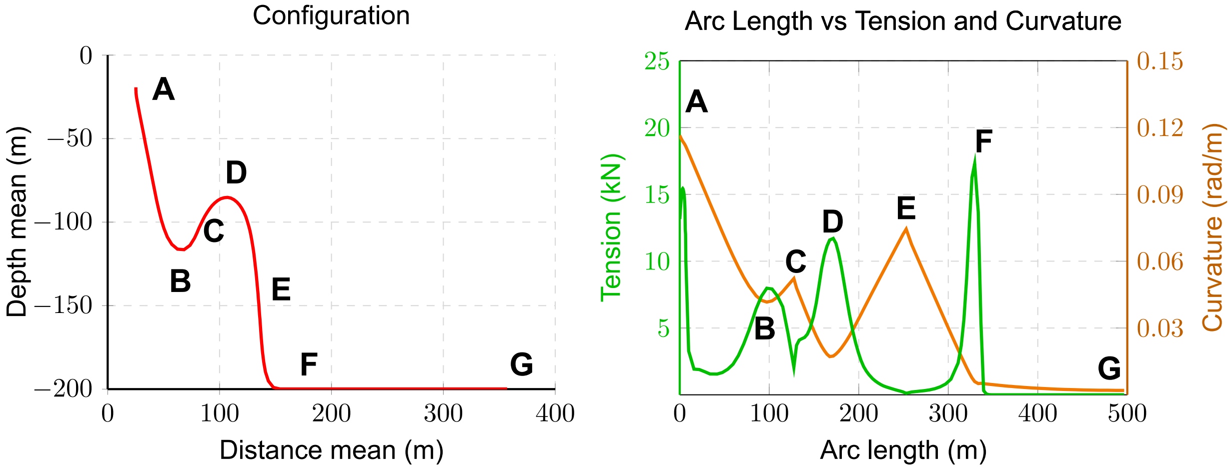

(a) Geometrical shapes of parameter variations **(b)** Graph of arc length vs tension

Figure 3.24: Base case scenario for 200m water depth

The tensions and curvatures for the base cases at 400m and 600m water depths show similarities across these depths; however, tension and curvature exhibit distinct behavior. Figures 3.25a reveals that the variance in water depth impacts these points differently; notably, point A experiences the most significant increase in tension with deeper water depths, followed by point E. Points C and G show minimal changes, with point G being the least affected. Figure 3.25b shows that point A shows relatively consistent curvature across all water depths, indicating a stable response to environmental changes at this location. In contrast, Points B, D, and F exhibit lower curvature values, which increase as the water depth increases. Maximum values for tension and curvature can occur at different locations under different scenarios, hence, this analysis of peak values at specific points is important.

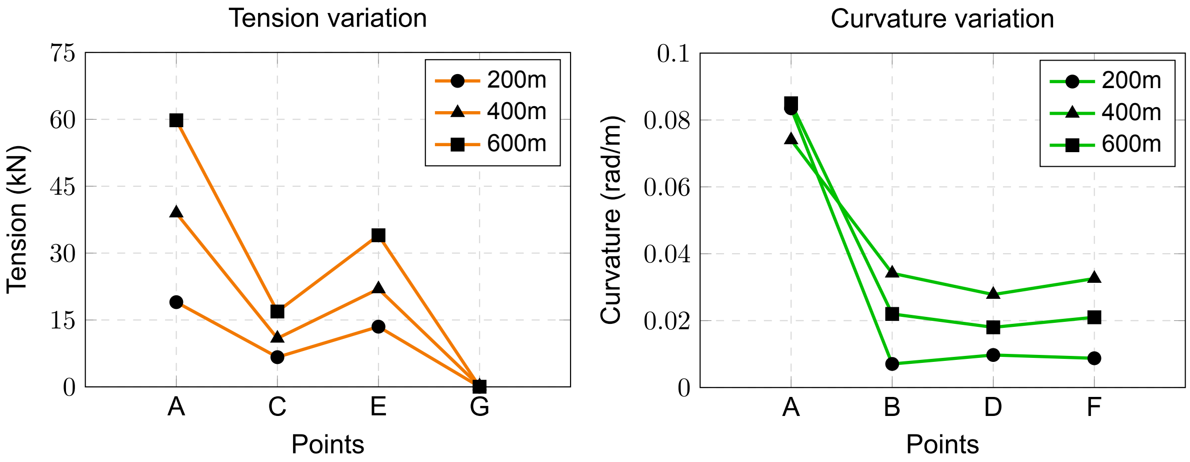

(a) Comparison of tension at different points and water depths **(b)** Comparison of curvature at different points and water depths

Figure 3.25: Trends of maximum tension and curvature for base case at different water depths

3.6.5. Sensitivity analysis set-up

In the parametric study, a variety of scenarios are tested and compared. Due to time constraints, the sensitivity analysis employs the same scenarios and results from the parametric study. This analysis utilizes the base values of the parameters and the corresponding tension and curvature values at depths of 200m, 400m, and 600m. In the parametric study, the base value is altered by either increasing or decreasing in a defined step size. The parameter variations are constrained by minimum and maximum limits to adhere to the boundary conditions. These limits define the allowable ranges within which a parameter can vary.

From the setup of the parametric study, it is noted that different scenarios do not use similar step sizes. Therefore, the sensitivity analysis makes a comparison by assuming linearity. This approach involves averaging over combinations of scenarios that exhibit a 10% increase or decrease in parameters. Similar combinations are then used to determine the corresponding changes in tension and curvature. The analysis distinguishes between points where maximum tension and curvature are observed. This provides a rate of increase or decrease for these variables for a 10% variation in parameters. This determined rate thus focuses on all possible combinations within the allowable range.

For comparative purposes, the sensitivity of different parameters concentrates on this rate of increase or decrease from its base value. The analysis, however, averaged the sensitivity across various scenarios, rather than using the base value as starting point. By employing the predefined allowable ranges, this provides a visualization that contrasts different parameters. These ranges additionally constrain unrealistic rates and magnitudes since it incorporated a combination of all values rather than solely relying on the rate from base value. In addition, only the dynamic analysis is utilized in this sensitivity assessment, as the static analysis has yielded comparable sensitivity responses.

4

Results

In this chapter, an overview of the comparison between the static and dynamic contributions is first provided in section 4.1. Section 4.2 then presents a comprehensive overview of all evaluation criteria for all simulations. Following this, the parametric variations at a 200m water depth are elaborated on in section 4.3, and the impact of different water depths is addressed in section 4.4. Finally, the analysis of sensitivity is detailed in section 4.5.

4.1. Static and Dynamic Contribution

The differentiation between static and dynamic contributions is made based on operational and physical criteria, which are elaborated separately.

4.1.1. Operational criteria

For operational criteria, clearance gaps at the sea surface and seabed are assessed at specific points: the sag bend (point B), the hog bend (point D), and the transition from buoyant to non-buoyant section (point E), as visualized in figure 4.1. The differences per parameter variation across three water depths are examined, considering all scenarios that meet the boundary conditions and which form a lazy wave. Within a single parameter variation these scenarios are considered, with their height differences averaged.

In dynamic analysis, the minimum clearance positions are used for points D and E, while the maximum is used for point B. This reflects the shifts observed in dynamic analysis, where the its mean position moves downward at points D and E, and upward at point B. Consequently, the height differences at these points are captured at their largest deviations, rather than at similar time points.

The height differences across different water depths generally follow similar magnitudes. They are averaged over all scenarios as follows: -1.5m at point B (with -1.4m at 200m, -1.5m at 400m, and -1.7m at 600m), +0.9m at point D (with +1m at 200m, +0.8m at 400m, and +0.9m at 600m), and -0.3m at point E (with -0.5m at 200m, -0.2m at 400m, and -0.1m at 600m). The greatest variances are observed at point B due to the heave motion of the FOWT, which directly links the translational vertical motion to this point.

Point B exhibits greater effects in deeper water. Point E is more affected in shallower water which can be attributed to the neglected scaling effect of current loading at depths of 400m and 600m. Point D shows increased effects in deeper water; however, due to large variations at L_{total} and x_{TP} at 200m, configuring in a nearly straight geometrical shape, this trend does not hold. Excluding these outlier scenarios, which are undesirable due to their diminishing effect on the lazy wave, it can be concluded that point D is more affected in deeper water. Therefore, without considering these outliers at 200m and acknowledging the neglected scaling of current loading at 400m and 600m, the geometric shape is more affected in deeper water.

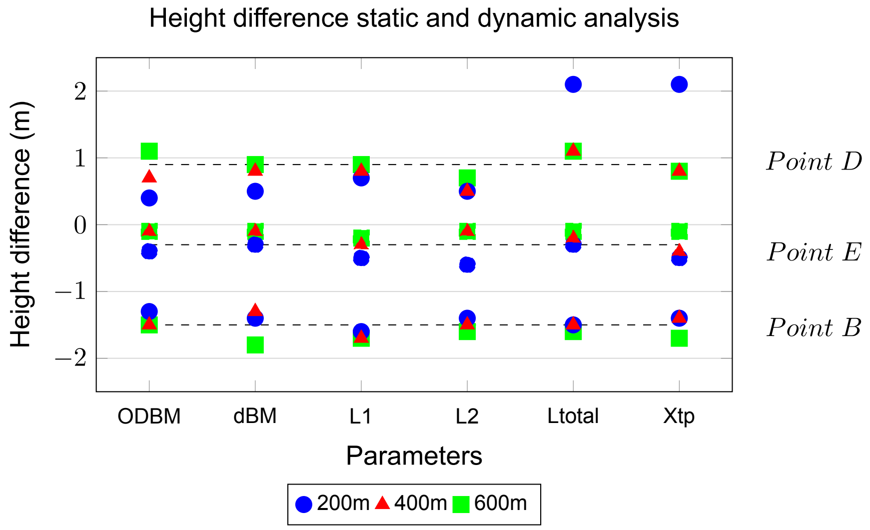

Figure 4.1: Height difference at points B, D and E between static and dynamic scenarios, averaged over scenarios within a single parameter variation

4.1.2. Physical criteria

Figure 4.2 provides a comparative analysis of the dynamic contributions to tension and curvature at various points along the pipe. For tension, these points include the HOP (point A), the transition from non-buoyant to buoyant (Point C), point E, and the TP (point G). For curvature, the points analyzed are point A, point B, point D, and the TDP (point F). Each point includes six values representing the averaged dynamic contribution from that specific parameter variation. This approach facilitates visualization of trends in dynamic contributions across potential configurations rather than detailing variations by individual parameters. For parameter-specific visualizations, see appendix D.1.

Figure 4.2a shows that across all locations and scenarios, the dynamic contribution to overall tension decreases with increasing water depth. From 200m to 400m to 600m, the averaged dynamic contributions across all scenarios are as follows: at point A 32%, 20%, 19%; at point C 30%, 18%, 16%; at point E 6%, 3%, 1%; and at point G 20%, 5%, 3%. This decrease in deeper water is due to a increase in static contributions in combination with a decrease in dynamic contributions, leading to a smaller overall dynamic impact.

In shallower waters, dynamic contributions vary more significantly than in deeper waters. Points A and C show the highest dynamic contributions, reflecting their proximity to areas where the highest horizontal wave particle velocity is. Point E exhibits the lowest dynamic contributions. Notably, at point G, despite being near the seabed, the dynamic contribution remains relatively significant in shallower waters. This indicates that dynamic environmental influences affect the entire length of the pipe, particularly in shallower waters, whereas in deeper waters, the dynamic contribution at point G diminishes.

Figure 4.2b demonstrates the varying behavior of dynamic contributions at different points and water depths. From 200m to 400m to 600m, the averaged dynamic contributions across all scenarios are: at point A 31%, 42%, 44%; at point B 25%, 9%, 7%; at point D 29%, 18%, 18%; and at point F 15%, 7%, 6%. As water depth increases, the geometry scales such that horizontal distances increase, thereby reducing the overall static contribution to curvature at all points. However, behavior across points varies.

Specifically, at point A, the static contribution decreases more rapidly than the dynamic contribution, which results in a relatively higher impact of the dynamic contribution in deeper water. The highest dynamic contribution to curvature are observed at this point, which can be explained due to the direct link to the movement of the FOWT. Conversely, at points B, D, and F, the dynamic contribution decreases at a faster rate than the static contribution, thus resulting relatively smaller impact in the dynamic contribution to lower environmental effects. Additionally, point F shows the smallest deviation with respect to water depth in dynamic contribution.

Comparing the results of tension and curvature, averaged over all locations and water depth, the dynamic contribution to tension is 14% (22% at 200m, 12% at 400m and 10% at 600m) and to curvature is 22% (28% at 200m, 19% at 400m and 19% at 600m). The largest dynamic contributions are noted at point

A for both criteria. Deeper waters show a larger deviation in dynamic contribution to curvature, making tension less susceptible to variations in water depth regarding its dynamic contribution. This results in a more consistent behavior of tension and a larger variability of curvature to dynamic contribution across water depths.

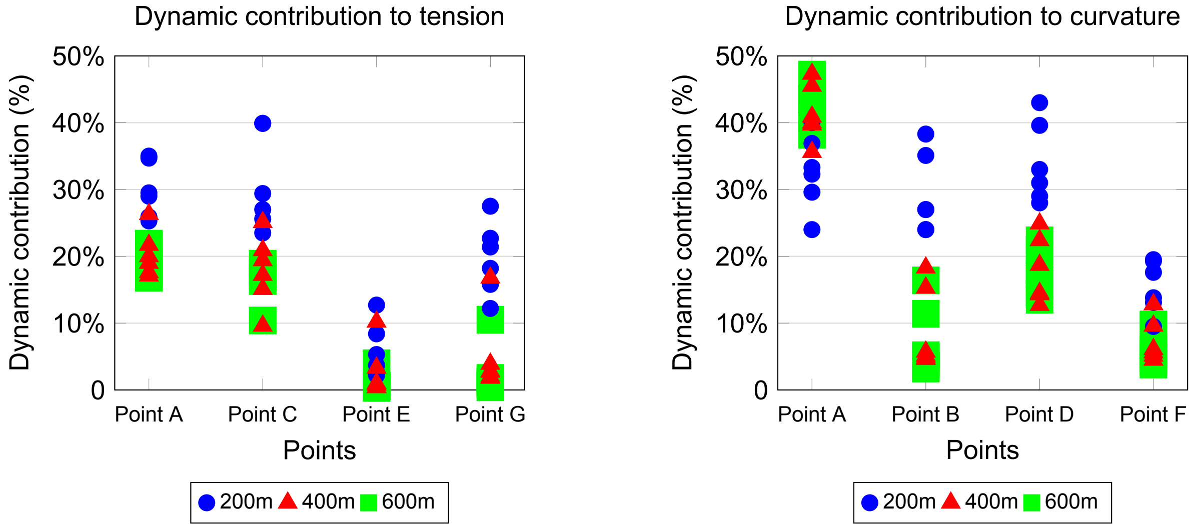

(a) Dynamic contribution to the maximum tension

(b) Dynamic contribution to the maximum curvature

Figure 4.2: Dynamic contributions to tension and curvature at different points, averaged over scenarios within a single parameter variation, resulting in six values per point

4.2. Evaluation All Tested Scenarios

Figure 4.3 presents the results of all tested parameter variation scenarios. The normalized criteria from section 3.5.2, including operational constraints (clearances at points D, B, and E) and physical constraints (maximum tension and curvature along the pipe), are depicted. A limit value of 1 indicates the maximum permissible values for each criterion, with variations shown across three water depths: 200m, 400m, and 600m. For OD_{BM}, 33 scenarios were tested, 12 for d_{BM}, 30 for L_1, 20 for L_2, 31 for L_{total}, and 11 for x_{TP}. The figure includes catenary configurations, particularly visible when clearances at point E are exceeded, though it does not distinguish between catenary and lazy wave configurations or tension and curvature relationships. Despite appearances, not all scenarios passed each criterion. For example, OD_{BM} at 200m shows many points, but only five scenarios passed. The figure visualizes all scenarios within each water depth, regardless of whether one criterion failed. Therefore, this offers overall trend rather than strict correlations of the criteria.

Scattered points within a criterion indicate how one parameter affect the configuration. A wider scatter shows greater impact, while narrower scatter reflects less variation. Clearance at point D is exceeded most frequently, particularly in shallower waters due to the decreasing distance with depth. Point D also exhibits the greatest variation across scenarios. For seabed clearance, minimal variation across depths suggests consistent behavior, while surface clearance is more depth-dependent. Tension increases with water depth, while curvature generally decreases and converges. Exceedances in tension and curvature primarily occur in L_{total} and x_{TP} for stretched or slacked scenarios. Curvature at L_1 shows high values when the lazy wave reaches the sea surface. Some extreme scenarios with exceedingly high values are excluded, and the figure does not account for compression. Notably, the largest variations in clearance occur in OD_{BM}, d_{BM}, L_1, and L_2, while L_{total} and x_{TP} show smaller variations.

Each parameter will be discussed in detail in the following section. See appendix D.2 for the evaluation criteria across scenarios separately at all water depth.

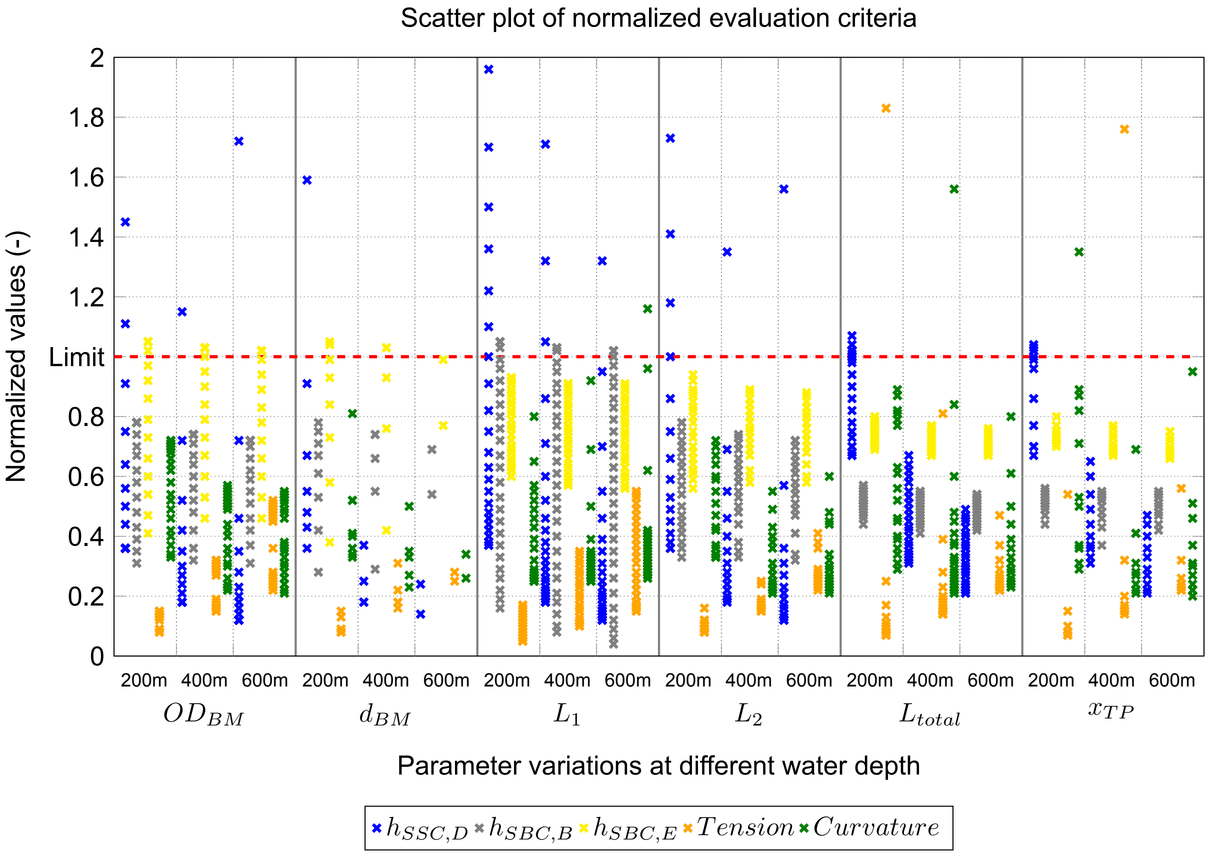

Figure 4.3: Scatter plot of normalized evaluation criteria of operational and physical constraints for all parameter variations across 200m, 400m, 600m

4.3. Parametric Variation at 200m Water Depth

The analysis at a water depth of 200m examines each parameter individually.

4.3.1. Effect of outer diameter buoyancy modules

The transition from a catenary to a lazy wave configuration results in changes in maximum curvature, noticeable up to a ratio of 3.55, where the curvature is predominantly governed by the TDP positioned between points B and D. In the catenary configuration, point F, is not located after point D as it would be in a lazy wave configuration. The simplification of indicating the TDP as point F helps in focusing on the curvature changes observed, see figure 4.4 for visual representation. Beyond a ratio of 3.7, section 2 has sufficient buoyancy force to achieve a total negative submerged weight. In this configuration, a "small wave" formation occurs, characterized by a slight horizontal excursion (x_{AC}). As the ratios increases, the points B and D ascend to a higher position, leading to a decrease in curvature at these points. For ratios between 4.16 and 4.78, the curvature transitions primarily to point F. Subsequently, at a ratio of 4.93, curvature peaks are further observed at point A. This shift coincides with the moment where the SSC at Point D is exceeded due to excessive buoyancy created by the BM. Despite a constant submerged weight and the fixed length of L_2, the curvature at point D remains less affected compared to other points.

As depicted in figure 4.5, tension is highest at point A across all scenarios. Variations in OD_{BM} influence the geometry and, consequently, the location and magnitude of operational constraints. An increase in seabed clearance at point B (decrease of h_{AB}), results in a minimal reduction in tension at point A, where tension even starts to increase at higher ratios. Moreover, the distance from point E to the seabed, $h_{SB,E}$, increases more than the decrease in h_{AB}. This leads to a steeper increase in tension at point E compared to the decrease at point A. This demonstrates a more pronounced effect of BM diameter changes on tension at point E, attributable to a concentrated increase in buoyancy force in section 2, affecting the distance x_{EF}.

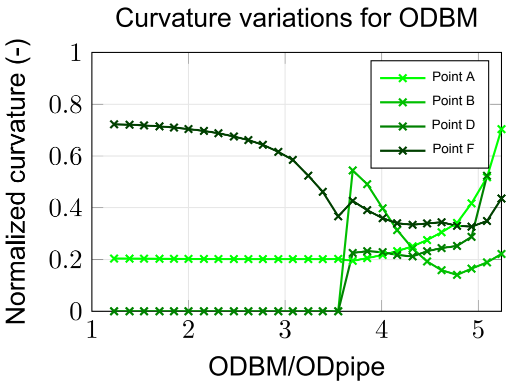

Figure 4.4: Maximum normalized curvature at points A, B, D, F for variations of OD_{BM}

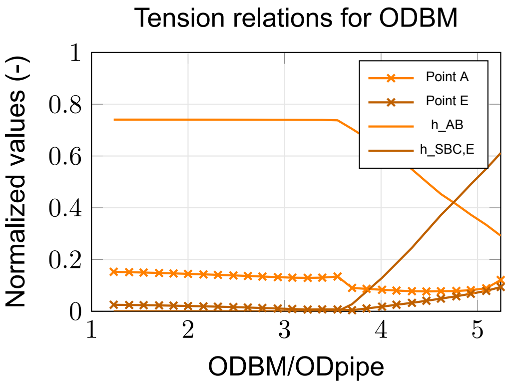

Figure 4.5: Effect tension at point A and E for variations of OD_{BM}

4.3.2. Effect of pitch between buoyancy modules

At ratios below 14, a catenary shape is observed, and from a ratio of 14 upwards, the submerged weight of section 2 becomes negative, resulting in an upward buoyancy force. The relationship between a larger ratio (higher number of buoyancy modules) and submerged weight increases exponentially, leading to ratios above 21 exceeding the sea surface constraint limit. This occurs at a submerged weight of -0.111 kN/m for section 2. Between ratios of 21 and 32, point D positions itself between this limit, while at ratios higher than 32, the BM begins to float at the surface.

This parameter variation, compared with the variation in the outer diameter of BM described in section 4.3.1, shows that changes in geometrical shape are identical, resulting in similar tension and curvature graphs. At points A, C, and E for tension, and points A, B, D, and F for curvature, the peaks occur at precisely the same locations. The static and dynamic contributions even show correlations. For scenarios that succeed within all evaluation criteria in both parameter variations, the peaks are of the same order of magnitude and exhibit identical trends as previously discussed. Therefore, the response behavior for these different parameters within the buoyancy section results in similar outcomes.

Thus, the behavior observed in d_{BM} variations mirrors that seen with changes in OD_{BM}. Section L_2, influenced by both OD_{BM} and d_{BM}, thus derives its geometrical shape from the buoyancy force generated. Both parameters exert their own influence on this buoyancy force. The submerged weight for the non-buoyant section of the pipe remains constant at 0.148 kN/m. Therefore, the net force of the buoyant section provides insight into the configuration where the the ratio of net force of buoyant section over net force of non-buoyant section is shown in figure 4.6. The variations in OD_{BM}, d_{BM}, L_2 exhibit consistent trends of the same order of magnitude, suggesting similar geometrical shape and clearance behavior. Additionally, it can be observed that the buoyant section can sustain a maximum net force of -1/4 of the net force of the non-buoyant section in order to remain within the SSC limit. Neglecting this limit allows for an increase in net force up to a maximum of -1/2 of the net force of the non-buoyant section for reaching the sea surface.

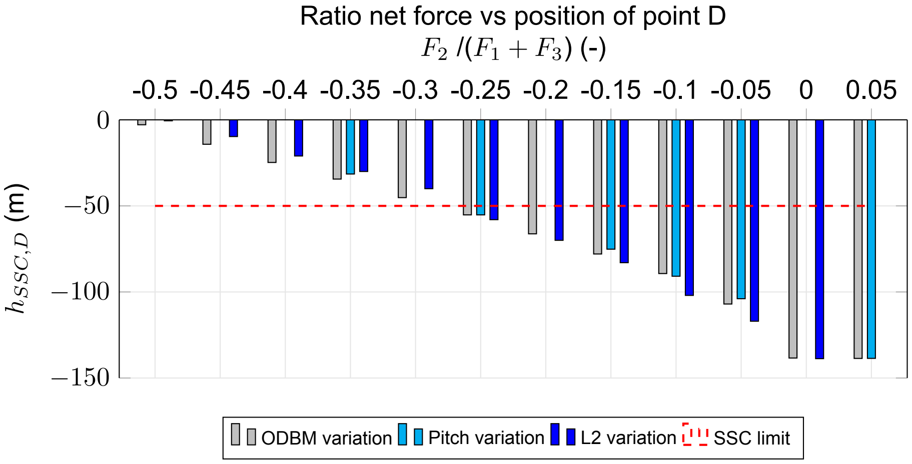

Figure 4.6: Ratio of net force from buoyant section over non-buoyant section with respect the vertical position of point D for variations of OD_{BM}, d_{BM} and L_2

4.3.3. Effect of first catenary section length

The primary contributor to this tension is the length of the pipe from which point it is suspended. Specifically, for variations in L_1, the vertical distance from h_{AB} is the most affected, impacting tension at point A. Figure 4.7 visualizes this relationship for this point, where the left y-axis displays the normalized tension and the right y-axis shows the absolute distances for the increase in L_1 and h_{AB}. The distance h_{AB} is equal to the total water depth minus the seabed clearance at point B. The increase in L_1 is not directly proportional to the increase in h_{AB} due to the decreasing angle at the HOP with longer L_1. This disparity results in a smaller relative increase in h_{AB} compared to the actual increase in L_1. This continues up to a ratio of 0.516, where eventually the distance of h_{AB} stops increasing due to the pipe lying on the ground. Consequently, the tension at point A increase with longer L_1, establishing a monotonic relationship between tension, the length of the pipe, and the vertical distance from point A to B. Tripling the length of L_1 doubles the distance of h_{AB}, while the tension at point also A nearly doubles.

A similar trend is observed at points C and E. Compared to point A, the effect of variations in distance and the corresponding tension is less pronounced at points C and E. At point E, while the distance $h_{SBC,E}$ decreases significantly, the tension only shows a minimal reduction. This reduction in tension is approximately equivalent to the increase observed at point C, even though the change in $h_{SBC,E}$ is more substantial than the change in h_{BC}. This suggests that the increase in horizontal distance affects the tension from the point its suspended from.

Furthermore, compression at the TDP occurs in scenarios with very small L_1 values, where operational constraints are already exceeded and the buoyant section reaches the sea surface.

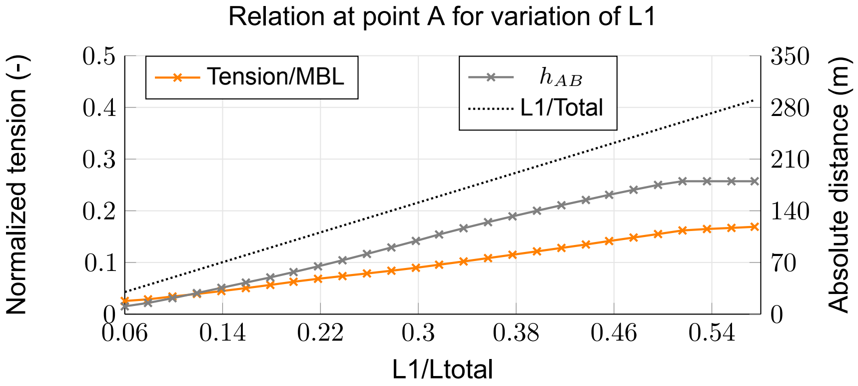

Figure 4.7: Relation at point A for distances and tension for variations of L_1

Figure 4.8 shows that maximum curvature decreases until a ratio of 0.3. Curvature peak positions vary across the tested ratios, with successful scenarios between ratios of 0.24 to 0.48. Below a ratio of 0.08, the highest curvature occurs at point A due to the elevated position of point SB (point B) and HB (point

D) when L_1 is short. From ratios of 0.1 to 0.28, the peak shifts to point F, decreasing as L_1 lengthens, which lowers the SB and HB further. This increases x_{EF}, leading to a smoother TDP which stabilizes at a normalized value of 0.1. Beyond a ratio of 0.3, the peak returns to point A. Additionally, the increase in L_1 increases x_{AC} and x_{CE}, promoting smoother bends and increasing the radius at points B and D. At a ratio of 0.5, the pipe contacts the seabed, causing a slight increase in curvature at point B.

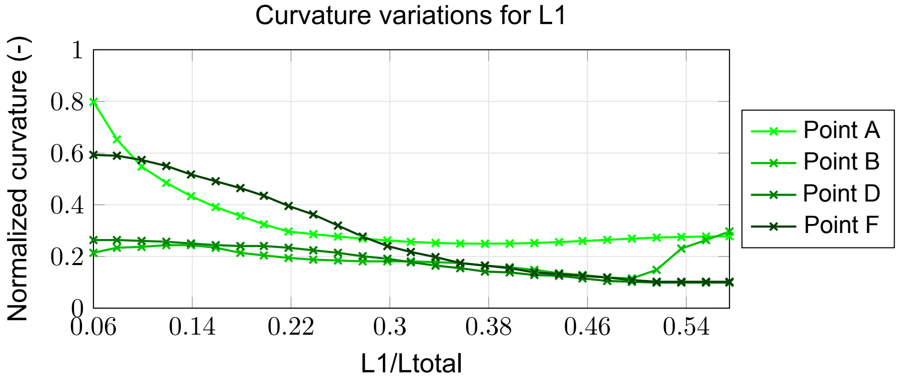

Figure 4.8: Maximum normalized curvature at points A, B, D, F for variations of L_1

4.3.4. Effect of buoyancy section length

Tension remains almost consistent across all ratios, following similar trends to those observed in variations of OD_{BM} and d_{BM}. Figure 4.9 shows the variations in tension. Starting from a ratio of 0.08, tension drops across all points as L_2 length increases, facilitating a lazy wave shape. Below this ratio, L_2 is too short to generate sufficient upward force (The buoyant section's submerged weight is -0.114 kN/m, whereas the non-buoyant section's is 0.148 kN/m). At a ratio of 0.08 (the lengths are 40m for L_2 and 464m for the non-buoyant section), resulting in total submerged weights of -4.6 kN and 69 kN, respectively. As L_2 increases, points B and D, leading to higher tension at point C which, at certain ratios, exceeds the tension at point E. These changes result in an increase of x_{AC}, altering the tensile forces.

This geometrical shape thus alters with concerning the horizontal distances x_{AC} and x_{CE}. This results in a consistent increase in both excursions, leading to similar radius variations and identical curvature behavior at points B and D. Figure 4.10 details the maximum curvature across all points, highlighting that below a ratio of 0.079, the catenary shape dominates, reducing curvature at points B and D with the peak occurring at point F where the pipe contacts the seabed. As L_2 increases, shifting to a lazy wave configuration, curvature peaks move to point B and D (the HB and SB), while the curvature at point F (the TDP) decreases. The increase in L_2 results in diminished curvature at these bends between ratios 0.198 and 0.298 due to extended horizontal distances X_{AC} and X_{CE}, with the most pronounced curvature found at point A above a ratio of 0.298. For ratio beyond 0.258, the SSC at point D is exceeded. The high position in combination with a large horizontal excursion of the bends, results in a non-optimal shape, leading to high curvature at point A.

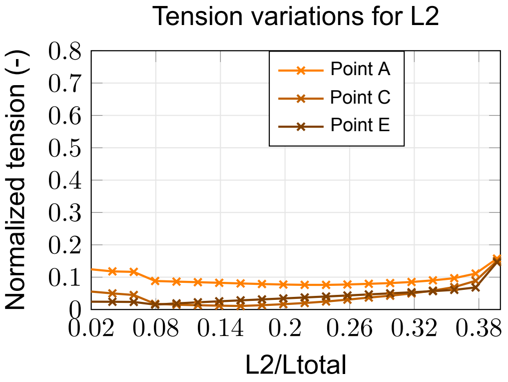

Figure 4.9: Maximum normalized tension at points A, C, and E for variations of L_2

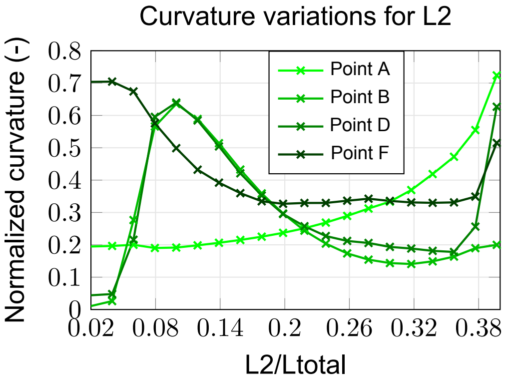

Figure 4.10: Maximum normalized curvature at points A, B, D, F for variations of L_2

4.3.5. Effect of total pipe length

For ratios above 3.08, the deformation at point F due to excessive slack results in missing data points and coiling of the pipe, (see appendix D.4 for visualizations of failed scenarios). This undesirable coiling causes compression from a ratios higher than 2.97 and necessitates a taut deployment of the pipe at the TDP to prevent unforeseen failures. Overall, a decrease in L_{total} tends to stretch the pipe, resulting in increased tension and curvature.

Tension remains relatively stable across all ratios of L_{total}, with the highest levels consistently observed at point A and lowest at point G, as shown in figure 4.11. For ratios higher than 2.97, compression occurs at point G, showing negative tension. Consequently, these ratios are not further observed but are still depicted in the figures. At shorter lengths, there is no direct correlation between the vertical distance h_{AB} and the tension, suggesting that high peaks in tension are not solely attributable to the pipe's weight. Instead, these peaks arise from a stretched scenario where the lazy wave configuration is not achieved, leading to exponential increases in tension. As L_{total} increases, the tension at point A converges to approximately 10% of its normalized value from ratios of 2.58 onward, while tension at point G diminishes to lower levels. Specifically, tension at G falls below 2% of its normalized value (5kN) at a ratio of 2.36 and below 0.4% (1kN) at a ratio of 2.63. This results in a minimum required L_{ST} of 0.25 and 0.4 times L_{total} to be below the threshold levels, respectively.

Curvature analysis focuses on points A and F, as depicted in figure 4.12. In scenarios with shorter L_{total}, curvature at points B and D results in diminished peaks, while in the lazy wave configuration, the maximum peaks stabilize at approximately 22% of their normalized value. In stretched scenarios, point A exhibits high curvature while point F shows low curvature. At a ratio of 2.74, the curvature equalizes between these points; for longer lengths, the curvature dynamics invert. This results in the curvature at point A to decrease and at point F to increase due to the pronounced effect of the wave configuration.

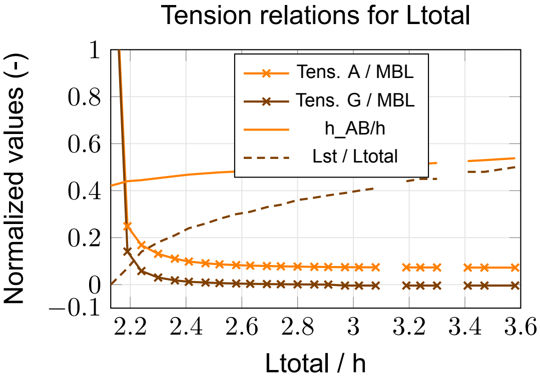

Figure 4.11: Relation and tension at points A and G for variations of L_{total}

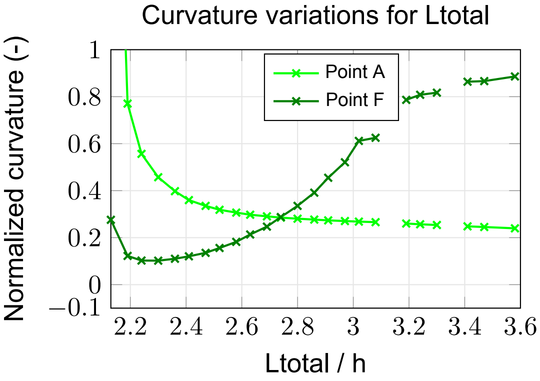

Figure 4.12: Maximum normalized curvature at points A and F for variations of L_{total}

The clearances to the seabed and sea surface are less affected by this variation compared to other parameters. This is because changes in L_{total} mainly influence the pipe on the seabed, as the clearances converge. Thus, increasing L_{total} primarily extends the static horizontal distance (L_{ST}) along the seabed without altering the overall geometrical shape. Figure 4.13 shows that L_3 increases linearly with L_{total}, while L_{ST}, at a ratio of 2.58, aligns with the rate of increase in L_3. Beyond this point, additional length causes more pipe to rest on the seabed, with minimal impact on the shape. However, for larger ratios, some variations in shape occur, driven by changes in x_{AF}. From a ratio of 2.97 upwards, the SSC at point D stabilizes, marking the limit of x_{AF}. At this point, the shape in the water column stabilizes, and looping begins at point F, linked to compression at G.

From an equilibrium ratio of 2.58, where L_{ST} is 139 m, the shape of the water column remains influenced. Beyond a ratio of 2.97, the shape stabilizes, and only L_{ST} increases, reaching a maximum of 208 m. These correspond to maximum normalized lengths of L_{ST} of 0.3 and 0.4 times L_{total}, respectively.

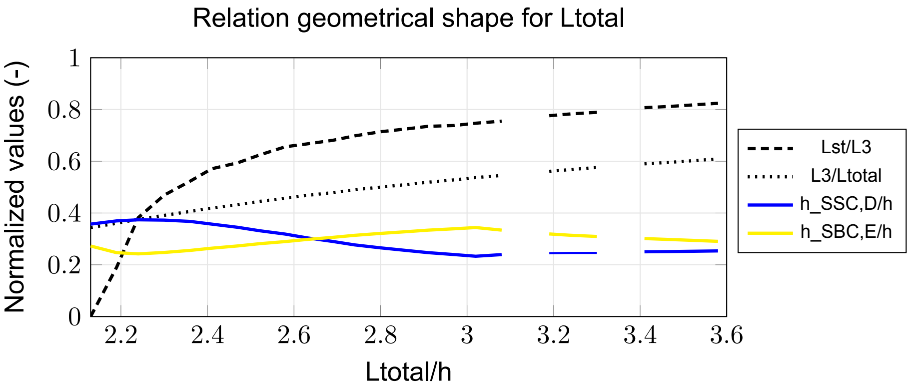

Figure 4.13: Relation geometrical shape of length and clearances for variations of L_{total}

4.3.6. Effect of horizontal termination point

Analysis of the x_{TP} variations reveals patterns mirroring those observed in the parameter variations of L_{total}. This behavior is demonstrated in figures 4.14 and 4.15, where the x-axis correlates the ratios of $\frac{L_{\text{total}}}{h}$ and $\frac{x_{\text{TP}}}{h}$. At a ratio of 2.4, the operational and physical criteria align for both parameters. The results show that the operational criteria further aligns closely with these equal step size of ratios from point 2.4, suggesting a direct correlation between with the geometric shape.

Moreover, as discussed in section 4.3.5, the maximum tension is observed at point A, with the maximum curvature transitioning from A to F beyond a ratio of 2.7. Similarly, for x_{TP}, this transition exhibits similar mirrored characteristics, occurring at a ratio of 2.1 for the curvature transition from F to A. Consequently, both maximum tension and curvature maintain comparable values with aligned increases or decreases in step size centered around a ratio of 2.4, as shown in figure 4.15. Furthermore, compression at point F is observed for ratios below 1.83.

However, discrepancies exist between in tension and curvature. In stretched scenarios (ratio 2.6 for x_{TP} and 2.2 for L_{total}), tension is approximately four times and curvature nearly two times higher in L_{total} scenarios compared to x_{TP}. Furthermore, in slacked scenarios converging issues arise for L_{total} while not for x_{TP} variations. This demonstrates that while the geometrical shapes in the water column exhibit similar trends, the maximum tension and curvature exhibit differences in stretched and slacked scenarios.

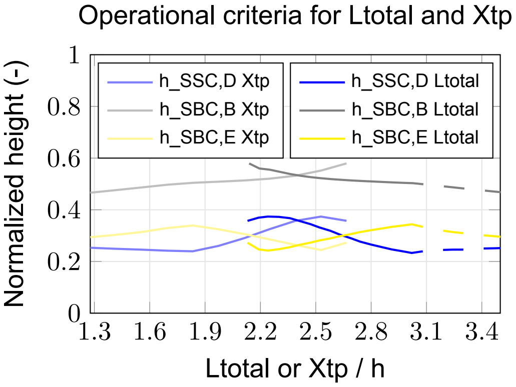

Figure 4.14: Comparison operational criteria on the variations of L_{total} and x_{tp}

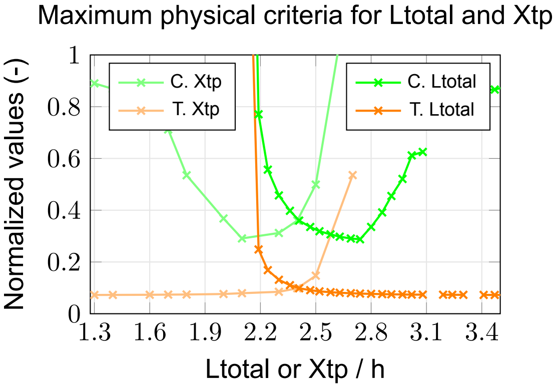

Figure 4.15: Comparison physical criteria on the variations of L_{total} and x_{tp} (C.= maximum curvature & T.= maximum tension)

4.3.7. Transition point by horizontal static length

The above mentioned difference in slacked or stretched scenarios, emerge when considering the absolute length (L_{AF}) and horizontal distance (x_{AF}) between the HOP (point A) and the TDP (point F), detailed by the following equations:

1. $$L_{AF} = L_{total} - L_{ST} \quad (4.1)$$
   $$where \quad L_{AF} = L_1 + L_2 + L_{3,\text{cat}}, \quad from \quad figure \; 3.22a$$

2. $$x_{AF} = x_{TP} - L_{ST} \quad (4.2)$$
   $$where \quad x_{AF} = x_{AC} + x_{CE} + x_{EF}, \quad from \quad figure \; 3.21$$

Figure 4.16 shows that the relationship between total length and horizontal distance does not consistently exhibit mirrored behavior. For stretched scenarios (ratios of 2.7 for x_{TP} and 2.2 for L_{total}), peaks in tension and curvature occur due to the minimal static horizontal distance. This distance is not present for L_{total}, explaining the higher tension and curvature observed. In slack conditions, non-convergence occurs for L_{total} due to the increase of L_{ST}, while x_{TP} converges to a maximum. Although the magnitude of changes in L_{ST} is greater when varying L_{total}, the tension and curvature behavior remains similar for scenarios that are neither stretched nor slacked.

To maintain tension at point G below 5 kN, a minimum L_{ST} length is required: at least 0.21 times L_{total} (with a minimum ratio of 2.36) and 0.35 times x_{TP} (with a maximum ratio of 2.53). From a financial standpoint, minimizing pipe length is more cost-effective, especially when limiting the length resting on the seabed. Therefore, it is preferable to set L_{total} at its minimum of 2.36. Beyond this ratio, adjusting x_{TP} to smaller ratios reduces tension and curvature while maintaining the minimum required length L_{ST}.

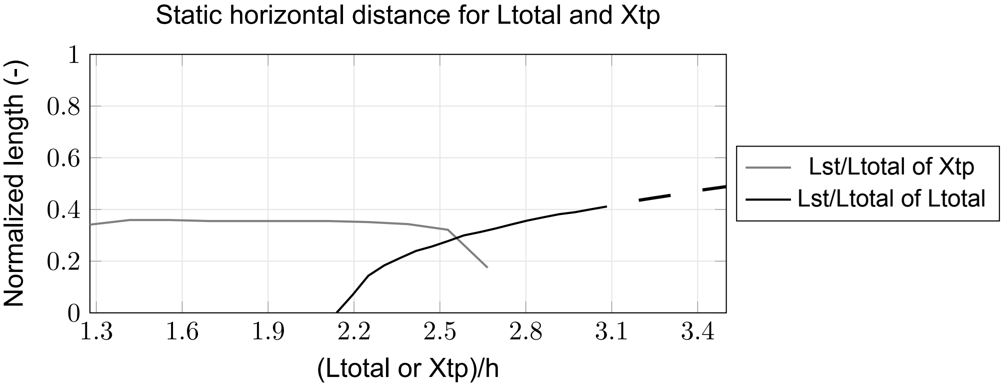

Figure 4.16: Comparison of static horizontal length on the variations of L_{total} and x_{tp}

4.4. Parametric Variation at 400m and 600m water depth

This section examines the impact of parameters at different water depths.

4.4.1. Effect on OD_{BM}

The evaluation criteria show consistent behavior across varying depths, with minimal impact on the SBC and the greatest difference at point D for the SSC. As depth increases, a wider range of successful scenarios allows OD_{BM} to increase before exceeding constraints. OD_{BM} is constrained by the SBC at point E and the SSC at point D, see figure 4.17 for the dynamic analysis. The solid line shows the limit based on the criteria, while the dashed line represents seabed or sea surface. These limits vary with depth: at 200m, OD_{BM} ranges from 3.85 to 4.47; at 400m, from 3.7 to 4.78; and at 600m, from 3.7 to 4.93. The acceptance range expands by 75% at 400m and doubles at 600m. In static analysis, the 4.58 ratio at 200m rises slightly to 4.62.

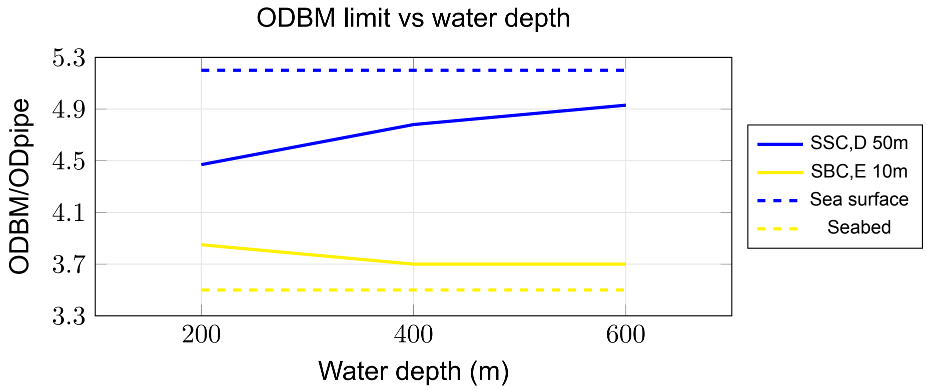

Figure 4.17: OD_{BM} limit on the clearances at points D and E for water depths of 200m, 400m, and 600m

The curvature at point B and F does not increase with depth. A smoother TDP area is observed at point F with increasing depth in lazy wave configurations. At 200 m, the maximum curvature shifts from point B to F and then to A, while at greater depths, the peak transitions directly from B to A. Point A is minimally affected by depth changes, while points B and F experience larger variations. As depth increases, curvature at points B and F decreases, shifting the maximum curvature to point A at a lower ratio. This reduction in curvature is due to the increased x_{AC} and x_{EF}, leading to smoother bends. Figure 4.18 compares points A, B, and F. Point D is excluded, as its curvature is lower than point B in all cases.

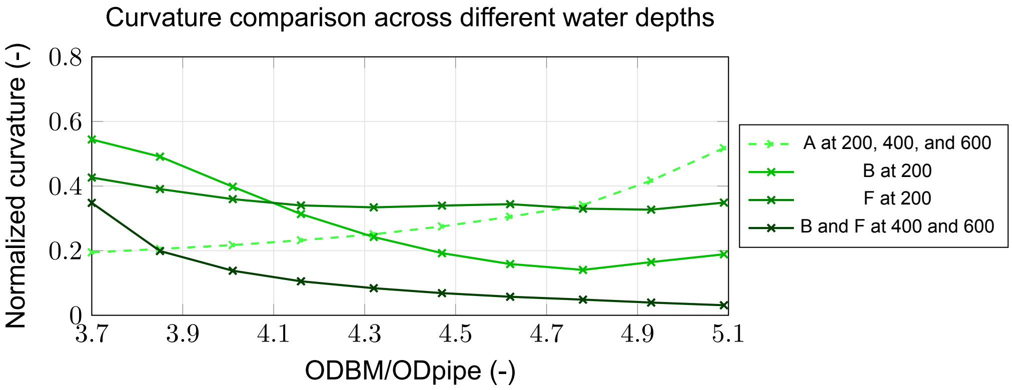

Figure 4.18: Curvature at points A, B, and F at 200m, 400m and 600m water depth

4.4.2. Effect on d_{BM} and L_2

For d_{BM}, the evaluation criteria across different water depths show variations in scenario convergence. With a fixed section length L_2 (126 m at 200 m, 266 m at 400 m, and 406 m at 600 m), the pitch changes for each depth. At 200 m, the response remained similar to changes in BM diameter. The buoyancy force from section 2 impacts the lazy wave configuration, while sections 1 and 3 maintain a constant submerged weight of 0.148 kN/m. When the buoyant section's submerged weight exceeds zero, no net buoyancy force is generated, resulting in a catenary configuration. A larger buoyancy force causes the lazy wave to rise vertically, potentially interfering with the sea surface, leading to non-convergence as BM reaches the surface.

When evaluating L_2 across water depths of 200m, 400m, and 600m, the primary difference arises at the SSC at point D, since the constraint at -50 m remains fixed regardless of water depth. Across all water depths, a minimum of 0.08 of the total length (L_{total}) is necessary for the pipe to form a lazy wave configuration. The limit of L_2 across varying depths is shown in figure 4.19, where ratios of the maximum buoyancy force can reach -1/2 of the non-buoyant section's net force at any depth before surfacing. The SSC becomes limiting at ratios of -0.25 for 200m, and -0.4 for 400m and 600m. This results in maximum L_2 ratios with respect to L_{total} of 0.26, 0.32, and 0.34 for 200m, 400m, and 600m, respectively, with point D reaching the surface at a ratio of 0.4. Figure D.13 in appendix D.3 shows the similar behavior of clearances resulting from d_{BM} variations.

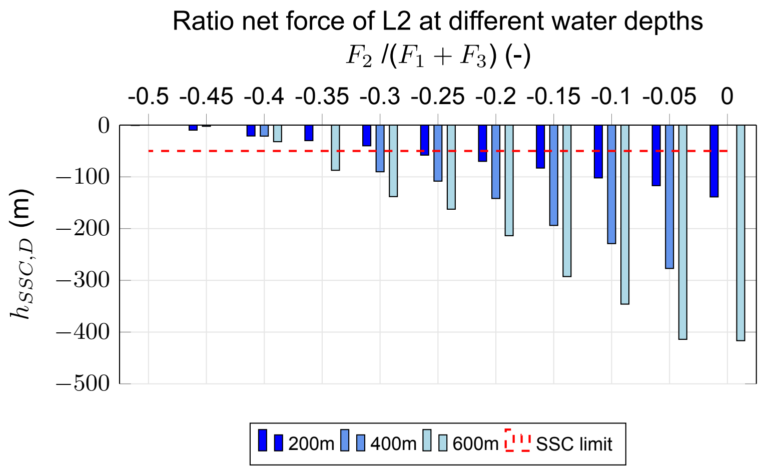

Figure 4.19: Ratio of net force from buoyant section over non-buoyant section for variations of L_2 with respect to sea surface clearance (h_{SSC}) at 200m, 400m, and 600m water depth

Focusing on the ratio of net force in buoyant section to the non-buoyant section, within the range of -0.5 to 0 (restricted to -0.25 for 200m and -0.4 for 400m due SSC), figure 4.20 shows the relationship between the number of BM units (constant across depths) and pitch (scaled with water depth). As depth increases, more BM units are needed to stay within the, following an exponential trend that reduces the weight of the buoyant section. Successful pitch scenarios occur between 6m to 9m at 200m, 6m to 8m at 400m, and 6m tom 10 at 600m. The required BM units range from 14 to 21 at 200m, 32 to 42 at 400m, and 42 to 63 at 600m.

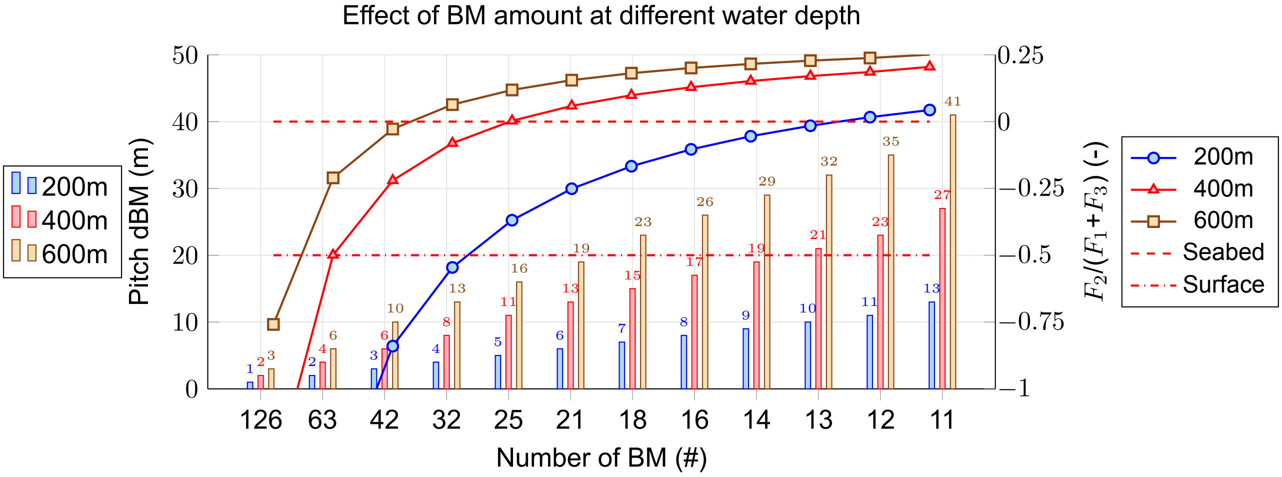

Figure 4.20: Effect BM amount on pitch and ratio net force buoyant and non-buoyant section at 200m, 400m, and 600m water depth

Figure 4.21 illustrates the curvature at points A, B, and F for L_2 across two ratios, which can also be observed for d_{BM}. Approximately a decrease of 40% from 200m to 400m and 50% from 200m to 600m is observed across all points, primarily driven by points B, D and F. The maximum curvature at point A remains consistent across all depths, with only small deviations across varying water depths. Smaller wave formations lead to higher curvature at point B and F, while larger wave formations result in higher curvature at point A. The horizontal distances X_{AC} and X_{CE} impact the curvature at points B and D similarly in all water depths. In shallower waters, larger curvature is observed at all points due to scaling effects in deeper waters, making curvature more vulnerable in shallower water. This is particularly evident at point F, where the largest absolute values occur (ranging between ratios of 0.1 and 0.3), while point B is more sensitive to changes than point F.

Furthermore, the tension shows similar behavior across all water depths, with a 50% increase in tension at point A from 200m to 400m depth, and a 70% increase from 200m to 600m depth.

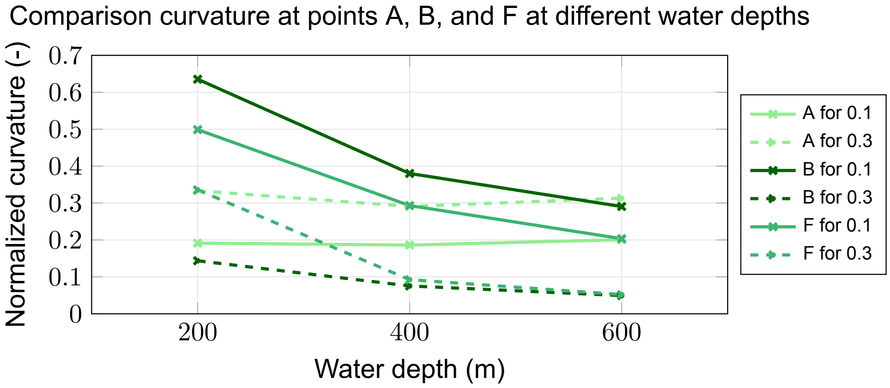

Figure 4.21: Comparison of normalized curvature at points A, B, and F for ratios 0.1 and 0.3 for variations of L_2 at 200m, 400m, and 600m water depth

4.4.3. Effect on L_1

The evaluation of L_1 across various water depths reveals a consistent pattern, where longer lengths are constrained by the SBC at point B, while shorter lengths are limited by the SSC at point D. However, deeper depths slightly expand these limits. As depicted in figure 4.22, the operational range for clearances at 200m is between 0.24 and 0.49, at 400m between 0.145 and 0.5, and at 600m between 0.115 and 0.515 of the total length. Notably, L_1 can increase by approximately 40% at 400m and 60% at 600m depth. In the static analysis, the minimum increases to a ratio of 0.139.

At point G, maximum allowable tension is required when the pipe connected to the TP, as shown in figure 4.22. This tension depends on L_{ST}, which inversely relates to L_1. For different depths, the normalized length of L_{ST} relative to L_{total} decreases uniformly, though tension at point G varies. The 5 kN limit [82] aligns with seabed clearance, while the 10 kN limit is reached with seabed interference. The 1 kN limit restricts L_1 more compared to the SBC at point B. At 400m and 600m, larger limits are reached earlier as all limits converge to similar L_1 lengths, resulting in smaller variations between different tension criteria in deeper waters. At 200 m, lower limits (e.g., 1 kN) affect L_1 more, making shallower water critical to smaller tensions. For 1 kN, L_1 increases by 12% at 400m and 14% at 600m compared to 200m, while the 5 kN limit reduces L_1 by 10% at greater depths. The minimum L_{ST} is 0.29 times L_{total} for 1 kN, 0.15 for 5 kN, and 0.1 for 10 kN. See figure D.12 in appendix E for the comparison of L_{total} and L_{ST}.

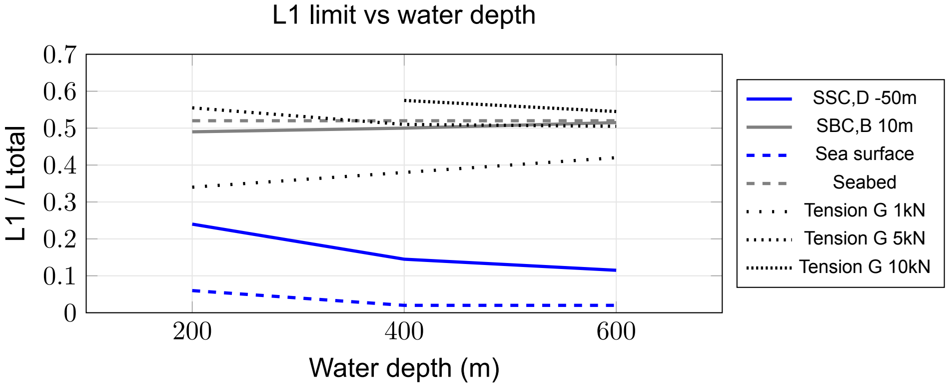

Figure 4.22: L_1 limit on the clearances at points B and D and tension at G at 200m, 400m, and 600m water depth

As noted in section 4.4.1, the curvature at point A remains relatively constant across all water depths, while the curvature at points B, D, and F decreases. This behavior is reflected in the this parameter across water depths, where the curvature at A shows minimal variation, but point F exhibits a consistent decrease in curvature across all scenarios. This indicates that point F is more sensitive to changes in water depth, where a 60% reduction is observed from 200m to 400m, and a 70% reduction from 200m to 600m. For detailed curvature comparisons, see figure D.13 in appendix E.

The tension at point A is primarily influenced by the free-hanging length, which increases with water depth. Although tension does not scale perfectly linearly with depth, there is a strong correlation. By extrapolating normalized tension values at 200 m, 400 m, and 600 m, an estimate of the tension at point A can be derived, as shown in figure 4.23. Different rates of tension increase (Inc. rate) with depth reveal varying growth patterns. The normalized tension values are 0.14, 0.3, and 0.47 at 200 m, 400 m, and 600 m, respectively, for a scenario without seabed or sea surface interference. Extrapolation suggests that the MBL could be exceeded between 1000 and 1400 m, depending on the rate of increase. The compounded growth estimate provides the most accurate prediction by accounting for relative increases. However, other constraints, such as the collapse limit at 510 m, impose stricter depth limitations than the MBL.

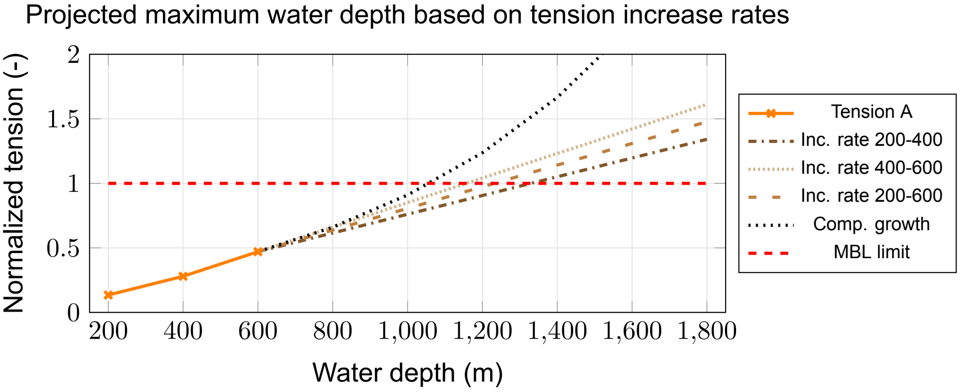

Figure 4.23: Estimated maximum water depth based on tension increase rates at point A

4.4.4. Effect on L_{total} and x_{TP}

For L_{total}, the SSC of -50 m at point D in 200m water depth is the limiting factor, while for 400m and 600m, geometrical shape is unaffected at lower ratios but influenced by variations in x_{AE} at higher ratios. Maximum tension consistently occurs at point A, followed by points C, E, and G. As depth increases, tension rises at points A, C, and E, but decreases at G. On average, tension at point A doubles from 200m to 400m, and triples by 600m. In contrast, tension at point G decreases by 10% from 200m to 400m, and by 15% at 600 m.

For curvature, the largest differences occur between points A and F. Transitions between these points shift to larger ratios as water depth increases. Points B and D exhibit similar curvature to F. In stretched configurations, point A experiences larger curvature, while in slacked scenarios, point F is more affected. Deeper waters impact point A in stretched cases more than F due to small wave formations in the pipe. Curvature at point F decreases with depth in slacked scenarios, driven by the increase in x_{TP}. Maximum curvature transitions from point A to F at a ratio of 2.74 for 200m, 3.13 for 400m, and 3.30 for 600m (see figure D.14 in appendix E).

The mirrored behavior of L_{total} and x_{TP} across water depths indicates that operational and physical constraints yield identical values across the x-axis. At a ratio of 2.4, both $\frac{L_{total}}{h}$ and $\frac{x_{TP}}{h}$ are perfectly aligned. The outcomes are similar for equal step sizes of L_{total} upwards and X_{TP} downwards. Figures 4.24a and 4.24b show the minimum and maximum required L_{total} and x_{TP}. These variations are primarily limited by tension at point G, rather than MBL or MBR. The MBR dominates as it is reached earlier than the MBL. Even when the pipe does not touch the seabed, additional axial load due to stretching does not exceed these limits. The maximum of L_{total} and minimum of x_{TP} are based on looping at the TDP, but the tension threshold at G remains the limiting factor, not maximum curvature or tension at point A. In shallower waters, smaller threshold values are critical, while in deeper waters, values converge to similar ratios, especially in x_{TP}.

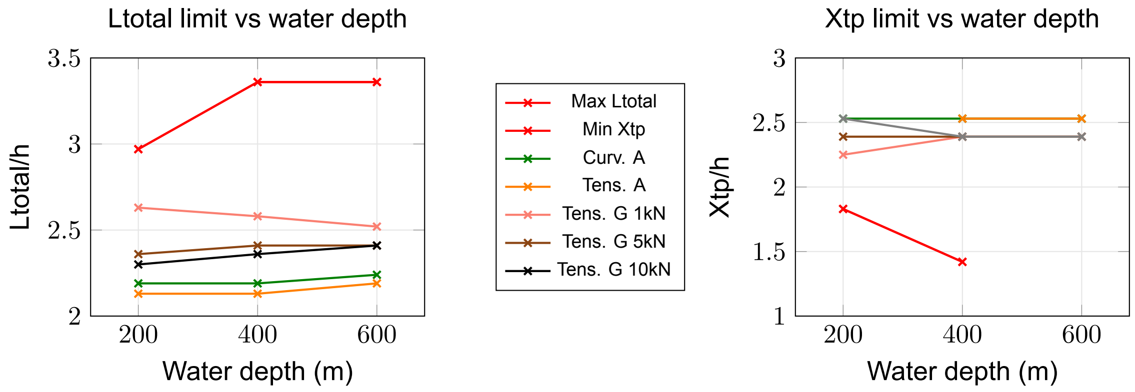

(a) L_{total} limit on physical criteria

(b) x_{TP} limit on physical criteria

Figure 4.24: L_{total} and x_{TP} limit based on physical criteria at 200, 400, and 600m water depth

4.4.5. Effect on L_{ST}

For the variations of L_1, L_{total}, and x_{TP}, tension at point G imposes limitations on the minimal required lengths and distances. This tension correlates with the static length of pipe lying on the seabed, L_{ST}. A longer pipe requires a larger frictional surface, leading to more dissipative energy.

The visualization of the minimum required L_{ST} for the three parameter variations is shown in figure 4.25. A minimum tension at point G is required, and different water depths result in various minimum lengths of L_{ST}. As water depth increases, threshold values converge toward a minimum. For X_{TP}, the largest L_{ST} is required across all depths, followed by L_{total} and then L_1. Moreover, the difference in tension thresholds is smallest for X_{TP}, followed by L_{total} and L_1 as well. Consequently, variations in X_{TP} have the greatest influence on the tension at G, requiring a distinct minimal L_{ST} of 0.343 times L_{total} for water depths of 200 m, 400 m, and 600 m.

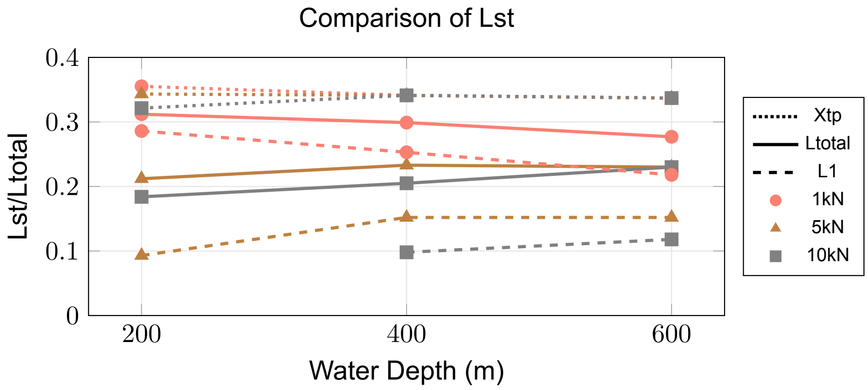

Figure 4.25: Comparison of L_{ST} for variations of L_{total}, X_{tp}, and L_1 at 200, 400m, and 600m water depth

4.5. Sensitivity Analysis

This results of the sensitivity analysis are presented, which focuses on the effects of a 10% increase or decrease in parameters on tension and curvature. At water depths of 200m, 400m, and 600m, the base values are derived for normalized physical constraints at specific points. These results from the dynamic analysis are used, where as the static analysis shows an overall lower averaged tension (12%) and a reduced curvature (24%). Visualizations of the base value outputs and a comparison between dynamic and static outputs from these values can be found in appendix E.1.

Figure 4.26 displays the allowable parameter ranges for water depths of 200m, 400m, and 600m. The base value corresponds to the base scenario, with the range being limited by minimum and maximum percentage changes. These limits are constrained by boundary conditions, indicating the maximum allowable increase or decrease to which the base value can fluctuate before meeting a boundary condition. The first four parameters, outer diameter of BM (OD_{BM}), pitch (d_{BM}), length of the first section (L_1), and length of the buoyancy section (L_2), are governed by clearances at thes seabed and sea surface, whereas the last two parameters, total length (L_{total}) and termination point (x_{tP}), are influenced by compression and tension at point G. From the figure, it is evident that the outer diameter of the buoyancy module has the smallest range, followed by the pitch and total length. The lengths of the first and second sections show the largest ranges. Moreover, an increase in water depth allows for larger ranges.

The allowable ranges for the static analysis show a 4% decrease in the maximum and minimum values at L_1 across all water depths due to SBC, and at 200m, a 4% increase in the outer diameter and total length due to SSC. This results in minor differences between static and dynamic analysis, leading to the decision to proceed with the results of the dynamic analysis. Detailed data for the minimum and maximum ratios for each parameter for both static and dynamic analyses are provided in appendix E.2.

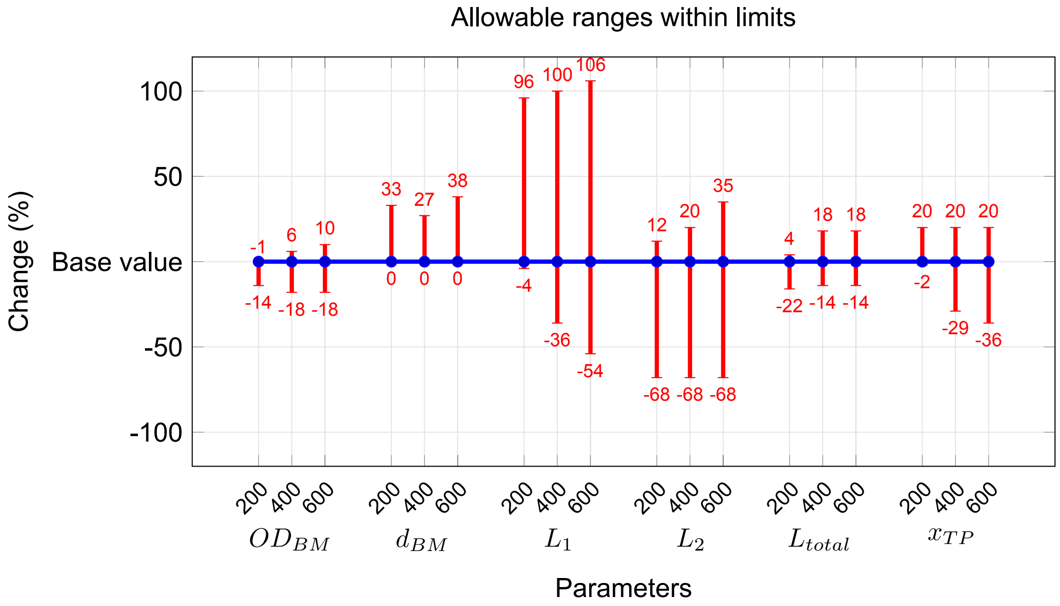

Figure 4.26: Plot showing allowable increase or decrease for parameters from its base value at 200m, 400m, and 600m water depth in dynamic analysis

The sensitivity analysis demonstrates that parameter variations yield similar, yet slightly more pronounced, rates of increase or decrease in dynamic when compared to static analyses. Consequently, only the dynamic sensitivity results at 200m are presented in figure 4.27. The rates of parameter increase and decrease do not translate to comparable output responses in terms of tension and curvature. Therefore, figure 4.27a details the effects of a 10% decrease, while figure 4.27b depicts the effects of a 10% increase. It is important to note that the percentages in this heatmap are derived from the linearization of test scenarios, which involved combinations of a 10% increase or decrease in parameter variations, as explained in section 3.6.5. Parameters OD_{BM}, L_1, L_2, and x_{tP} show consistent relationships with tension but display inverse relationships with curvature. In contrast, parameters d_{BM} and L_{total} display the opposite behavior, showing a similar relation to curvature and an inverse relation to tension. Results of the heat maps for 400m and 600m depths, along with data from the static analysis, are available in appendix E.3.

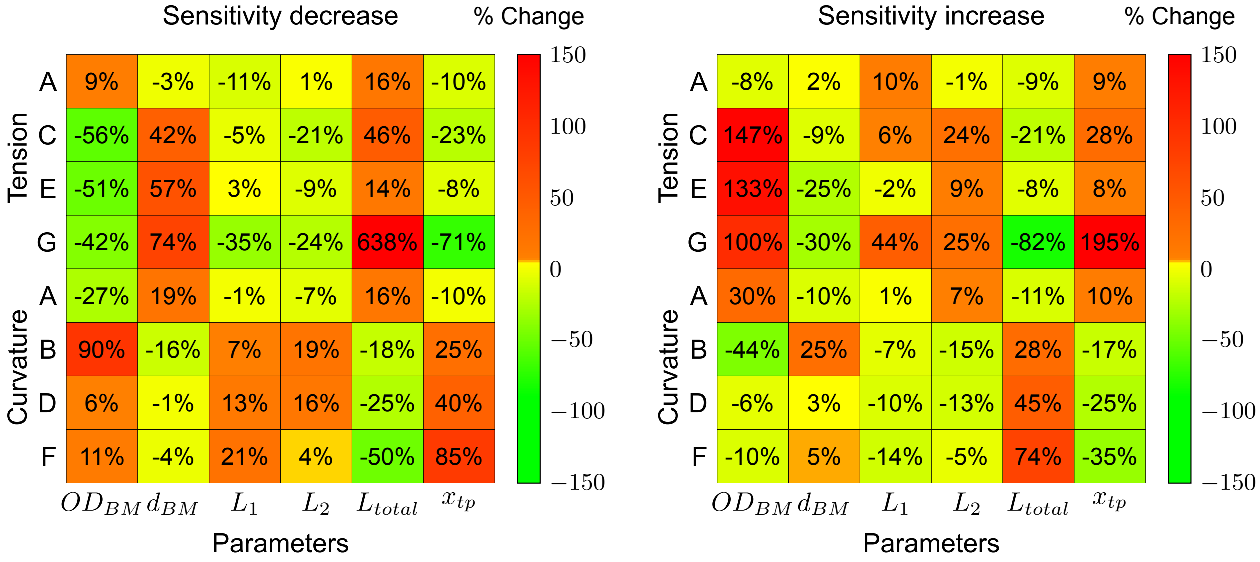

Sensitivity decrease

		OD_{BM}	d_{BM}	L_1	L_2	L_{total}	x_{tp}
Tension	A	9%	-3%	-11%	1%	16%	-10%
	C	-56%	42%	-5%	-21%	46%	-23%
	E	-51%	57%	3%	-9%	14%	-8%
	G	-42%	74%	-35%	-24%	638%	-71%
Curvature	A	-27%	19%	-1%	-7%	16%	-10%
	B	90%	-16%	7%	19%	-18%	25%
	D	6%	-1%	13%	16%	-25%	40%
	F	11%	-4%	21%	4%	-50%	85%

(a) Effect on tension and curvature for a 10% decrease of parameter

Sensitivity increase

		OD_{BM}	d_{BM}	L_1	L_2	L_{total}	x_{tp}
Tension	A	-8%	2%	10%	-1%	-9%	9%
	C	147%	-9%	6%	24%	-21%	28%
	E	133%	-25%	-2%	9%	-8%	8%
	G	100%	-30%	44%	25%	-82%	195%
Curvature	A	30%	-10%	1%	7%	-11%	10%
	B	-44%	25%	-7%	-15%	28%	-17%
	D	-6%	3%	-10%	-13%	45%	-25%
	F	-10%	5%	-14%	-5%	74%	-35%

(b) Effect on tension and curvature for a 10% increase of parameter

Figure 4.27: Comparison of heat maps for parameter sensitivity on tension and curvature at 200m depth in dynamic analysis

Based on the combination of the sensitivity heat map and the allowable parameter ranges, it is possible to compare different parameters. Unlike direct parameter comparisons, this focuses on the locations of tension at points A and C, and curvature at points B and F, as illustrated in figures 4.28 and 4.29 respectively. Tension at point E is not considered significant since the sensitivity at point C is more pronounced. As a result, tension at point E follows a similar sensitivity pattern to point C but at lower rates. Tension at point G is also disregarded as it is most sensitive to changes in L_{total} followed by x_{TP}, as identified in the parametric study. For curvature, parameters OD_{BM}, d_{BM}, L_2, and L_{total} are compared at points A and B, with mirrored rates at these locations. However, point A shows lower rates, making point B more dominant with larger effects. Furthermore, L_1, L_{total}, and x_{TP} are compared to changes in curvature at points D and F, with point F exhibiting higher sensitivity rates compared to point D, thereby disregarding the impact at point D. Changes within the buoyancy section have the least effect on the curvature at these point D and F.

For tension, the parameter most sensitive at point A is L_1, followed by L_{total} and x_{TP}. At point C, L_{total} is most sensitive, although the heatmap showed the largest rate for OD_{BM} and d_{BM}; however, due to the allowable range, these rates are not considered significant. This is similar for the tension at point E, as discussed above. Tension at point G is also most sensitive to L_{total} followed by x_{TP}. This indicates that tension across the length of the pipe is primarily influenced by changes in L_{total}, followed by x_{TP}, with point A being particularly sensitive to L_1. However, across the rest of the pipe, tension is least sensitive to L_1. Changes within the buoyancy section for OD_{BM}, d_{BM}, and L_2 are less sensitive to changes in tension compared to L_{total} and x_{TP}, with OD_{BM} being more sensitive than d_{BM} and L_2 across the entire length of the pipe.

For curvature, at point B the most sensitive parameters are in a similar order within the buoyancy section as OD_{BM}, d_{BM}, and L_2 followed by L_{total} and x_{TP}, following a similar trend as in point A with similar but lower rates. For curvature at points D and F, the buoyancy section is least sensitive to parameter changes, with L_{total} being more sensitive than x_{TP} followed by L_1. Notably, the buoyancy section is more sensitive to curvature at points A and B, while it is least sensitive at points D and F.

Combining this data reveals that across tension and curvature, several observations can be concluded. For changes within the buoyancy section, the order of sensitivity is always OD_{BM}, d_{BM}, followed by L_2 and L_{total} always shows higher sensitivity than x_{TP}. Specifically regarding tension, L_{total} exhibits the highest sensitivity along the entire length of the pipe, followed by x_{TP} and the buoyancy section parameters. Notably, L_1 shows the greatest sensitivity at point A, yet it is the least sensitive parameter overall. Specifically for curvature, points A and B are most sensitive to the buoyancy section, followed by L_{total}, x_{TP}, and L_1, while for points D and F, the latter three are more sensitive than the buoyancy section.

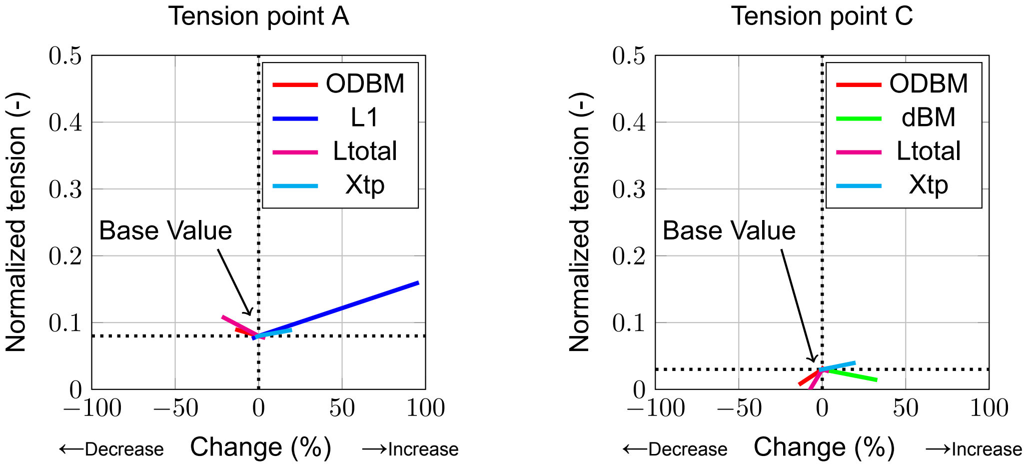

(a) Tension Point A

(b) Tension Point C

Figure 4.28: Comparison sensitivity for tension at points A and C at 200m depth

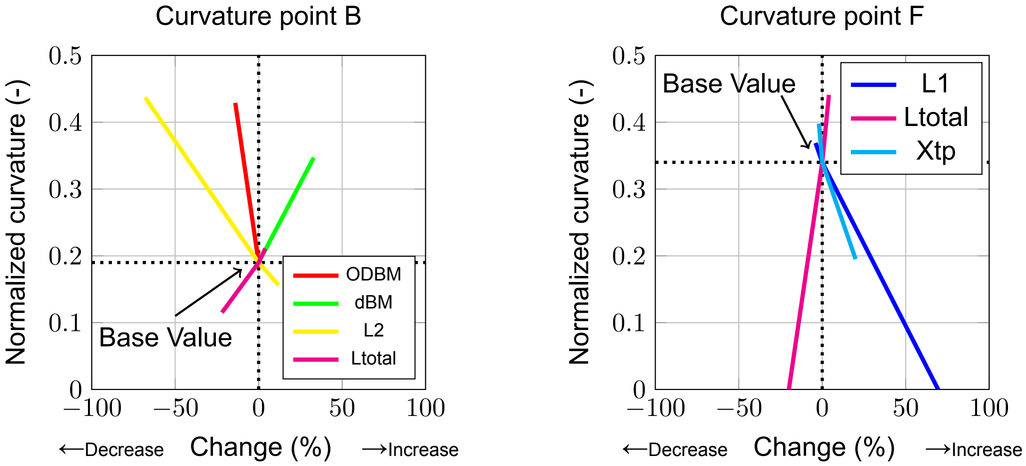

(a) Curvature Point B

(b) Curvature Point F

Figure 4.29: Comparison sensitivity of curvature at points B and F at 200m depth

At depths of 400m and 600m, different trends in sensitivity are observed compared to 200m. Since the sensitivity rates at 400m and 600m are similar, the focus of visualizations is provided for 400m. Deeper water results in decreased sensitivity in tension and increased sensitivity in curvature. Tension at points A and C are shown in figure 4.30, and curvature at points D and F in figure 4.31. For tension, point A is visualized due to differences at 200m, and point C is chosen over point E as it displays similar sensitivity but at higher rates. Point G exhibits similar tension sensitivity across all water depths. For curvature, points A, B, and F show similar sensitivity across all parameters. Only point F is highlighted due to its significantly higher rates than at A and B. Furthermore, point D is shows differences with repect to other points.

For tension, the most sensitive parameter at point A is L_1, followed by OD_{BM}, L_{total}, and x_{TP}. At points C and E, the buoyancy section shows the highest sensitivity in the order of OD_{BM}, d_{BM}, and L_2, followed by L_{total} and x_{TP}. In deeper waters, the buoyancy section is more responsive to changes compared to L_{total} and x_{TP}, which can be attributed to the longer free hanging length.

For curvature at point F (and thus also at points A and B), the most sensitive parameter is OD_{BM}, followed by L_{total} and x_{TP}. d_{BM} comes next, followed by L_2 and L_1. Compared to 200m, OD_{BM} becomes more sensitive and L_1 less sensitive. At point D, similar trends are observed as at 200m, with the buoyancy section affecting curvature at this location the least, yet L_2 is more sensitive than the rest of the buoyancy section parameters.

Combining this data reveals several observations across tension and curvature. The buoyancy section parameters are not always grouped in order of sensitivity, while L_{total} consistently shows higher sensitivity than x_{TP}. Specifically for tension, OD_{BM} exhibits the highest sensitivity along the entire length of the pipe, followed by L_1 at point A and the buoyancy section parameters at points C and E. Similar trends are observed at point G as at 200m. Specifically for curvature, points A, B, and F are most sensitive to OD_{BM}, followed by L_{total}, x_{TP}, and the buoyancy section, while at point D, the buoyancy section parameters are least sensitive.

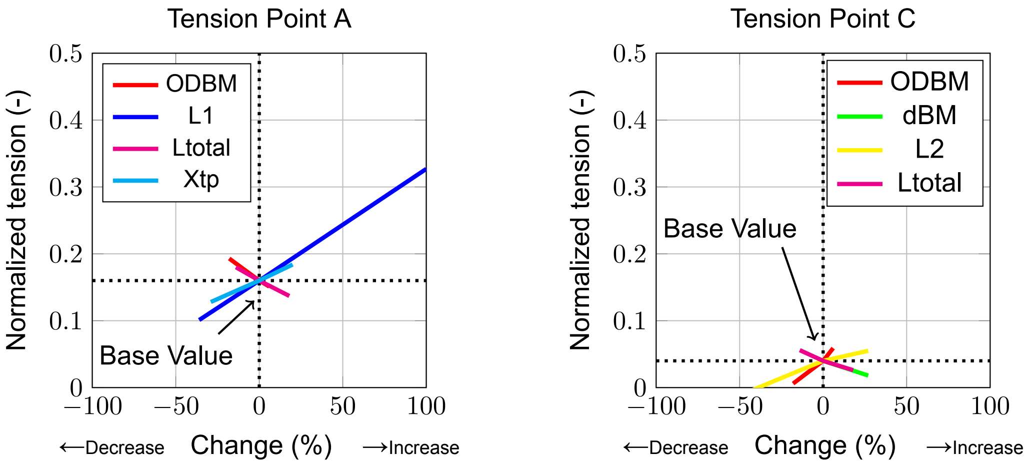

(a) Tension Point A

(b) Tension Point C

Figure 4.30: Comparison sensitivity for tension at points A and C at 400m depth

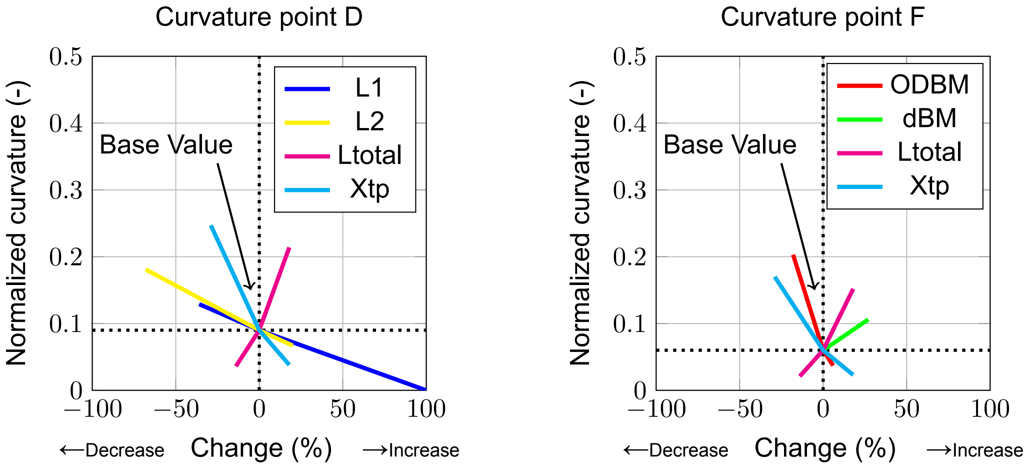

(a) Curvature Point D

(b) Curvature Point F

Figure 4.31: Comparison sensitivity of curvature at points D and F at 400m depth

The sensitivity rankings from most sensitive to least sensitive parameters are summarized as follows:

At 200m depth:

- For tension across the full length:

$$L_{\text{total}} > x_{\text{TP}} > OD_{\text{BM}} > d_{\text{BM}} > L_2 > L_1,$$

while at point A the most sensitive is L_1.

- For curvature at points A and B:

$$OD_{\text{BM}} > d_{\text{BM}} > L_2 > L_{\text{total}} > x_{\text{TP}} > L_1,$$

while at point D and F all the buoyancy section parameters are least sensitive.

At 400m and 600m depths:

- For tension at points C and E:

  $$OD_{\text{BM}} > d_{\text{BM}} > L_2 > L_{\text{total}} > x_{\text{TP}} > L_1,$$

  while at points A L_1 is the most sensitive, and at point G shows similar sensitivity as at 200m.

- For curvature at points A, B, and F:

  $$OD_{\text{BM}} > L_{\text{total}} > x_{\text{TP}} > d_{\text{BM}} > L_2 > L_1,$$

  while at point D all the buoyancy parameters are least sensitive.

5

Discussion and Limitations

This chapter presents the findings from the parametric study, with a detailed discussion in section 5.1 and the research limitations outlined in section 5.2.

5.1. Discussion

While the results presented in this research provide valuable insights, they must be interpreted with caution. The base case of the parametric study is tailored to specific end-use conditions, and the conclusions drawn here may not be directly transferable to other scenarios.

This research adopted the configurations based on recommendations from an optimization of DPC configurations. The MBL of a DPC is about 5 times smaller and the MBR is about 1.5 larger than for flexible pipes. This results in an excessive amount of buoyancy, effectively leading to an overly conservative evaluation of tension and curvature. The breaking load for DPCs is significantly lower than for pipes, which leads to positioning the wave shape in the middle of the water column to balance and minimize tension between the HOP and the end of the buoyant section. A lower wave shape, particularly in deep water scenarios (yet not investigated), would suffice, as the pipe's breaking load at the HOP is not exceeded when 1000 meters of pipe is suspended from this point. This smaller wave shape located in the proximity of the seabed would decouple the floater from the TDP, though curvature already converges to minimum value for an increase in water depth at the TDP. In shallower waters, looping could occur at the TDP, making a small lazy wave configuration preferable to minimize this.

The primary focus of this research is on only one specification for the flexible pipe. This sourced from the in-house software provided by the pipe manufacturer. This pipe has not been tested under real-world conditions, so the design is based solely on the numerical software's recommendations. The hydrogen electrolyzer used as the design input, while other types of electrolyzers may require different design parameters for pressure and temperature. Higher operating temperatures or pressures, for example, would necessitate thicker pipe walls or reinforced layers, increasing the mass and stiffness reducing its flexibility. This, in turn, increases the surface area, affecting hydrodynamic loading and response, and requiring additional buoyancy from the buoyant section to maintain the same geometric configuration.

Furthermore, the hydrodynamic coefficients used in the simulation were assumed based on a smooth surface. However, in real-world applications, marine growth, fouling or surface roughness could affect these coefficients, leading to different hydrodynamic loading conditions. Variations in diameter or hydrodynamic coefficients alters the forces acting on the pipe and changing its dynamic behavior accordingly.

Additionally, the system layout considered only one pipe orientation, with the pipe located at the midpoint of the mooring system. The largest excursions of a semi-submersible platform occur in the mooring direction, so the responses in the current configuration may not represent the worst-case scenario.

The hydrogen electrolyzer was modeled on a semi-submersible, and the motion response of this substructure influences the behavior of the pipe at its connection point. The semi-submersible design, which uses a catenary mooring system, experiences large horizontal excursions compared to other substructure and mooring types. The larger horizontal excursions of the semi-submersible results in more pronounced curvatures in the pipe. Substructures such as spars exhibited larger rotational responses due to its deeper draft, possibly affecting curvature at the HOP more than semi-submersibles. Semi-submersibles tend to experience higher wave-induced motions, resulting in greater heave responses that alters the vertical position of the SB. TLPs respond differently due to their higher natural frequencies, and provide greater motion restriction. Both spars and TLPs experience less transnational motion than semi-submersibles, reducing the need for a lazy wave configuration since the decoupling function becomes less critical. Additionally, the motion response of the FOWT with a catenary mooring system is expected to be larger compared to a taut-leg system. This reduces tension and curvature along the pipe's length, resulting in smaller values and sensitivity rates, making the catenary configuration more favorable.

The mass of the hydrogen electrolyzer on the FOWT was not considered. Adding the electrolyzer would shift the center of mass and adjust the inertia of the FOWT, effecting the response to external loading. However, this could lead to larger motions once the FOWT begins to move, as the increased mass distribution would store more energy. These larger motions would affect the overall tension and curvature in the pipe. Additionally, while the pipe was centered in the middle of the structure, rotational motions at the ends of the substructure could result in larger motion responses an inaccuracies.

The aerodynamic decoupling of the turbine blades neglects the rotational effects. Variations in wind speed across blade height, gusts and turbulence were not considered, leading to a single constant point force at the RNA. The substructure's motions are thus not influenced by the aerodynamic effects of the turbine blades. Additionally, due to the pipe's central position, the rotational motion of the substructure is minimizes the impact at this location.

During the environmental study, different directionalities were considered, and the in-line direction resulted in the largest curvature response at the BS. However, after review, the de-coupled aerodynamic model not directly implemented the thrust and drag forces considering changes in direction. These forces were always assumed to be acting in the 0-degree direction, rather than the actual wind direction. This results in a curvature drop for opposite directions, even though curvature would have increased in counter directional (180 degrees) in-line environmental loading due to an increased movement and elongation.

Furthermore, the simulations modeled environmental scenarios using increments of 30 degrees relative to each other. However, the roses from complex areas often show that the wind, wave, and current directions can be significantly misaligned. This misalignment would result in a higher elongation of pipe or different wave configuration responses to the larger misaligned directional wave and currents than those captured.

Single sea states for an irregular sea were compared, while it did not explore the effects of different seed numbers on the randomness of wave frequencies. This frequencies and amplitudes could lead to different dynamic responses, potentially resulting in more extreme conditions than those used. Additionally, the response of the FOWT was evaluated relative to peak wave periods. In an irregular sea state, a range of wave frequencies may occur, not solely dependent on the single peak period, potentially exciting resonance at specific RAO frequencies. These effects may not have been captured in the analysis due to the lack of randomness. Furthermore, a resonance peak was found for yaw moments at low wave periods, suggesting that torsional stresses on the pipe could pose a risk to its multi-layer structure's integrity.

The design of the BS in this research was based on a single set of environmental conditions. The above mentioned directional conditions would have resulted in larger curvature at the HOP, thereby effectively a different and larger design of the BS to accommodate for the increased curvature. However, different pipe specifications and environmental conditions would require a different BS design.

The simulation parameters are tailored to the specific configuration and environmental conditions. However, varying these parameters may necessitate adjustments to the simulation settings to optimize performance under different scenarios. For instance, larger wave heights or lengths could require extended simulation or build-up times to fully capture the relevant physical effects, which might not be adequately represented in this irregular sea state. Additionally, alternative geometrical configurations with smaller bends might necessitate a finer target segment length to accurately model its curvature.

A critical error in this research was the incorrect implementation of hydrogen density during the simulations. The density was modeled at ten times its actual value, leading to inaccurate buoyancy calculations. Due to this error, the configurations were modeled with less buoyancy than necessary. If the correct hydrogen density had been used, the pipe would have been more buoyant. In the exact same scenario with similar amount of buoyancy, this results in a larger curvature TDP and at the BS, and a decrease in tension at the HOP as well.

Differences between the static and dynamic analyses revealed that increasing water depth leads to greater height differences due to larger variations in the geometric shape in the dynamic analysis. Furthermore, as water depth increases, the contribution of static tension forces becomes more significant, while the dynamic contributions decrease. Conversely, for curvature, dynamic contributions become more significant at the HOP, while less for lower positioned locations. This was observed in all scenarios, though different pipe properties could lead to different results. A heavier pipe, for example, would have increased inertia and thus be less affected by dynamic forces, while a larger diameter would result in increased drag and surface area, influencing the dynamic response. Furthermore, the FOWT's motion response directly impacts the HOP behavior, with lower floater motions reducing the pipe's dynamic contribution.

If the pipe's structural parameters, such as weight or diameter, increase, the system becomes less sensitive to dynamic environmental forces due to the higher moment of inertia. The additional mass also increases the static load, requiring more buoyancy to minimize tension and curvature. In this research, when the turbine and electrolyzer operate at full capacity, a smaller pipe is sufficient to transport the full volume of hydrogen produced. This reduction in pipe size decreases the static load due to the lower mass, but it also makes it more vulnerable to dynamic forces. Consequently, the dynamic contribution has a more pronounced effect, resulting in greater variations in tension and curvature during dynamic analysis. This can lead to different outcomes in static and dynamic analysis, potentially determining whether the pipe performs successfully or fails under varying conditions. Furthermore, in more extreme conditions, such as increased wave amplitudes, larger height differences may be observed at the SB, while an increase in current speed could result in greater curvature, depending on its direction. In scenarios where wind and waves are aligned while the current is counter-directed, an increase in curvature, particularly at the bends, is expected.

The results are constrained by both physical, the MBR and MBL, and operational, the clearances, criteria. In most scenarios, the operational constraints were more limiting than the physical constraints, especially in shallow water scenarios. Physical constraints were only approached and exceeded in extreme scenarios where the total length of the pipe became excessively short. These scenarios caused an additional axial loading and bending at the HOP in stretched configurations, where the pipe was unable to maintain seabed contact. Looping at the TDP was observed earlier than the breaching of the MBR in excessively long scenarios. Compression at the TDP occurred in scenarios where the pipe either touched the sea surface or looped due to excessive length.

Operational constraints are provided for clearances at the seabed and sea surface to prevent contact or interference with the surrounding environment. Seabed clearance was set at 10 meters, limiting pipe contact at the sag bend and the transition between buoyant and non-buoyant sections. However, this clearance could be reduced. It was observed that at the transition from the buoyant to the non-buoyant section (Point E), dynamic analysis showed minimal to no height difference, with smaller effect for an in increase in water depth. Thus, the 10-meter clearance, based on this environmental condition, appears conservative. Since the wave decouples the motion, the height difference at this point is expected to have minimal influence under other environmental conditions as well. However, considering marine growth over time, the height difference could effectively lower the pipe's position. Additionally, in scenarios where the buoyant section is smaller, point E would be positioned higher vertically, resulting in less likelihood of exceeding this constraints. The sea surface clearance was set at 50 meters, but reducing this value could result in more successful configurations. This reduction would be particularly helpful in limiting tension at the HOP by shortening the free-hanging length, which is especially relevant for power DPCs but not as necessary for flexible pipes.

The tension threshold at the TP is set at 5 kN, where this research considers non-burial scenarios. Burial would increase the frictional surface area, resulting in higher energy dissipation, leading to shorter allowable (horizontal) pipe length. However, this would increase tension and curvature at the TDP due to greater restrictions. Burial would recommended for shallower waters to mitigate the risk of collisions with objects or other operational hazards.

The hypothetical pipe design intended to meet minimal specifications, reducing the amount of material and layers to create conservative estimates for both tension and curvature limits. However, looping at the TDP occurred without exceeding the MBR, while MBR and MBL exceedance was observed only in scenarios with non-optimal wave configurations. Increasing the design's robustness, such as adding layers or using alternative materials, would even enhances the pipe's axial load capacity, resulting in scenarios were exceeding these limits even has a lower probability. For instance, collapse limits were surpassed at 600m, while the collapse limit (510 meters) was disregarded, where tensile and bending stresses remained within acceptable ranges. This suggests that the collapse limit presents a higher risk of failure than tension or bending. To account for deeper waters, adjustments to the pipe's carcass could increase the collapse limit, although this would also increase the MBR.

A 30% utilization factor was applied to both MBL and MBR, allowing for comparisons between distributed buoyancy with DCM and discrete buoyancy with FCM. This factor was calculated at a single location and time step in a dynamic scenario, rather than across multiple points or accounting for maximum variations over time, making it less reliable for extended studies. This utilization factor was also applied in static scenarios, where it likely leads to overestimation, as static analysis neglects external forces such as hydrodynamic drag and added mass, which are influenced by the surface area of the buoyancy setup. In static configurations, smaller discrepancies are expected due to the absence of these external forces, whereas dynamic analysis introduces more pronounced variations in curvature and structural response. Additionally, this discrepancy percentage was observed in curvature comparisons, yet lower discrepancy values were noted in tension comparisons. While conservative for tension, as it is primarily influenced by the coupling method rather than the buoyancy method, the curvature could be underestimated. Curvature was found to be more dominant than tension in terms of failure risk, since larger values are observed. Therefore, utilization factors for curvature should be determined at specific locations within the buoyancy sections, where the largest variations occur, such as at the pipe-to-BM connections. In addition, environmental conditions result in similar effects on shape and response behavior when distributed BM are used. However, if discrete BMs were adopted, different characteristics in dynamic scenarios would emerge, especially concerning its surface area and dynamic response behavior. Discrete BMs would increase localized drag and create higher dynamic forces, whereas the uniform buoyancy line maintains a smoother dynamic profile, reducing the overall drag and leading to more stable behavior under environmental loading. This could potentially result in more pronounced curvature variations in discrete methods, indicating possible underestimation.

The results of the parameter variations were mainly governed by operational constraints. This resulted nearly identical allowable ranges for parameters to decrease or increase before reaching their limits in different water depths in static an dynamic analysis. Dynamic analysis showed a 22% contribution in curvature and a 14% contribution in tension, averaged across all scenarios and all locations. As water depth increases, the dynamic contribution decreases. However, greater variations in dynamic tension were observed compared to curvature at larger depths, indicating that the dynamics have a more pronounced effect on curvature when comparing different water depths. Despite this, the dynamic contribution remained relatively small in relation to the maximum loading observed for both tension and curvature. This suggests that static analysis provides a simpler and faster solution, as both static and dynamic analyses yielded similar results in passing or failing the MBL and MBR limits at comparable parameter ratios. Thus the dynamic contribution is small compared to the pipe's maximum capacity. As previously discussed, when a smaller pipe is used, the dynamic contribution can become more pronounced.

The parametric study evaluated six parameters, with similar behavior observed across the buoyancy section parameters (OD_{BM}, d_{BM}, L_2) and the parameters influencing its total configuration (L_{total}, x_{TP}). Given the similarity, investigating changes in individual parameters may be redundant. This allows the lazy wave configuration to be designed using only three parameters: a buoyancy section parameter, a total length configuration parameter, and L_1, while keeping the other parameters constant. Based on the buoyancy forces required to form the lazy wave configuration, a combination of the three buoyancy section parameters could be optimized. Alternatively, varying only the cost-driving parameter while keeping the other two constant could minimize expenses. Financial considerations may also guide the recommendation for a minimal L_{total} with varying x_{TP}.

In the sensitivity analysis, results were based on the average of all successful scenarios, excluding those that did not meet the criteria. This approach linearized the increase or decrease rates for tension and curvature across all successful scenarios, and estimated the effects of a 10% variation in parameter values. However, these sensitivity rates are not directly measured but are instead estimated as averages over single parameter variations. Additionally, this linearization limits the ability to capture exponential responses from excluded scenarios. In particular, scenarios with fewer successful cases, such as those involving variations in d_{BM}, required interpolation of the results, increasing the likelihood of deviations from the actual 10% increase or decrease in parameter variations. However, important to note is that these excluded scenarios represent configurations which are positioned near the sea surface and seabed. Nonetheless, the static and dynamic analyses showed similar sensitivity responses, indicating that parameter changes should produce comparable effects in both analyses. This linearization underestimates or overestimates tension and curvature responses due to non-linear behavior from parametric variations. The issue is further complicated by visualizations based on the comparison around its base value, while sensitivities are thus measured across all scenarios. The pre-determined allowable ranges, however, try to limits these inaccuracies.

The research focuses on the lazy wave configuration, but the results indicate that a catenary configuration could be a viable option, particularly from a financial perspective. Maximum tension at the HOP occurs only when the vertical distance from the pipe's end exceeds 1000 meters, with looping at the TDP happening before the MBR is exceeded. The catenary configuration reached approximately 75% of its curvature limit at the TDP in 200m water depth of water, with more significant curvature effects than in 400m and 600m water depth. In contrast, the lazy wave configuration decouples the motion of the FOWT from the TDP, reducing curvature at TDP and the tension and HOP by around 50%. This reduction could minimize fatigue damage at the TDP by lowering stress variations. Unlike the catenary configuration, the direct coupling of FOWT to the TDP, this could increase the risk of fatigue. Although this research did not explicitly examine fatigue, the lazy wave is recommended as a potential mitigation strategy.

A parametric study for a lazy wave configuration would be more applicable to DPC design than to flexible pipes, as the constraints of MBL and MBR for flexible pipes are less stringent. When comparing the bending stiffness of pipes to DPCs, axial stiffness is greater in DPCs, while their bending stiffness is lower, with a lower MBL and higher MBR. This necessitates for careful design for DPCs, especially at high loading points like the HOP and at the transition from buoyant to non-buoyant section. Additionally, DPCs are more flexible and require larger bend radii, which demand greater horizontal excursions in the wave shape. A more dispersed distribution of buoyancy is needed to achieve larger radii at the hog and sag bends, ensuring also a smooth transition at the TDP.

5.2. Limitations

Throughout the research, certain assumptions limit its applicability to other scenarios and studies. These are as follows:

- The numerical software interprets the pipe using the beam theory, which neglects lateral restrictions and local effects between individual layers of the pipe. As a result, the global response behavior is modeled, but the specific behavior between each individual layer is not accounted for. This simplification impacts accuracy, particularly in scenarios where interactions between layers are critical under high bending moments. For example, local buckling or delamination between layers could occur in reality but remain undetected in the global beam model. Consequently, this overestimates the pipe's load-bearing capacity.
- Several failure modes were evaluated, including tension, overbending, compression, and collapse; however, other failure modes were not investigated. The design constraints of MBL, MBR, and the collapse limit suggest that while MBL and MBR are significant, the key design drivers in terms of physical constraints have yet to be clearly identified. Fatigue failure, which was not examined due to the complexity of the pipe's multi-layer structure, could provide valuable insights if incorporated into the evaluation criteria. This would require converting the structural response from a global to a local layer level. A full conversion to the local level at its most vulnerable layer, offering greater clarity on the likelihood of successful scenarios. Additionally, torsional stresses were excluded from the analysis, despite their potential to increase tension due to the helically oriented armor wires.
- The scenarios focused on a single layout, with the pipe positioned at the midpoint of the mooring system. Additionally, it did not account for the randomness of environmental loads, which could introduce variability in wave conditions that were not considered. This suggests that the most extreme motion and structural responses may not have been captured. Consequently, the sensitivity analysis is limited to this specific FOWT scenario and the environmental conditions simulated here.
- Environmental factors, such as marine growth, were not considered. Marine growth can affect the pipe's geometry and response over time by increasing its weight and altering its hydrodynamic properties. Additionally, VIV conditions were not simulated, despite their possible impact on fatigue. In particular, this location, which experiences large variations in current speed and direction, could

make VIV a dominant factor, potentially requiring adjustments to the pipe structure if needed.

- The DLCs were specifically tailored for the design of an FOWT in a decentralized layout. If a centralized or semi-centralized layout were considered, the pipe design and DLCs would need to be re-evaluated for a dynamic riser configuration connected to different floating substructures. In a centralized layout, the hydrogen production unit would be located on a separate floating structure, which would respond differently to similar environmental conditions compared to the FOWT used in this research. Furthermore, in a centralized layout, multiple pipes or a larger-diameter pipe would be required to transport the increased volume of hydrogen. Different pipe specifications would result in varying characteristics and impacts on structural response. For instance, increases in both axial and bending stiffness would reduce flexibility and alter the pipe's load-bearing capacity, necessitating recalibration of the design to accommodate these changes. In addition, the internal fluid parameters were modeled as constant throughout the pipe. However, variations in internal flow speed and pressure, particularly due to elevation changes, affects bending stiffness.
- Between the TDP and TP, the seabed was modeled as a contact surface with friction, but complexities such as soil displacement or accumulation in front of the pipe were not considered. These factors alters the pipe's behavior, especially in counter-directed environmental conditions relative to the pipe layout. Accurately capturing these effects would result in higher curvature at the TDP due to increased movement restriction.
- Lastly, the water depth was scaled from 200m to 400m and 600m, with corresponding adjustments to the mooring lines. However, in realistic scenarios, the mooring line configuration would differ. A fully chain-based catenary mooring system becomes impractical at greater depths due to the excessive weight of the mooring lines. In deeper waters, a combination of synthetic and chain ropes is more suitable, resulting in larger horizontal and smaller vertical motions responses for the FOWT.

6

Conclusion and Recommendations

This chapter presents the conclusions drawn from the research in section 6.1, followed by recommendations for future work in section 6.2.

6.1. Conclusion

This research has provided an investigation into the structural response of flexible pipes deployed in a lazy wave configuration for offshore hydrogen transportation from semi-submersible FOWT, spanning from the HOP to the TP. The researched focused on how configurational parameters influence the pipe's tension and curvature. The first part of the study gave an overview of the technology and design considerations for flexible pipes. This was followed by a detailed discussion of the methodology, which included a preliminary analysis and the setup of a parametric study that formed the foundation for the numerical modeling. This chapter presents the conclusions drawn from this research. The objective is to answer the main research question:

What impact do parameters of lazy wave configurations have on the tension and curvature of flexible pipes connected to a semi-submersible FOWT in hydrogen applications?

The design of the lazy wave configuration was assessed through static and dynamic analyses. Numerical modeling was performed using OF software, which employs a finite-element model based on the beam theory, simplifying the interactions between pipe layers and providing a global approach of the pipe's structural behavior. The DCM in OF provided the FOWT motion response as input for the pipe's motion at the HOP, along with metocean conditions. The pipe was designed for hydrogen applications using in-house software from the pipe manufacturer. The design constraints considered the failure modes of tension, compression, overbending, and collapse. The research evaluated a single top-view system layout, incorporating recommended configurational parameters optimized from DPCs as the reference scenario. The BMs were distributed along the buoyant section, and the BS was tailored to its specific purpose. Environmental conditions, including wind, waves, and currents, were modeled using omni-directional inputs combined with DLCs for a FOWT, focusing on the combination of directions that induced the largest structural responses. The parametric study varied six configurational parameters: the outer diameter of the buoyancy modules (OD_{BM}), the pitch (d_{BM}), the first section length (L_1), the second section length (L_2), the total length (L_{total}), and the horizontal position of the termination point (x_{TP}). These parameters were evaluated at water depths of 200m, 400m, and 600m.

The lazy wave configuration cannot be fully designed or optimized based solely on the failure modes of tension, overbending, compression, and collapse, as operational constraints govern the design rather than its physical constraints. These physical limits are only exceeded in scenarios where the wave configuration is non-optimal, such as in elongated or slacked configurations. The MBR is exceeded earlier than the MBL, indicating that bending radius is a more dominant constraint than tensile load in such scenarios. The limits of the MBL and MBR are breached when compression has already occurred, when looping begins at the TDP, or when the collapse limit has already been exceeded. Therefore, tension and curvature loading are not the primary design drivers, yet other factors such as fatigue or VIV, which were not considered in this research, may ultimately govern the pipe's design. This leads to two possible conclusions regarding the pipe's axial and bending capacity: either the pipe is overdesigned, suggesting that material and cross-sectional parameters could be minimized by the manufacturer, or the lazy wave configuration is not the optimal solution for this flexible pipe.

The lazy wave configuration reduces tension at the HOP and curvature at the TDP compared to a catenary configuration. In the lazy wave setup, the MBL is reached at the HOP when a pipe of approximately 1000m is hanging from this location, and looping occurs earlier than when the MBR is exceeded at the TDP. Tension at the HOP and curvature at the TDP are reduced by up to 50% in the lazy wave configuration, while the catenary remains within acceptable limits as well. Consequently, a lazy wave configuration should only be considered when a catenary is unsuitable, as the catenary is simpler and generally a more cost-effective option. However, failure modes not investigated could become key design drivers, as direct movement transfer to the TDP may increase the risk of failure due to repetitive contact with the seabed. A small wave configuration near the seabed can effectively reduce curvature, leading to improved stress distribution. To ensure a holistic understanding of its application, the lazy wave design must incorporate techno-economic and operational criteria, along with the consideration of additional failure modes.

Both static and dynamic analyses were conducted, with the comparison focusing on the dynamic contribution, which showed minimal differences. The pipe's geometric shape exhibited the most variation in vertical displacement at the SB, primarily due to the direct influence of FOWT motion. The lazy wave configuration effectively decouples the FOWT's movement, reducing its impact on the pipe beyond the wave section. Without this configuration, the FOWT motion would be directly transferred to the TDP.

The structural response to static effects contributes, on average, 86% of the total tension and 78% of the total curvature, resulting in only a small influence by environmental factors. This indicates that static loading from the pipe's weight and buoyancy is significantly more dominant than dynamic loading. As a result, static development forms the basis for the initial configuration, where shape, curvature, and tension are minimally affected by the addition of environmental factors. As water depth increases, the dynamic contribution to tension and curvature decreases. Consequently, as FOWTs are deployed farther from shore, environmental loading becomes less significant, with static loading becoming increasingly important in deeper and more remote FOWT scenarios. Curvature exhibited more pronounced variations and higher normalized values across different scenarios compared to tension, making it a more critical design constraint. Larger deviations in curvature were observed due to dynamics, especially when comparing different water depths. Tension remained relatively consistent, emphasizing that the curvature constraint is more critical, as this exhibits greater variability across different configurations and consequently in various applications.

The comparison of static and dynamic analyses shows that the pipe's design constraints, MBL and MBR, can be effectively evaluated through static development rather than a dynamic development in the initial design phase, as similar scenarios failed in both static and dynamic analyses based on these constraints. While dynamic effects are important for cyclic loading over time, they require more computational resources and have minimal influence on tension and curvature. Therefore, performing initial static developments offers a quicker approach for designing lazy wave configurations focused on tension and bending. For dynamic analyses, however, additional failure modes beyond tension, overbending, compression, and collapse should be incorporated.

Regarding the configurational parameters, several observations can be made. Parameter variations showed slightly more pronounced changes in tension and curvature when environmental loading was included. Additionally, environmental loading affected the pipe uniformly along its full length, with its influence decreasing with depth in the water column, indicating a reduced overall response to parameter variations in static analysis. For an increase in water depth, tension and curvature responses begin to converge, suggesting similar behavior beyond a certain depth.

The lazy wave configuration paramaters can be effectively designed using three distinct groups of parameters. The grouped parameters governing the buoyant section (OD_{BM}, d_{BM}, and L_2) and those governing the overall configuration (L_{total} and x_{TP}) showed similar responses in terms of shape variation and structural behavior. The environmental factors have minimal influence where different buoyant section configurations show negligible differences in response. For L_{total} and x_{TP}, the primary difference lies in the static horizontal length on the seabed (L_{ST}), which affects energy dissipation and tension at the TP.

The MBL and MBR limits were only exceeded in stretched scenarios due to variations in L_{total} and x_{TP} or when the buoyant section was positioned near the surface due to changes in L_1. Additionally, only these parameters caused compression at the seabed. Therefore, these parameters have the greatest impact on failure modes, while variations in the buoyant section parameters never led to exceeding the physical limits. Instead, the buoyant section parameters are governed by operational criteria. However, the failure modes of tension, compression, and overbending observed in these scenarios occurred in unrealistic or undesirable configurations for the lazy wave design, as they coincided with exceeding operational constraints. This demonstrates that operational limits, rather than physical ones, are the dominant design drivers for the lazy wave configuration. This highlights that the lazy wave configuration can be designed primarily based on operational criteria, given its high MBL and lower MBR limits.

Both grouped parameter combinations exhibit similar behavior in tension and curvature variation along the pipe's length. Therefore, the six parameters investigated can be reduced to three: a buoyant section parameter, L_1, and a parameter defining the overall lazy wave configuration. Limiting the design to these three parameters, while keeping the remaining ones constant, simplifies comparison evaluations by reducing the range of possibilities. The selection of these parameters is guided by financial incentives; for example, adjusting the BM diameter has a smaller cost impact compared to increasing the number of BMs, while modifying the TP has no effect on pipe costs, unlike changes to the total length.

Based on the sensitivity analysis, water depths of 400m and 600m yield similar outcomes for tension and curvature compared to 200m, indicating that parameter variations behave differently at varying depths. As water depth increases, after a certain depth (400m in this research), maximum curvature responses begin to converge to a minimum, while tension gradually increases. However, even at 600m, normalized curvature shows larger values than normalized tension. At all depths, curvature remains the more critical constraint, though tension may become more significant in deeper waters not investigated. The larger normalized values observed for curvature suggest that the lazy wave configuration is more suitable for shallower waters, though this has not been investigated below 200m.

Grouped parameters influencing the buoyant section (OD_{BM}, d_{BM}, and L_2) and the overall configuration (L_{total} and x_{TP}) follow consistent sensitivity rates, listed from largest to smallest, across the full length for both curvature and tension. Thus, the outer diameter of the BM (OD_{BM}) is always the most sensitive parameter within the buoyant section, while total length (L_{total}) is more sensitive than the horizontal position (x_{TP}). From a financial perspective, for increasing buoyancy force, it is more efficient to increase OD_{BM} rather than decreasing d_{BM}, and for reducing buoyancy, increasing d_{BM} is preferable over reducing OD_{BM}. Moreover, adjusting x_{TP} instead of L_{total} is recommended to optimize cost-efficiency.

The deduction of these three parameters leads to the following conclusions: tension at the HOP is most sensitive to L_1 across all water depths, although this parameter has the least influence on curvature and tension at other locations. Therefore, L_1 governs design considerations for HOP tension. Additionally, the objective of the lazy wave to decouple curvature at the TDP, indicates that L_{total} demonstrates greater sensitivity at 200m at this location, whereas OD_{BM} is more sensitive at 400m and 600m depths. Curvature and tension variation along the rest of the pipe varies between these two parameters. When financial considerations are included, x_{TP} becomes the most sensitive for curvature at the TDP across all depths, competing with d_{BM} for sensitivity in tension and curvature along the pipe. As a result, a lazy wave configuration can be optimized using L_1, OD_{BM}, and L_{total} with large sensitivity responses, while smaller sensitivities are driven by L_1, d_{BM}, and x_{TP}.

6.2. Recommendations

Several recommendations for further research can be made:

- **Fatigue and Accidental Failure Considerations**: The failure modes of tension, overbending, compression, and collapse are addressed. However, future studies should prioritize investigating other failure modes, such as fatigue at critical points, particularly where the largest stress variations occur, such as the HOP and TDP. This requires capturing all load cases within dynamic environments that influence fatigue behavior. Additionally, this analysis should be conducted at a local layer level, rather than at the global level. Coupling OF's global model with in-house software for local fatigue analysis will provide detailed insights into the layers most susceptible to failure. This is crucial, as the key design drivers are not based solely on MBL and MBR limits. Furthermore, accidental failures, such as pipe collisions with surrounding components or mooring line failures, should be studied, including the risks associated with hydrogen dissipation in submerged environments.

- **Techno-Economic Optimization of Pipe Design**: Optimization should be explored by comparing a minimum required pipe design for a lazy wave configuration with the maximum required design for a catenary configuration. This comparison should be based on material properties and cross-sectional dimensions that determine the capacity of the MBL and MBR. The goal is to evaluate the robustness needed for a lazy wave configuration and identify the specific pipe design where a lazy wave becomes more suitable instead of a catenary. A techno-economic analysis is essential to assess cost-effectiveness while maintaining structural integrity. Scenarios comparing a less robust pipe with expensive BMs to a more robust pipe without buoyancy should eventually offer valuable insights into cost-benefit trade-offs.
- **Evaluation of Alternative Configurations**: Future studies should explore combinations of configurational parameters to achieve more optimized solutions. In addition, alternative configurations, such as the lazy-S or tethered configurations, should also be evaluated for their viability under different operational conditions. Particularly in centralized layouts requiring multiple risers, the lazy-S configuration may offer advantages. On the other hand, combining a catenary configuration with a tether at the TDP could offer a viable solution in shallower waters, as curvature at the TDP in a standard catenary setup may pose constraint challenges.
- **Comparative Structural Analysis of Umbilical Systems**: A comparative study of the structural behavior of flexible pipes and DPCs is necessary. Different applications in both centralized and decentralized layouts will require distinct umbilical systems, highlighting the potential need for multiple specialized umbilical systems, each with unique properties, in the future. This integration of both DPCs for electricity and flexible pipes for hydrogen transport within a single wind farm would enable a comparison of structural responses across various floating substructures and environmental conditions. Such an approach would help determine the most optimal umbilical system for a specific wind farm application and location.
- **Incorporation of Additional Environmental Effects**: This study did not consider additional environmental factors, such as VIV and marine growth. VIV can lead to large-amplitude oscillations that affect structural integrity, while marine growth alters the mass and drag characteristics of the pipe over time. Future studies should investigate and incorporate these factors to provide a more realistic representation and to better assess the pipe's suitability and integrity in long-term applications.

References

[1] Hannah Ritchie et al. “Population Growth”. In: *Our World in Data* (June 2024). URL: `https://ourworldindata.org/population-growth` (visited on 08/31/2024).

[2] *EIA projects nearly 50% increase in world energy use by 2050, led by growth in renewables - U.S. Energy Information Administration (EIA)*. URL: `https://www.eia.gov/todayinenergy/detail.php?id=49876` (visited on 08/31/2024).

[3] United Nations Climate Change: *Key aspects of the Paris Agreement*. https://unfccc.int/. URL: `https://unfccc.int/most-requested/key-aspects-of-the-paris-agreement` (visited on 10/12/2024).

[4] Jerry L. Holechek et al. “A Global Assessment: Can Renewable Energy Replace Fossil Fuels by 2050?” en. In: *Sustainability* 14.8 (Apr. 2022), p. 4792. ISSN: 2071-1050. DOI: `10.3390/su14084792`. URL: `https://www.mdpi.com/2071-1050/14/8/4792` (visited on 08/31/2024).

[5] Dolf Gielen et al. “Global Energy Transformation: A Roadmap to 2050”. en. In: (Apr. 2019). URL: `https://www.h2knowledgecentre.com/content/researchpaper1605` (visited on 08/31/2024).

[6] Jochen Markard and Regula Petersen. “The offshore trend: Structural changes in the wind power sector”. en. In: *Energy Policy* 37.9 (2009), pp. 3545–3556. URL: `https://ideas.repec.org//a/eee/enepol/v37y2009i9p3545-3556.html` (visited on 08/31/2024).

[7] Mehmet Bilgili, Abdulkadir Yasar, and Erdogan Simsek. “Offshore wind power development in Europe and its comparison with onshore counterpart”. en. In: *Renewable and Sustainable Energy Reviews* 15.2 (Feb. 2011), pp. 905–915. ISSN: 13640321. DOI: `10.1016/j.rser.2010.11.006`. URL: `https://linkinghub.elsevier.com/retrieve/pii/S1364032110003758` (visited on 08/31/2024).

[8] Rebecca Williams and Fheng Zhao. *GLOBAL OFFSHORE WIND REPORT 2023*. Tech. rep. Brussels, Belgium: Global Wind Energy Council, Aug. 2023.

[9] *World’s First Floating Offshore Wind Farm Achieves 65% Capacity Factor After 3 Months*. URL: `https://www.greentechmedia.com/articles/read/worlds-first-floating-offshore-wind-farm-65-capacity-factor` (visited on 12/18/2023).

[10] Rhodri James and Marc Costa Ros. *Floating Offshore Wind: Market and Technology Review*. UK. June 2015.

[11] *Fixed versus floating offshore wind | Guide to a floating offshore wind farm*. en-GB. URL: `https://guidetofloatingoffshorewind.com/fixed-versus-floating-offshore-wind/` (visited on 12/18/2023).

[12] “A Tutorial on the dynamics and Control of Wind Turbines and Wind Farms”. eng. In: ed. by American Automatic Control Council. Piscataway, NJ: IEEE, 2009. ISBN: 9781424445240 9781424445233.

[13] *Floating offshore wind market technology review*. en. Jan. 2020. URL: `https://www.carbontrust.com/our-work-and-impact/guides-reports-and-tools/floating-offshore-wind-market-technology-review` (visited on 12/18/2023).

[14] Rosamund Pearce. *Q&A: How viable are floating offshore windfarms?* en. July 2017. URL: `https://www.carbonbrief.org/qa-how-viable-are-floating-offshore-windfarms/` (visited on 12/18/2023).

[15] Mary Harvey et al. *Floating Wind Joint Industry Programme – Phase IV Summary Report*. en. Tech. rep. July 2022. URL: `https://www.carbontrust.com/our-work-and-impact/guides-reports-and-tools/floating-wind-joint-industry-programme-phase-iv-summary-report` (visited on 12/18/2023).

[16] *Offshore Wind Outlook 2019 – Analysis*. en-GB. URL: `https://www.iea.org/reports/offshore-wind-outlook-2019` (visited on 12/16/2023).

[17] Martijn. *Unlocking the Green Hydrogen Economy through Business Model Innovation*. en. Mar. 2021. URL: `https://eghac.com/unlocking-the-green-hydrogen-economy-through-business-model-innovation/` (visited on 12/16/2023).

[18] *HYBRIT - Vattenfall partnership with LKAB and SSAB*. en. URL: `https://group.vattenfall.com/what-we-do/roadmap-to-fossil-freedom/industry-decarbonisation/hybrit` (visited on 10/13/2024).

[19] *The wheels on the hydrogen bus go round and round in Aberdeen*. en. URL: `https://cordis.europa.eu/article/id/429071-the-wheels-on-the-hydrogen-bus-go-round-and-round-in-aberdeen` (visited on 10/13/2024).

[20] Jim Green et al. “Electrical Collection and Transmission Systems for Offshore Wind Power”. In: *All Days*. Houston, Texas, U.S.A.: OTC, Apr. 2007, OTC–19090–MS. DOI: `10.4043/19090-MS`. URL: `https://onepetro.org/OTCONF/proceedings/07OTC/All-07OTC/OTC-19090-MS/37841` (visited on 12/15/2023).

[21] *DNV study shows high offshore hydrogen infrastructure potential for Europe*. en. Mar. 2023. URL: `https://www.dnv.com/news/dnv-study-shows-high-offshore-hydrogen-infrastructure-potential-for-europe-241164/` (visited on 08/31/2024).

[22] Yann Poirette et al. “An Optimization Method for the Configuration of Inter Array Cables for Floating Offshore Wind Farm”. en. In: *Volume 10: Ocean Renewable Energy*. Trondheim, Norway: American Society of Mechanical Engineers, June 2017, V010T09A072. ISBN: 978-0-7918-5778-6. DOI: `10.1115/OMAE2017-61655`. URL: `https://asmedigitalcollection.asme.org/OMAE/proceedings/OMAE2017/57786/Trondheim,%20Norway/282139` (visited on 11/22/2023).

[23] Manuel U. T. Rentschler et al. “Parametric study of dynamic inter-array cable systems for floating offshore wind turbines”. en. In: *Marine Systems & Ocean Technology* 15.1 (Mar. 2020), pp. 16–25. ISSN: 1679-396X, 2199-4749. DOI: `10.1007/s40868-020-00071-7`. URL: `http://link.springer.com/10.1007/s40868-020-00071-7` (visited on 11/21/2023).

[24] Sayeed Rushd and Mohamed Ismael. *Pipeline Engineering - Design, Failure, and Management*. en. 10.5772/intechopen.102290. InTechOpen, Mar. 2023. ISBN: 978-1-83768-000-9. DOI: `DOI`. URL: `https://www.intechopen.com/chapters/85818`.

[25] Karen Bybee. “Analytical Tools Optimize Unbonded Flexible Pipes for Deepwater Environments”. en. In: *Journal of Petroleum Technology* 56.05 (May 2004), pp. 48–50. ISSN: 0149-2136, 1944-978X. DOI: `10.2118/0504-0048-JPT`. URL: `https://onepetro.org/JPT/article/56/05/48/110661/Analytical-Tools-Optimize-Unbonded-Flexible-Pipes` (visited on 11/01/2023).

[26] API. “API 17B: Recommended Practice for Flexible Pipe”. en. In: *Technical report, American Petroleum Institue (API)* (July 1998), p. 141.

[27] Dag Fergestad and Svein Are Løtveit. *Handbook on Design and operation of flexible pipes*. en. NTNU, 4Subsea and SINTEF Ocean, June 2017.

[28] “The integrity of flexible pipe: search for an inspection strategy”. en-US. In: *Engineering Structures* 17.4 (May 1995). Publisher: Elsevier, pp. 305–314. ISSN: 0141-0296. DOI: `10.1016/0141-0296(95)00028-6`. URL: `https://www.sciencedirect.com/science/article/pii/0141029695000286` (visited on 11/01/2023).

[29] I Kraincanic and E Kebadze. “Slip initiation and progression in helical armouring layers of unbonded flexible pipes and its effect on pipe bending behaviour”. en. In: *The Journal of Strain Analysis for Engineering Design* 36.3 (Apr. 2001), pp. 265–275. ISSN: 0309-3247, 2041-3130. DOI: `10.1243/0309324011514458`. URL: `http://journals.sagepub.com/doi/10.1243/0309324011514458` (visited on 11/01/2023).

[30] *State of the art Bonded Flexible Pipes 2018*. Tech. rep. 2.0. Norway: 4Subsea AS, Dec. 2018.

[31] API. “API 17J: Specification for Unbonded Flexible Pipe”. en. In: *Technical report, American Petroleum Institue (API)* (Jan. 2009), p. 85.

[32] F O Kolawole et al. “Mitigation of Corrosion Problems in API 5L Steel Pipeline – A Review”. en. In: (2018).

[33] Yong Bai and Qiang Bai. *SUBSEA PIPELINES AND RISERS*. en. First Edition. https://doi.org/10.1016/B978-0-08-044566-3.X5000-3. Oxford: Elsevier, Nov. 2005. ISBN: 0-08-044566-7.

[34] T CLAUSEN and R. D’SOUZA. “Dynamic risers key component for deepwater drilling, floating production”. In: *Dynamic risers key component for deepwater drilling, floating production* 61.5 (2001). Place: Tulsa, OK Publisher: Pennwell, pp. 89–93. ISSN: 0030-0608.

[35] Sadjad Karegar. “Flexible riser global analysis for very shallow water”. eng. MA thesis. University of Stavanger, Norway, 2013. URL: `https://uis.brage.unit.no/uis-xmlui/handle/11250/182926` (visited on 05/22/2024).

[36] Tang An-quan. “The Motion and Mooring Forces of a Turret Moored FPSO with the Wind,Waves and Currents Loads”. In: 2011. URL: `https://www.semanticscholar.org/paper/The-Motion-and-Mooring-Forces-of-a-Turret-Moored-An-quan/c69e05c7c1bca6073d074ac7dfeecd9ff0a1a3ad` (visited on 12/07/2023).

[37] Tapan K. Sen. “Probability of Fatigue Failure in Steel Catenary Risers in Deep Water”. en. In: *Journal of Engineering Mechanics* 132.9 (Sept. 2006), pp. 1001–1006. ISSN: 0733-9399, 1943-7889. DOI: `10.1061/(ASCE)0733-9399(2006)132:9(1001)`. URL: `https://ascelibrary.org/doi/10.1061/%28ASCE%290733-9399%282006%29132%3A9%281001%29` (visited on 12/01/2023).

[38] Tatiana Vargas-Londono et al. *A Theoretical and Experimental Analysis of the Bending Behavior of Unbonded Flexible Pipes*. Vol. 6. Journal Abbreviation: Proceedings of the International Conference on Offshore Mechanics and Arctic Engineering - OMAE Publication Title: Proceedings of the International Conference on Offshore Mechanics and Arctic Engineering - OMAE. June 2014. DOI: `10.1115/OMAE2014-24247`.

[39] Liping Sun and Bo Qi. “Global analysis of a flexible riser”. en. In: *Journal of Marine Science and Application* 10.4 (Dec. 2011), pp. 478–484. ISSN: 1671-9433, 1993-5048. DOI: `10.1007/s11804-011-1094-x`. URL: `http://link.springer.com/10.1007/s11804-011-1094-x` (visited on 12/06/2023).

[40] L. Martinelli et al. “Power Umbilical for Ocean Renewable Energy Systems - Feasibility and Dynamic Response Analysis”. In: Bilbao, Oct. 2010.

[41] Yong Bai and Qiang Bai. *Subsea Pipeline Integrity and Risk Management*. en. Google-Books-ID: rsz8CN4FBSEC. Gulf Professional Publishing, Feb. 2014. ISBN: 9780123946485.

[42] ISO. “Petroleum and natural gas industries: Design and operation of subsea production systems”. eng. In: *ISO 13628-11* (Feb. 2008), p. 222. ISSN: 978 0 580 63564 9.

[43] Max van der Tholen. “Parametric Optimization of Dynamic Power Cable Configurations for Floating Offshore Wind Applications”. en. In: Master Thesis (Feb. 2023), p. 130. DOI: `10.4043/6724-MS`.

[44] DNV-GL. *DNVGL-ST-0437: Loads and site conditions for wind turbines*. en. Nov. 2016.

[45] Safdar Rasool, Kashem Muttaqi, and Danny Sutanto. “Modelling Ocean Waves and an Investigation of Ocean Wave Spectra for the Wave-to-Wire Model of Energy Harvesting”. In: *Engineering Proceedings* 12 (Dec. 2021), p. 51. DOI: `10.3390/engproc2021012051`.

[46] Jorgen Fredsoe and B. Mutlu Sumer. *Hydrodynamics Around Cylindrical Structures (Revised Edition)*. en. Google-Books-ID: LLPICgAAQBAJ. World Scientific, Sept. 2006. ISBN: 978-981-4476-98-0.

[47] JMJ Journée and WW Massie. *OFFSHORE HYDROMECHANICS*. eng. First Edition. Delft: Delft University of Technology, Jan. 2001.

[48] Etienne Rivard, Michel Trudeau, and Karim Zaghib. “Hydrogen Storage for Mobility: A Review”. en. In: *Materials* 12.12 (Jan. 2019), p. 1973. ISSN: 1996-1944. DOI: `10.3390/ma12121973`. URL: `https://www.mdpi.com/1996-1944/12/12/1973` (visited on 12/11/2023).

[49] Ahmed M. Elberry et al. “Large-scale compressed hydrogen storage as part of renewable electricity storage systems”. en. In: *International Journal of Hydrogen Energy* 46.29 (Apr. 2021), pp. 15671–15690. ISSN: 03603199. DOI: `10.1016/j.ijhydene.2021.02.080`. URL: `https://linkinghub.elsevier.com/retrieve/pii/S0360319921005838` (visited on 12/11/2023).

[50] C. Tsiklios, M. Hermesmann, and T.E. Müller. “Hydrogen transport in large-scale transmission pipeline networks: Thermodynamic and environmental assessment of repurposed and new pipeline configurations”. en. In: *Applied Energy* 327 (Dec. 2022), p. 120097. ISSN: 03062619. DOI: `10.1016/j.apenergy.2022.120097`. URL: `https://linkinghub.elsevier.com/retrieve/pii/S030626192201354X` (visited on 12/08/2023).

[51] Arvind Keprate, R.M. Chandima Ratnayake, and Shankar Sankararaman. “Minimizing hydrocarbon release from offshore piping by performing probabilistic fatigue life assessment”. en. In: *Process Safety and Environmental Protection* 106 (Feb. 2017), pp. 34–51. ISSN: 09575820. DOI: `10.1016/j.psep.2016.11.019`. URL: `https://linkinghub.elsevier.com/retrieve/pii/S0957582016302890` (visited on 12/11/2023).

[52] E. Shashi Menon. *Gas pipeline hydraulics*. Boca Raton, FL: Taylor & FRancis, 2005. ISBN: 9780849327858.

[53] Jesse Blok. “Semi-centralised hydrogen production: A techno-economic analysis of offshore wind-to-hydrogen configurations”. en. In: (2023). URL: `https://repository.tudelft.nl/islandora/object/uuid%3A935a38bc-09a6-47c8-9f1d-c2284da437a3` (visited on 12/11/2023).

[54] Tomasz Włodek et al. “Thermodynamic analysis of hydrogen pipeline transportation – selected aspects”. en. In: *AGH Drilling, Oil, Gas* 33.2 (2016), p. 379. ISSN: 1507-0042. DOI: `10.7494/drill.2016.33.2.379`. URL: `http://journals.bg.agh.edu.pl/DRILLING/2016.33.2/379.php` (visited on 12/13/2023).

[55] Christelle Gabet et al. “Qualification of Flexible Pipes for Gaseous Hydrogen Transportation”. In: *Day 3 Wed, May 03, 2023*. Houston, Texas, USA: OTC, Apr. 2023, D031S040R001. DOI: `10.4043/32242-MS`. URL: `https://onepetro.org/OTCONF/proceedings/23OTC/3-23OTC/D031S040R001/519101` (visited on 12/14/2023).

[56] *NOV In-house data*.

[57] J. Muren. *Failure modes, inspection, testing and monitoring*. 2007.

[58] *Petroleum and natural gas industries. Design and operation of subsea production systems Flexible pipe systems for subsea and marine applications*. Definitive. OCLC: 9521588100. 2010. ISBN: 9780580635649.

[59] DNV-GL. *DNV OS-F201: Dynamic Risers.pdf*. en. Jan. 2018. (Visited on 11/08/2023).

[60] Jiahao Chen et al. “Comparisons of the dynamical characteristics of a semi-submersible floating offshore wind turbine based on two different blade concepts”. In: *Ocean engineering* 153.Elsevier (2018), pp. 305–318.

[61] Mert Kaptan et al. “Analysis of spar and semi-submersible floating wind concepts with respect to human exposure to motion during maintenance operations”. en. In: *Marine Structures* 83 (May 2022), p. 103145. ISSN: 09518339. DOI: `10.1016/j.marstruc.2021.103145`. URL: `https://linkinghub.elsevier.com/retrieve/pii/S0951833921001969` (visited on 08/22/2024).

[62] Qinglong Lei et al. “On the pressure–torsion response of a flexible pipe with section ovalization”. en. In: *Applied Ocean Research* 127 (Oct. 2022), p. 103297. ISSN: 01411187. DOI: `10.1016/j.apor.2022.103297`. URL: `https://linkinghub.elsevier.com/retrieve/pii/S0141118722002310` (visited on 08/22/2024).

[63] . “DNV-OS-F201: Dynamic Risers”. In: (2010).

[64] *Technical report: Definition of the IEA Wind 15-Megawatt Offshore Reference Wind Turbine*. 2020.

[65] *Technical Report: Definition of the UMaine VolturnUS-S Reference Platform Developed for the IEA Wind 15- Megawatt Offshore Reference Wind Turbine*. July 2020.

[66] DNV-GL. *DNV-RP-C205: Environmental Conditions And Environmental Loads.* Apr. 2007.

[67] Pan Fang et al. “Bending study of submarine power cables based on a repeated unit cell model”. en. In: *Engineering Structures* 293 (Oct. 2023), p. 116606. ISSN: 01410296. DOI: `10.1016/j.engstruct.2023.116606`. URL: `https://linkinghub.elsevier.com/retrieve/pii/S0141029623010210` (visited on 08/25/2024).

[68] . “DNV-RP-F019: On-bottom stability design of submarine pipelines”. In: (2021).

[69] Weidong Ruan et al. “Study on fatigue damage optimization mechanism of deepwater lazy wave risers based on multiple waveform serial arrangement”. en. In: *Ocean Engineering* 228 (May 2021), p. 108926. ISSN: 00298018. DOI: `10.1016/j.oceaneng.2021.108926`. URL: `https://linkinghub.elsevier.com/retrieve/pii/S0029801821003619` (visited on 05/22/2024).

[70] Anja Schnepf et al. “Numerical Investigations on Suspended Power Cable Configurations for Floating Offshore Wind Turbines in Deep Water Powering an FPSO”. en. In: *Journal of Offshore Mechanics and Arctic Engineering* 145.3 (June 2023), p. 030904. ISSN: 0892-7219, 1528-896X. DOI: `10.1115/1.4057006`. URL: `https://asmedigitalcollection.asme.org/offshoremechanics/article/145/3/030904/1159794/Numerical-Investigations-on-Suspended-Power-Cable` (visited on 05/22/2024).

[71] Avinash Aninthaneni and Université de Liège > Master ing civ méc. (EMSHIP+). “Optimisation of offshore wind floater from dynamic cable and mooring perspective”. en. In: (Sept. 2021). URL: `https://matheo.uliege.be/handle/2268.2/13300` (visited on 05/22/2024).

[72] Laksri Jayathilake. “Parametrization of Steel Lazy Wave Riser Configuration for Fatigue Considerations at the Touch Down Point”. eng. MA thesis. uis, 2022. URL: `https://uis.brage.unit.no/uis-xmlui/handle/11250/3032568` (visited on 08/23/2024).

[73] M Lane et al. “Bend stiffeners for flexible risers”. Houstoon, Texas, United States. In: *In Proceedings of the Conference on Offshore technology* (1995). URL: `https://www.osti.gov/biblio/128899`.

[74] Mehmet Emre Boru. “VIV Fatigue of dynamic power cables applied in offshore wind turbines”. eng. MA thesis. NTNU, 2021. URL: `https://ntnuopen.ntnu.no/ntnu-xmlui/handle/11250/2784217` (visited on 08/24/2024).

[75] D. Tsukinovsky, E. Zaretsky, and I. Rutkevich. “Material Behavior in Plane Polyurethane-Polyurethane Impact with Velocities from 10 to 400 m/sec”. en. In: *Journal de Physique IV Proceedings* 07.C3 (1997), p. C3. DOI: `10.1051/jp4:1997359`. URL: `https://hal.science/jpa-00255516` (visited on 08/24/2024).

[76] Manuel U.T. Rentschler, Frank Adam, and Paulo Chainho. “Design optimization of dynamic inter-array cable systems for floating offshore wind turbines”. en. In: *Renewable and Sustainable Energy Reviews* 111 (Sept. 2019), pp. 622–635. ISSN: 13640321. DOI: `10.1016/j.rser.2019.05.024`. URL: `https://linkinghub.elsevier.com/retrieve/pii/S1364032119303375` (visited on 11/21/2023).

[77] *Ovun | Buoyancy & Plastic Moulding*. en-US. Nov. 2017. URL: `https://ovun.com/` (visited on 07/15/2024).

[78] Anja Schnepf et al. “Dynamic Power Cable Configuration Design for Floating Offshore Wind Turbines Using Gradient-Based Optimization”. In: *Volume 8: Ocean Renewable Energy*. Melbourne, Australia: American Society of Mechanical Engineers, June 2023, V008T09A037. ISBN: 9780791886908. DOI: `10.1115/OMAE2023-102788`. URL: `https://asmedigitalcollection.asme.org/OMAE/proceedings/OMAE2023/86908/V008T09A037/1167390` (visited on 07/15/2024).

[79] Anja Schnepf et al. “Feasibility study on suspended inter-array power cables between two spar-type offshore wind turbines”. en. In: *Ocean Engineering* 277 (June 2023), p. 114215. ISSN: 00298018. DOI: `10.1016/j.oceaneng.2023.114215`. URL: `https://linkinghub.elsevier.com/retrieve/pii/S0029801823005991` (visited on 07/15/2024).

[80] Ahmad Izwan. “Optimisation of Suspended Inter-array Power Cable Configurations for Floating Offshore Wind Turbines”. eng. MA thesis. uis, 2022. URL: `https://uis.brage.unit.no/uis-xmlui/handle/11250/3022354` (visited on 07/15/2024).

[81] Matthias Brommundt et al. “Mooring System Optimization for Floating Wind Turbines using Frequency Domain Analysis”. en. In: *Energy Procedia* 24 (2012), pp. 289–296. ISSN: 18766102. DOI: `10.1016/j.egypro.2012.06.111`. URL: `https://linkinghub.elsevier.com/retrieve/pii/S1876610212011514` (visited on 08/27/2024).

[82] *Vattenfall In-house*.

[83] Dunja Stanisic et al. “Evaluation of Conventional Methods of Establishing Extreme Mooring Design Loads”. In: *Volume 3A: Structures, Safety and Reliability*. Trondheim, Norway: American Society of Mechanical Engineers, June 2017, V03AT02A017. ISBN: 9780791857656. DOI: `10.1115/OMAE2017-61243`. URL: `https://asmedigitalcollection.asme.org/OMAE/proceedings/OMAE2017/57656/Trondheim,%20Norway/280852` (visited on 10/11/2024).

[84] TKI Offshor Wind and TKI New Gas. *North Sea Energy Technical assessment of Hydrogen transport, compression, processing offshore*. 2020.

[85] *OrcaFlex example files - simulation files & guidance documents*. en-GB. URL: `https://www.orcina.com/resources/examples/` (visited on 08/26/2024).

[86] Dapeng Zhang et al. "Dynamic analysis of the subsea production system with lazy-wave risers attached to FPSO". en. In: *PLOS ONE* 18.9 (Sept. 2023). Ed. by Salar Farahmand-Tabar, e0291603. ISSN: 1932-6203. DOI: `10.1371/journal.pone.0291603`. URL: `https://dx.plos.org/10.1371/journal.pone.0291603` (visited on 05/30/2024).

[87] Chul-hee Jo, Do-youb Kim, and Yu-ho Rho. "A Comparison of Coupled and Uncoupled Dynamic Analysis for the Flexible Riser in Shallow Water". In: *Volume 4B: Pipeline and Riser Technology*. Nantes, France: American Society of Mechanical Engineers, June 2013, V04BT04A020. ISBN: 9780791855379. DOI: `10.1115/OMAE2013-11035`. URL: `https://asmedigitalcollection.asme.org/OMAE/proceedings/OMAE2013/55379/Nantes,%20France/270644` (visited on 12/16/2023).

[88] Shun-Han Yang et al. "A comparison of coupled and de-coupled simulation procedures for the fatigue analysis of wave energy converter mooring lines". en. In: *Ocean Engineering* 117 (May 2016), pp. 332–345. ISSN: 00298018. DOI: `10.1016/j.oceaneng.2016.03.018`. URL: `https://linkinghub.elsevier.com/retrieve/pii/S0029801816300075` (visited on 12/16/2023).

[89] Shan Gao et al. "Dynamic Responses for WindFloat Floating Offshore Wind Turbine at Intermediate Water Depth Based on Local Conditions in China". en. In: *Journal of Marine Science and Engineering* 9.10 (Oct. 2021), p. 1093. ISSN: 2077-1312. DOI: `10.3390/jmse9101093`. URL: `https://www.mdpi.com/2077-1312/9/10/1093` (visited on 11/28/2023).

[90] . "DNV-RP-C205: Environmental Conditions and Environmental Loads". en. In: (Apr. 2014).

[91] DNV-GL. *DNVGL-ST-F201: Dynamic risers*. Jan. 2018.

[92] DNV-GL. *DNV-OS-J103: Design of Floating Wind Turbine Structures*. en. June 2013. (Visited on 11/08/2023).

[93] G. Benassai et al. "Ultimate and accidental limit state design for mooring systems of floating offshore wind turbines". en. In: *Ocean Engineering* 92 (Dec. 2014), pp. 64–74. ISSN: 00298018. DOI: `10.1016/j.oceaneng.2014.09.036`. URL: `https://linkinghub.elsevier.com/retrieve/pii/S0029801814003692` (visited on 08/20/2024).

[94] "Development of an Integrated Extreme Wind, Wave, Current, and Water Level Climatology to Support Standards-Based Design of Offshore Wind Projects". In: *IEC 61400-3 Table 1 Design Load Cases (DLCs)* ().

[95] Clemens Hübler, Cristian G. Gebhardt, and Raimund Rolfes. "Assessment of a standard ULS design procedure for offshore wind turbine sub-structures". In: *Journal of Physics: Conference Series* 1104 (Oct. 2018), p. 012013. ISSN: 1742-6588, 1742-6596. DOI: `10.1088/1742-6596/1104/1/012013`. URL: `https://iopscience.iop.org/article/10.1088/1742-6596/1104/1/012013` (visited on 08/20/2024).

[96] DNV-GL. *DNV-GL: Metocean Characterization Recommended Practices for U.S. Offshore Wind Energy*. Aug. 2018.

[97] Alexey Ozorishin. "FSO concept for shallow waters in the Vietnam offshore oilfield - block Hanoi trough - 02". eng. MA thesis. University of Stavanger, Norway, 2012. URL: `https://uis.brage.unit.no/uis-xmlui/handle/11250/182918` (visited on 08/23/2024).

[98] Jonathan A. Tawn. "An extreme-value theory model for dependent observations". en. In: *Journal of Hydrology* 101.1-4 (June 1988), pp. 227–250. ISSN: 00221694. DOI: `10.1016/0022-1694(88)90037-6`. URL: `https://linkinghub.elsevier.com/retrieve/pii/0022169488900376` (visited on 08/24/2024).

[99] Nils S□dahl and Torfinn Ottesen. "Bend Stiffener Design for Umbilicals". In: *Volume 4: Pipeline and Riser Technology*. Rotterdam, The Netherlands: ASMEDC, Jan. 2011, pp. 449–460. ISBN: 9780791844366. DOI: `10.1115/OMAE2011-49461`. URL: `https://asmedigitalcollection.asme.org/OMAE/proceedings/OMAE2011/44366/449/357467` (visited on 12/15/2023).

[100] Tim Bunnik and Jule Scharnke. "Statistical Variation Of The 3-Hour Maximum Crest Height in a Survival Sea State". In: *Volume 7: CFD and FSI*. Hamburg, Germany: American Society of Mechanical Engineers, June 2022, V007T08A007. ISBN: 9780791885925. DOI: `10.1115/OMAE2022-79045`. URL: `https://asmedigitalcollection.asme.org/OMAE/proceedings/OMAE2022/85925/V007T08A007/1148020` (visited on 08/19/2024).

[101] Elzbieta M. Bitner-Gregersen et al. “Sea state conditions for marine structures’ analysis and model tests”. en. In: *Ocean Engineering* 119 (June 2016), pp. 309–322. ISSN: 00298018. DOI: `10.1016/j.oceaneng.2016.03.024`. URL: `https://linkinghub.elsevier.com/retrieve/pii/S0029801816300105` (visited on 08/19/2024).

[102] Izwan Bin Ahmad, Anja Schnepf, and Muk Chen Ong. “An optimisation methodology for suspended inter-array power cable configurations between two floating offshore wind turbines”. en. In: *Ocean Engineering* 278 (June 2023), p. 114406. ISSN: 00298018. DOI: `10.1016/j.oceaneng.2023.114406`. URL: `https://linkinghub.elsevier.com/retrieve/pii/S0029801823007904` (visited on 11/23/2023).

[103] B Mutlu Sumer and Jørgen Fredsøe. *Hydrodynamics Around Cylindrical Structures*. en. Revised. Vol. 26. Advanced Series on Ocean Engineering. WORLD SCIENTIFIC, Sept. 2006. ISBN: 9789812700391 9789812772770. DOI: `10.1142/6248`. URL: `https://www.worldscientific.com/worldscibooks/10.1142/6248` (visited on 07/16/2024).

[104] API. “API 17K: Specification for Bonded Flexible Pipe”. en. In: *Technical report, American Petroleum Institue (API)* (Mar. 2002), p. 72.

[105] Anja Schnepf et al. “Suspended Power Cable Configurations for Floating Offshore Wind Turbines in Deep Water Powering an FPSO”. In: Oct. 2022. DOI: `10.1115/OMAE2022-80071`.

[106] Upul Shanthilal Fernando et al. “Experimental Evaluation of the Metal-to-Metal Seal Design for High-Pressure Flexible Pipes”. en. In: *All Days*. Houston, Texas, USA: OTC, Apr. 2012, OTC–23110–MS. DOI: `10.4043/23110-MS`. URL: `https://onepetro.org/OTCONF/proceedings/12OTC/All-12OTC/Houston,%20Texas,%20USA/37067` (visited on 11/02/2023).

[107] Seyed Mohammad Hossein Sharifi, Nima Pirali, and Babak Najafi. “Investigation of Available Configurations for Flexible Risers in Shallow Water”. en. In: 14 (2020).

A

Technology Flexible Pipes

A.1. Comparison pipes and configurations

Table A.1: Limitations and applications of bonded [104] and non-bonded [31] flexible pipes

Properties	**Bonded flexible pipes**	**Non-bonded flexible pipes**	**Remark**
		Limitations	
Length	12 - 100m	Several km	Non-bonded pipes usually employed for long lengths
Internal fluid	Low pressure/ low temperature	High pressure/ temperature max 120 °C	Non-bonded pipes preferred with gas, unstable fluids or high temperatures
Internal diameter	Max 24 inches	Max 19 inches	Bore bonded pipes constructed in 12 m parts
Bending flexibility	Excellent	Good	Bonded pipes preferred in high bending applications
		Applications	
Flowline	Usually not	Yes	Located subsea; from well to manifold
Subsea jumper	Usually not	Yes	Short line connecting subsea units e.g. individual wells
Flexible riser	Some	Yes	Lines connecting a subsea station to a floating platform
Offloading Oil	Yes	Some	Mostly used in combinations with diameters higher than the limit of bonded pipes
Jumpers	Yes	Yes	Drilling, turret jumpers FPSO, topside jumpers TLPs and long jumpers connection platforms

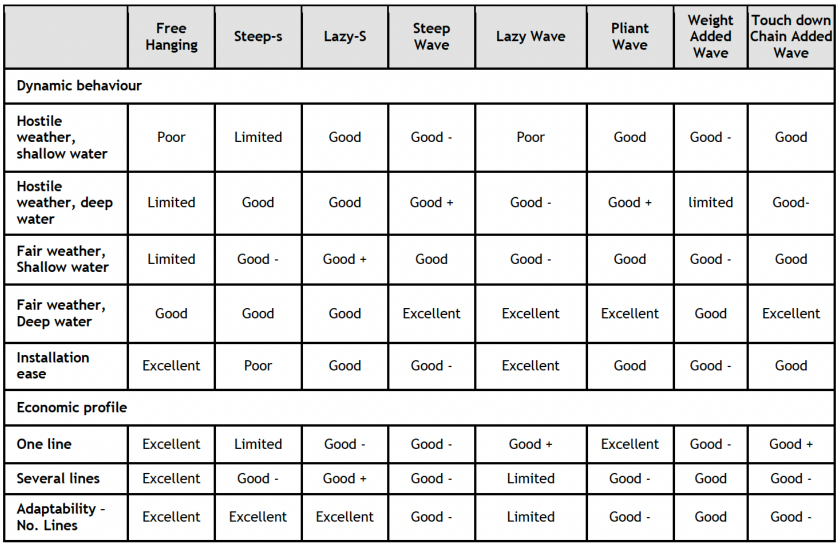

	Free Hanging	Steep-s	Lazy-S	Steep Wave	Lazy Wave	Pliant Wave	Weight Added Wave	Touch down Chain Added Wave
Dynamic behaviour								
Hostile weather, shallow water	Poor	Limited	Good	Good -	Poor	Good	Good -	Good
Hostile weather, deep water	Limited	Good	Good	Good +	Good -	Good +	limited	Good-
Fair weather, Shallow water	Limited	Good -	Good +	Good	Good -	Good	Good -	Good
Fair weather, Deep water	Good	Good	Good	Excellent	Excellent	Excellent	Good	Excellent
Installation ease	Excellent	Poor	Good	Good -	Excellent	Good	Good -	Good
Economic profile								
One line	Excellent	Limited	Good -	Good -	Good +	Excellent	Good -	Good +
Several lines	Excellent	Good -	Good +	Good -	Limited	Good -	Good	Good -
Adaptability - No. Lines	Excellent	Excellent	Excellent	Good -	Limited	Good -	Good	Good -

Figure A.1: Selection matrix for riser configuration based on the study of [35]

A.2. Ancillary components

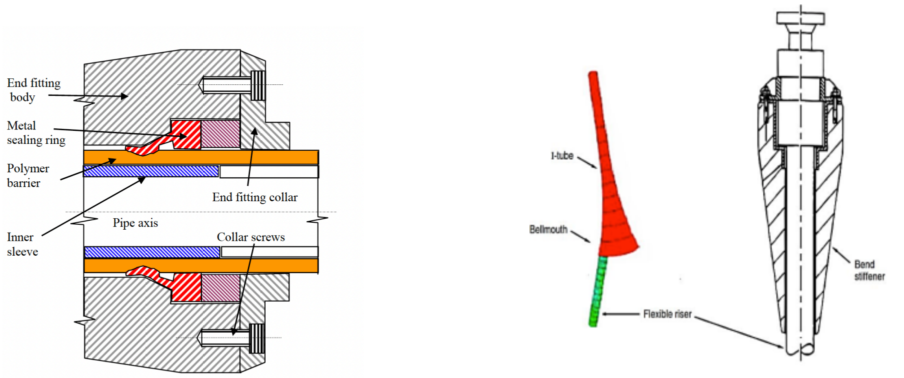

(a) End-fitting [106]

(b) Bend stiffener (left) and bellmouth (right) [107]

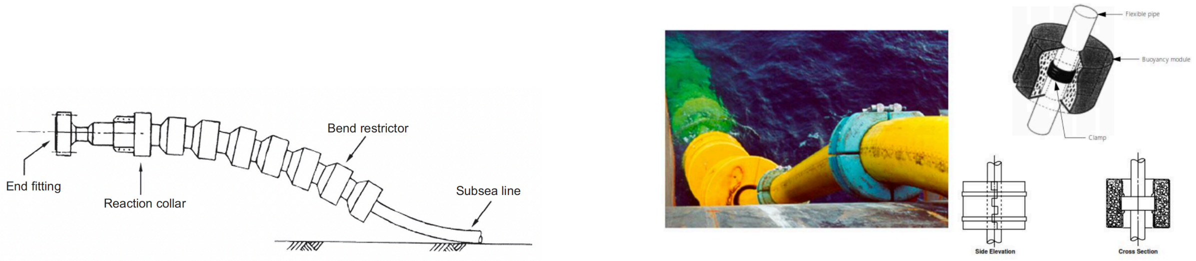

(c) Bend restrictor [104]

(d) Buoyancy modules [35]

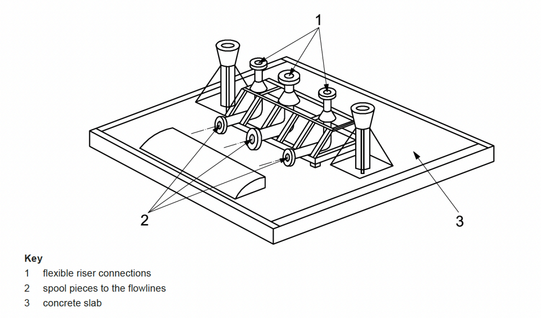

(e) Riser base [41]

Figure A.2: Main ancillaries

B

Pipe Design Details

B.1. Decision-making hydrodynamic coefficients pipe

The hydrodynamic coefficients for slender structures are determined following the guidelines in [66]. The hydrodynamic loads are characterized by the drag and added mass coefficients, which depend on the Reynolds number, Keulegan-Carpenter number, and surface roughness. These are defined by the following equations:

$$Re = \frac{vD}{\nu} \tag{B.1}$$

$$K_c = \frac{v_m T}{d} \tag{B.2}$$

$$k/D = \frac{k}{D} \tag{B.3}$$

Where v is the flow velocity (m/s), D is the outer diameter of the structure (m), ν is the kinematic viscosity (m^2/s), T is the wave period (s), and k is the surface roughness height (m).
For this analysis, the surface roughness is taken as 5×10^{-5} m (uncoated steel), resulting in a roughness ratio of $k/D = 3 \times 10^{-5}$. Assuming a water temperature of 5°C, the kinematic viscosity is $1.56 \times 10^{-6}\ m^2/s$ [66]. With a 100-year average current speed [35] of 0.46 m/s, the Reynolds number is calculated as 4.4×10^4. The corresponding hydrodynamic drag coefficient C_D is approximately 1.05 (see figre B.1).

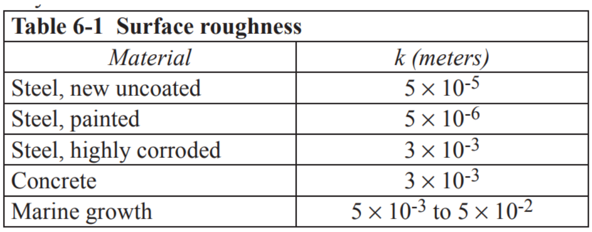

Table 6-1 Surface roughness

Material	*k (meters)*
Steel, new uncoated	5×10^{-5}
Steel, painted	5×10^{-6}
Steel, highly corroded	3×10^{-3}
Concrete	3×10^{-3}
Marine growth	5×10^{-3} to 5×10^{-2}

(a) Surface roughness for drag coefficient determination

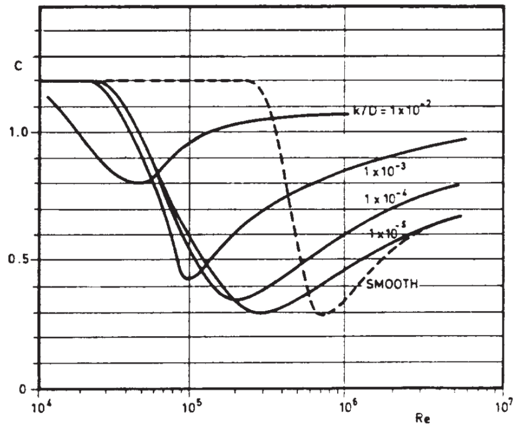

(b) Drag coefficient for circular structures in steady flow [66]

Figure B.1: Determination of drag coefficient

The maximum wave height varies between 9.1 m and 12.6 m in a severe sea state (SSS), leading to a Keulegan-Carpenter number calculated as $K_c = \frac{\pi H}{D}$ within the wave zone. This gives a range of K_c from 215 to 298, indicating a large value. For high K_c values, the added mass coefficient C_M is estimated to be 1.6 for smooth cylinders, resulting in an added mass coefficient $C_A = C_M - 1 = 0.6$, as shown in Fig. B.2.

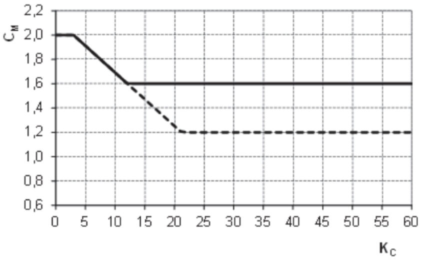

Figure B.2: Added mass coefficient as a function of the K_c number. Solid line: smooth cylinder; dashed line: rough cylinder [66].

B.2. Equations hydrodynamic coefficients buoyancy section

$$C_{Dn,e} = C_{Dn,BM}\frac{OD_{BM}L_{BM}}{OD_{pipe}d_{B}M} + C_{Dn,pipe}\frac{d_{BM} - LBM}{d_{BM}} \tag{B.4}$$

$$C_{Da,e} = \frac{1}{d_{BM}OD_{BMe}}\left(\frac{C_{Da,1}}{4}(OD_{BM}^2 - OD_{pipe}^2) + C_{Da,2}OD_{BM}L_{BM} + C_{Da,pipe}OD_{BMe}(d_{BM} - L_{BM})\right) \tag{B.5}$$

B.3. Capacity of hydrogen production

The hydrogen production is based on the output electrolyzer requirements of a design pressure and temperature of 40 barg and 50 °C. The energy content of hydrogen is 55 kWh/kg, and the full capacity of the wind turbine is 15 MW. The energy efficiency is around 60 to 70% [82], and the internal hydrogen velocity is estimated at 15 m/s [84].

To determine the density of hydrogen, the ideal gas law provides a reasonable approximation. High temperatures favor ideal gas behavior; however, high pressure results in more compressed behavior and intermolecular forces. While the ideal gas law is generally a reasonable approximation under these conditions, precise calculations, such as those needed for safety analysis, benefit from considering deviations from ideal gas behavior. For greater accuracy, using compressibility factors is beneficial to adjust for molecular interactions. The density, determined by the ideal gas constant, can be estimated with the following equation:

$$\rho_{\text{hydrogen}} = \frac{p \cdot M}{R \cdot T} = \frac{4 \times 10^6 \times 0.002016}{8.314 \times 323.15} = 3.00\,\text{kg/m}^3 \tag{B.6}$$

where p is the pressure in Pa, M the molar mass in kg/mol, R the gas constant in $\text{m}^3 \cdot \text{Pa}/(\text{K} \cdot \text{mol})$, and T is the temperature in K.

When the turbine and electrolyzer run at full capacity, the hydrogen production mass flow rate can be estimated with:

$$\dot{m}_{\text{H}_2} = \frac{P \times \eta}{E} = \frac{15 \times 0.60}{55} = 0.04545\,\text{kg/s} \tag{B.7}$$

where P is the power output in MW, η the efficiency factor and E is the energy content of hydrogen in kWh/kg.

Using the derived density and the mass flow rate, the total volumetric flow rate of hydrogen can be calculated using the following equation:

$$Q_{tot} = \frac{\dot{m}_{\mathrm{H_2}}}{\rho_{\text{hydrogen}}} = \frac{0.04545}{3.00} = 0.01515\,\mathrm{m}^3/\mathrm{s} \tag{B.8}$$

Capacity based on maximum conversion possibility: If a single pipe were used to transport the hydrogen at maximum capacity, the inner diameter would be:

$$ID_{single} = 2\sqrt{\frac{\frac{Q_{tot}}{v}}{\pi}} = 2\sqrt{\frac{\frac{0.01515}{15}}{\pi}} = 0.0359\,\mathrm{m} = 1.4\,\text{inches} \tag{B.9}$$

where v is the internal flow speed in m/s.

Capacity based on provided pip:
If the pipe provided by NOV is used, the volumetric flow rate for is calculated with:

$$Q_{pipe} = v \times \pi \times \left(\frac{ID}{2}\right)^2 = 15 \times \pi \times (\frac{0.1016}{2}^{2}) = 0.1216\,\mathrm{m}^3/\mathrm{s} \tag{B.10}$$

The number of pipes needed to transport all hydrogen with the hypothetical pipe requires is as follows:

$$\mathrm{N} = \frac{Q_{tot}}{Q_{pipe}} = \frac{0.01515}{0.1216} = 0.142$$

B.4. Design flowchart

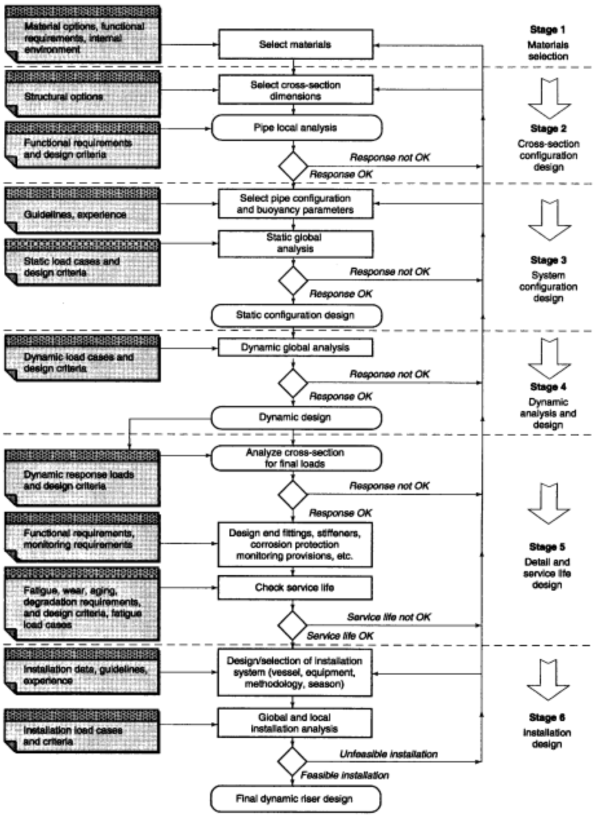

Figure B.3: Flowchart application for dynamic design purpose of un-bonded flexible pipes [26]

B.5. Information on beam theory

The beam Theory, particularly the Euler-Bernoulli beam theory, is used to analyze the behavior of beam-like structures under various loads. This theory simplifies the analysis of bending and axial deformations by making several key assumptions, introducing also limitations:

- **Linear Elasticity:** The material of the beam behaves according to Hooke's Law, meaning that the deformations are proportional to the applied loads. This implies that the material remains within its elastic limit and does not experience plastic deformations. For materials undergoing large strains or yielding, this simplification may lead to inaccurate results.
- **Small Deformations:** The theory assumes that the deformations are small relative to the beam's length. This allows the linear approximation of deformations and neglects geometric non-linearities. For cases involving large deformations or complex loading conditions, geometric non-linearities can become more significant.
- **Plane Sections Remain Plane:** Cross-sections of the beam that are initially plane and perpendicular to the beam's axis remain plane and perpendicular after deformation. This means that there is no warping or twisting of the cross-sections.
- **Neglecting Shear Deformation:** For scenarios involving pure bending, shear deformation is not considered. This assumption is valid for slender beams where the length is significantly greater than the cross-sectional dimensions. However, this may not be accurate for short or thick beams where shear effects can be substantial.

Flexible pipes are complex structures consisting of multiple layers, each with its specific function. The structure of such pipes is far more complex than that of a simple homogeneous beam, yet Orcaflex simplifies this complexity using this theory. This simplification, while computationally efficient, introduces several limitations that must be understood to accurately interpret simulation results.

- **Homogeneous and Isotropic Material Properties:** Despite the pipe being composed of multiple layers, each with distinct materials and mechanical properties, the software assumes the pipe can be treated as a homogeneous and isotropic material. This means that the material properties are uniform throughout the structure and behave identically in all directions. This simplification ignores the interaction between layers (such as friction, potential gaps forming, or layer separation), leading to an oversimplified representation of the pipe's behavior, especially under bending or torsional loads.
- **Constant Cross-Section:** The software assumes that the cross-section of the pipe remains constant along its length, which neglects the complex interaction between the layers, particularly when they move relative to each other under bending. This can lead to inaccurate predictions of stress distribution, especially at the interfaces between layers where varying stiffness and strength would otherwise affect the structural response.
- **No Layer Separation:** In reality, the layers in a flexible pipe are not bonded, meaning they can move relative to each other. This movement can cause changes in the overall cross-sectional shape during bending, an effect not captured by the beam theory used in Orcaflex. Consequently, the theory does not accurately represent the potential sliding or separation of layers, which could impact the structural integrity of the pipe under certain conditions.
- **Inadequate Representation of Non-Linearities:** The complex loading conditions, including pressure, temperature variations, and dynamic forces such as waves or currents, can cause non-linear deformations in the pipe. Beam theory assumes linear elasticity and small deformations, which may not hold true under high stress or strain conditions, leading to inaccuracies in the predicted structural response. This is particularly important in the context of operational safety and design optimization.
- **Neglecting Shear and Warping Effects:** In reality, the cross-section of a flexible pipe may experience warping and shear deformation under load due to the complex layered structure. However, the beam theory assumes that plane sections remain plane, neglecting these effects. This limitation can result in underestimating the deformation

The simplifications made OF affect the accuracy of simulations in real-life scenarios. For example, the inability to accurately predict the behavior of each layer in a flexible pipe could lead to an underestimation of critical stresses, particularly in scenarios involving high internal pressures or complex loading patterns. This could impact the operational safety and reliability of the pipeline. Additionally, without accurately accounting for the complex interactions between layers, the design process may not fully optimize material usage or layer thicknesses, potentially leading to over-engineering or insufficient strength in certain areas. Finally, the beam theory simplifications might lead to discrepancies between the simulation results and actual pipe behavior in the field, especially under extreme conditions, resulting in less accurate predictions for fatigue life, failure points, and overall pipe performance.

B.6. RAO's of semi-submersible

Figure B.4: 6 DoF RAOs of semi-submersible in wave direction of 0, 60 and 90 degrees

B.7. Bend stiffener considerations

Table B.1: Maximum normalized curvature for all tested scenarios of BS

		Diameter (m)							
		0.3	**0.4**	**0.5**	**0.6**	**0.7**	**0.8**	**0.9**	**1.0**
Length (m)	**1**	0.82	0.56	0.63	0.69	0.73	0.76	0.78	0.80
	2	0.86	0.51	0.42	0.49	0.56	0.61	0.65	0.68
	3	0.89	0.55	0.33	0.35	0.42	0.47	0.52	0.57
	4	0.91	0.58	0.35	0.27	0.31	0.37	0.42	0.47
	5	0.93	0.60	0.37	0.24	0.24	0.29	0.34	0.39
	6	0.94	0.62	0.39	0.25	0.21	0.23	0.27	0.32
	7	0.95	0.63	0.41	0.27	0.19	0.19	0.23	0.27
	8	0.96	0.64	0.42	0.28	0.20	0.17	0.19	0.23
	9	0.96	0.65	0.43	0.29	0.21	0.16	0.17	0.19
	10	0.97	0.66	0.44	0.31	0.22	0.16	0.15	0.17

Table B.2: Position of maximum normalized curvature for all tested scenarios of BS (0% = base, 100% = tip)

	Diameter (m)							
Length (m)	**0.3**	**0.4**	**0.5**	**0.6**	**0.7**	**0.8**	**0.9**	**1.0**
1	0%	125%	125%	125%	125%	125%	125%	125%
2	0%	0%	113%	113%	113%	113%	113%	113%
3	0%	0%	38%	108%	108%	108%	108%	108%
4	0%	0%	0%	66%	106%	106%	106%	106%
5	0%	0%	0%	33%	81%	105%	105%	105%
6	0%	0%	0%	0%	61%	89%	104%	104%
7	0%	0%	0%	0%	35%	84%	104%	104%
8	0%	0%	0%	0%	76%	89%	103%	103%
9	0%	0%	0%	0%	0%	41%	85%	93%
10	0%	0%	0%	0%	0%	0%	82%	90%

B.8. Simulation parameters for convergence

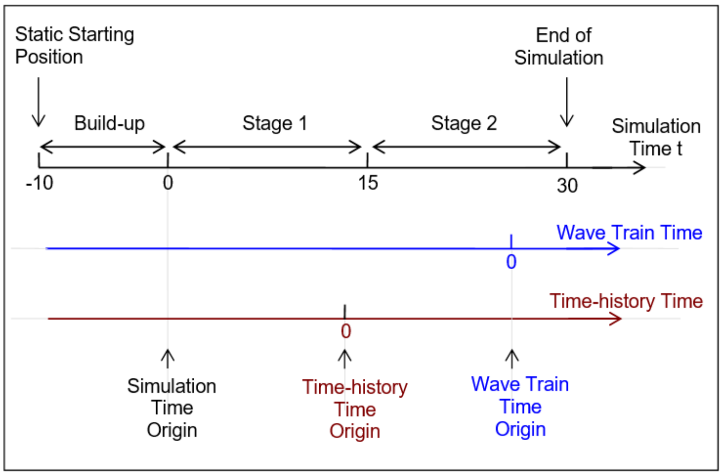

Figure B.5: Time and simulation stages of time domain dynamic analysis

Table B.3: Full data of convergence test values

Parameter	**unit**	**Test values**
Time step	s	[0.05, 0.1, 0.15, 0.2, 0.25, 0.3, 0.35, 0.4, 0.5, 0.6, 0.7, 0.8, 0.9, 1, 1.5, 2]
Target segment length	m	[0.2, 0.5, 1, 2, 3, 4, 5, 6, 7, 8, 9, 10]
Build-up time	s	[16, 32, 60, 120, 240, 360, 480, 600, 720, 840, 1000]
Simulation time	s	[120, 460, 600, 1200, 2400, 3600, 4800, 6000, 7200, 8400, 9600, 10800]

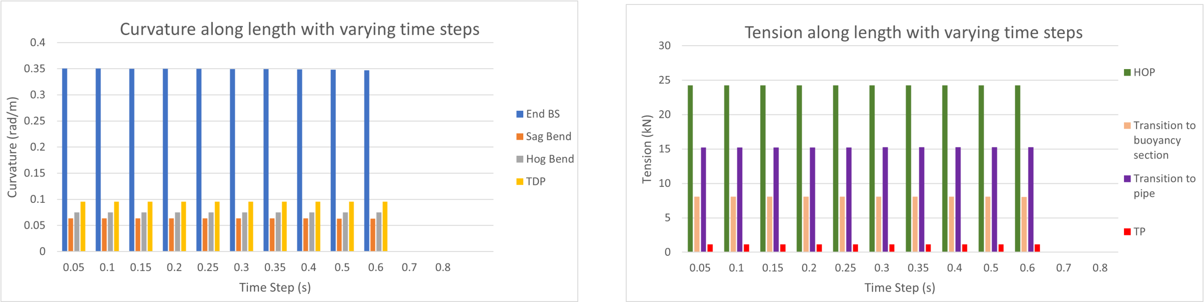

(a) Curvature effect **(b)** Tension effect

Figure B.6: Convergence: Time step

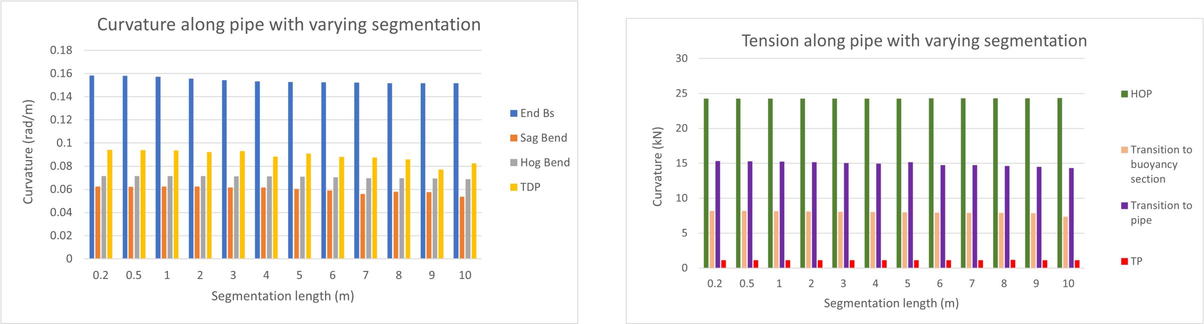

(a) Curvature effect **(b)** Tension effect

Figure B.7: Convergence: Target segment length

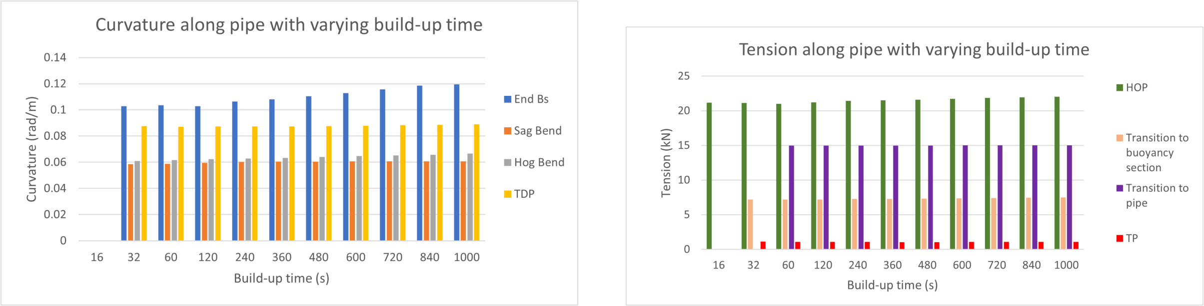

(a) Curvature effect **(b)** Tension effect

Figure B.8: Convergence: Build-up time

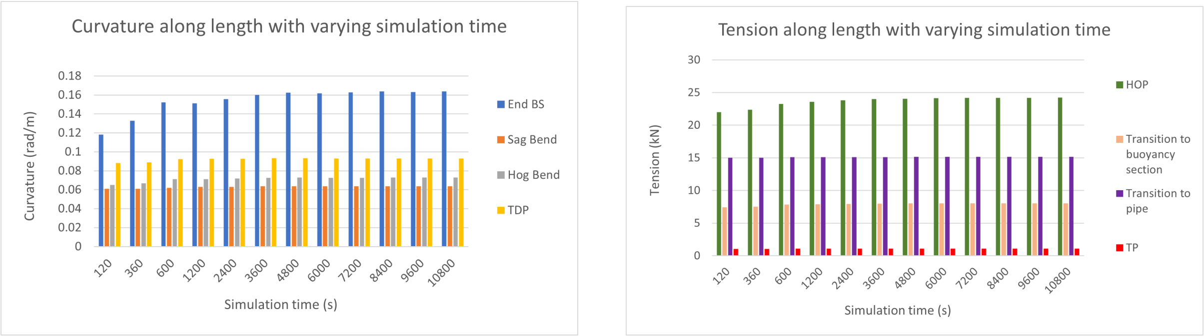

(a) Curvature effect **(b)** Tension effect

Figure B.9: Convergence: Build-up time

C

Scenarios for Parametric Set-Up

C.1. Test ratios

Table C.1: Parametric variable set-up in ratios

Parameter	Ratio	Test ratios
OD_{BM}	$\frac{OD_{BM}}{OD_{pipe}}$	[1.23, 1.39, 1.54, 1.7, 1.85, 2, 2.16, 2.31, 2.47, 2.62, 2.77, 2.93, 3.08, 3.24, 3.39, 3.55, 3.7, 3.85, 4.01, 4.16, 4.32, 4.47, 4.62, 4.78, 4.93, 5.09, 5.24, 5.39, 5.55, 5.7, 5.96, 6]
d_{BM}	$\frac{L_2}{d_{BM}}$	[126, 63, 42, 32, 25, 21, 18, 16, 14, 13, 11, 10]
L_1	$\frac{L_1}{L_{total}}$	[0.02, 0.04, 0.06, 0.079, 0.099, 0.119, 0.139, 0.159, 0.179, 0.198, 0.218, 0.238, 0.258, 0.278, 0.298, 0.317, 0.337, 0.357, 0.377, 0.397, 0.417, 0.437, 0.456, 0.476, 0.496, 0.516, 0.536, 0.556, 0.575, 0.595]
L_2	$\frac{L_2}{L_{total}}$	[0.02, 0.04, 0.06, 0.079, 0.099, 0.119, 0.139, 0.159, 0.179, 0.198, 0.218, 0.238, 0.258, 0.278, 0.298, 0.317, 0.337, 0.357, 0.377, 0.397, 0.417, 0.437, 0.456, 0.476, 0.496]
$L_{total}*$	$\frac{L_{total}}{h}$	[1.97, 2.02, 2.08, 2.13, 2.19, 2.24, 2.30, 2.36, 2.41, 2.47, 2.52, 2.58, 2.63, 2.69, 2.74, 2.8, 2.86, 2.91, 3.02, 3.08, 3.13, 3.19, 3.24, 3.3, 3.36, 3.41, 3.47, 3.52, 3.58, 3.63]
X_{TP}	$\frac{X_{TP}}{h}$	[1.28, 1.42, 1.56, 1.69, 1.83, 1.97, 2.11, 2.25, 2.39, 2.53, 2.67]
*L_3	$\frac{L_3}{L_{total}}$	[0.288, 0.308, 0.326, 0.344, 0.360, 0.376, 0.391, 0.406, 0.419, 0.432, 0.445, 0.457, 0.468, 0.479, 0.490, 0.500, 0.510, 0.519, 0.528, 0.537, 0.545, 0.553, 0.561, 0.568, 0.576, 0.583, 0.590, 0.596, 0.603, 0.609, 0.615]

C.2. Test values for 200m, 400m, and 600m depth

Table C.2: Full data of test values for 200m water depth

Parameter	**Ratio**	**Test values**
OD_{BM}	$\frac{OD_{BM}}{OD_{pipe}}$	[0.2, 0.225, 0.25, 0.275, 0.3, 0.325, 0.35, 0.375, 0.4, 0.425, 0.45, 0.475, 0.5, 0.525, 0.55, 0.575, 0.6, 0.625, 0.65, 0.675, 0.7, 0.725, 0.75, 0.775, 0.8, 0.825, 0.85, 0.875, 0.9, 0.925, 0.95, 0.975, 1]
d_{BM}	$\frac{L_2}{d_{BM}}$	[1, 2, 3, 4, 5, 6, 7, 8, 9, 10, 11, 12]
L_1	$\frac{L_1}{L_{total}}$	[10, 20, 30, 40, 50, 60, 70, 80, 90, 100, 110, 120, 130, 140, 150, 160, 170, 180, 190, 200]
L_2	$\frac{L_2}{L_{total}}$	[10, 20, 30, 40, 50, 60, 70, 80, 90, 100, 110, 120, 130, 140, 150, 160, 170, 180, 190, 200, 210, 220, 230, 240, 250, 260, 270, 280, 290, 300]
$L_{total}*$	$\frac{L_{total}}{h}$	[354, 364, 374, 384, 394, 404, 414, 424, 434, 444, 454, 464, 474, 484, 494, 504, 514, 524, 534, 544, 554, 564, 574, 584, 594, 604, 614, 624, 634, 644, 654]
X_{TP}	$\frac{X_{TP}}{h}$	[230, 255, 280, 305, 330, 355, 380, 405, 430, 455, 480]
*L_3	$\frac{L_3}{L_{total}}$	[78, 88, 98, 108, 118, 128, 138, 148, 158, 168, 178, 188, 198, 208, 218, 228, 238, 248, 258, 268, 278, 288, 298, 308, 318, 328, 338, 348, 358, 368]

Table C.3: Full data of test values for 400m and 600m water depth

Parameter	Ratio	Test values
		Water depth = 400m
OD_{BM}	$\frac{OD_{BM}}{OD_{pipe}}$	[0.2, 0.225, 0.25, 0.275, 0.3, 0.325, 0.35, 0.375, 0.4, 0.425, 0.45, 0.475, 0.5, 0.525, 0.55, 0.575, 0.6, 0.625, 0.65, 0.675, 0.7, 0.725, 0.75, 0.775, 0.8, 0.825, 0.85, 0.875, 0.9, 0.925, 0.95, 0.975, 1]
d_{BM}	$\frac{L_2}{d_{BM}}$	[2.1, 4.2, 6.3, 8.4, 10.6, 12.7, 14.8, 16.9, 19.0, 21.1, 23.2, 26.6]
L_1	$\frac{L_1}{L_{total}}$	[21.1, 42.2, 63.3, 84.4, 105.6, 126.7, 147.8, 168.9, 190.0, 211.1, 232.2, 253.3, 274.4, 295.6, 316.7, 337.8, 358.9, 380.0, 401.1, 422.2, 443.3, 464.4, 485.6, 506.7, 527.8, 548.9, 570.0, 591.1, 612.2, 633.3]
L_2	$\frac{L_2}{L_{total}}$	[21.3, 42.2, 63.3, 84.4, 105.6, 126.7, 147.8, 168.9, 190.0, 211.1, 232.2, 253.3, 274.4, 295.6, 316.7, 337.8, 358.9, 380.0, 401.1, 422.2]
$L_{total}*$	$\frac{L_{total}}{h}$	[747.3, 768.4, 789.6, 810.7, 831.8, 852.9, 874.0, 895.1, 916.2, 937.3, 958.4, 979.6, 1000.7, 1021.8, 1042.9, 1064.0, 1085.1, 1106.2, 1127.3, 1148.4, 1169.6, 1190.7, 1211.8, 1232.9, 1254.0, 1275.1, 1296.2, 1317.3, 1338.4, 1359.6, 1380.7]
X_{TP}	$\frac{X_{TP}}{h}$	[485.6, 538.3, 591.1, 643.9, 696.7, 749.4, 802.2, 855.0, 907.8, 960.6, 1013.3]
		Water depth = 600m
OD_{BM}	$\frac{OD_{BM}}{OD_{pipe}}$	[0.2, 0.225, 0.25, 0.275, 0.3, 0.325, 0.35, 0.375, 0.4, 0.425, 0.45, 0.475, 0.5, 0.525, 0.55, 0.575, 0.6, 0.625, 0.65, 0.675, 0.7, 0.725, 0.75, 0.775, 0.8, 0.825, 0.85, 0.875, 0.9, 0.925, 0.95, 0.975, 1]
d_{BM}	$\frac{L_2}{d_{BM}}$	[3.2, 6.4, 9.7, 12.9, 16.1, 19.3, 22.6, 25.8, 29.0, 32.2, 35.4, 40.6]
L_1	$\frac{L_1}{L_{total}}$	[32.2, 64.4, 96.7, 128.9, 161.1, 193.3, 225.6, 257.8, 290.0, 322.2, 354.4, 386.7, 418.9, 451.1, 483.3, 515.6, 547.8, 580.0, 612.2, 644.4, 676.7, 708.9, 741.1, 773.3, 805.6, 837.8, 870.0, 902.2, 934.4, 966.7]
L_2	$\frac{L_2}{L_{total}}$	[32.5, 64.4, 96.7, 128.9, 161.1, 193.3, 225.6, 257.8, 290.0, 322.2, 354.4, 386.7, 418.9, 451.1, 483.3, 515.6, 547.8, 580.0, 612.2, 644.4]
$L_{total}*$	$\frac{L_{total}}{h}$	[1140.7, 1172.9, 1205.1, 1237.3, 1269.6, 1301.8, 1334.0, 1366.2, 1398.4, 1430.7, 1462.9, 1495.1, 1527.3, 1559.6, 1591.8, 1624.0, 1656.2, 1688.4, 1720.7, 1752.9, 1785.1, 1817.3, 1849.6, 1881.8, 1914.0, 1946.2, 1978.4, 2010.7, 2042.9, 2075.1, 2107.3]
X_{TP}	$\frac{X_{TP}}{h}$	[741.1, 821.7, 902.2, 982.8, 1063.3, 1143.9, 1224.4, 1305.0, 1385.6, 1466.1, 1546.7]

D

Additional Results Parametrics

D.1. Static and dynamic contribution per parameter

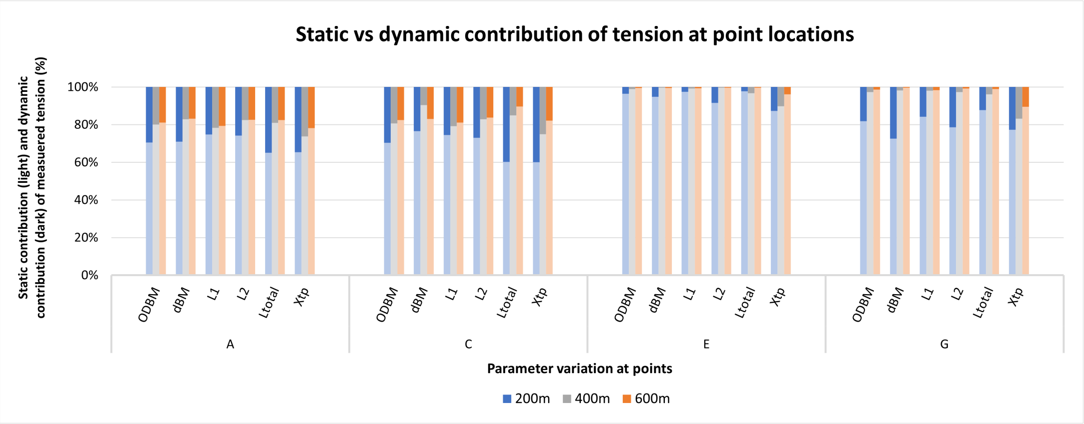

Figure D.1: Averaged static and dynamic contribution for tension

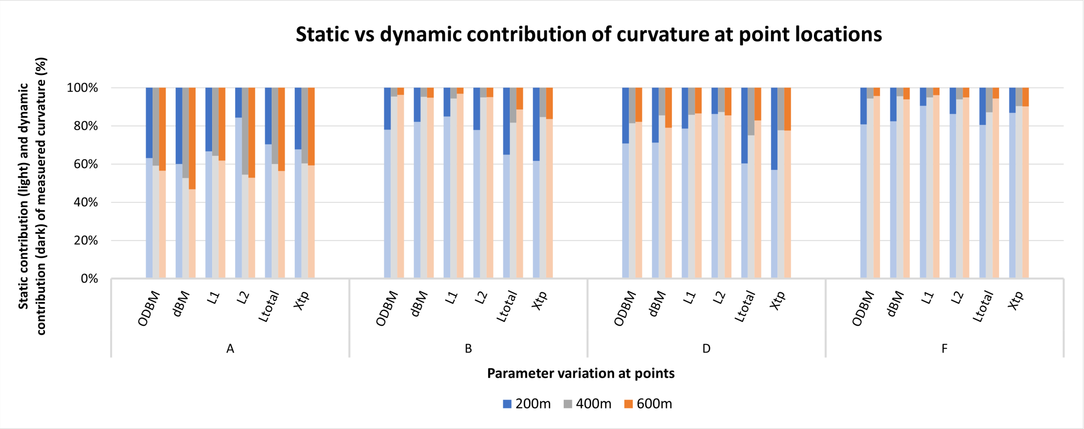

Figure D.2: Averaged static and dynamic contribution for curvature

D.2. Evaluation criteria for water depth 200m, 400m, 600m

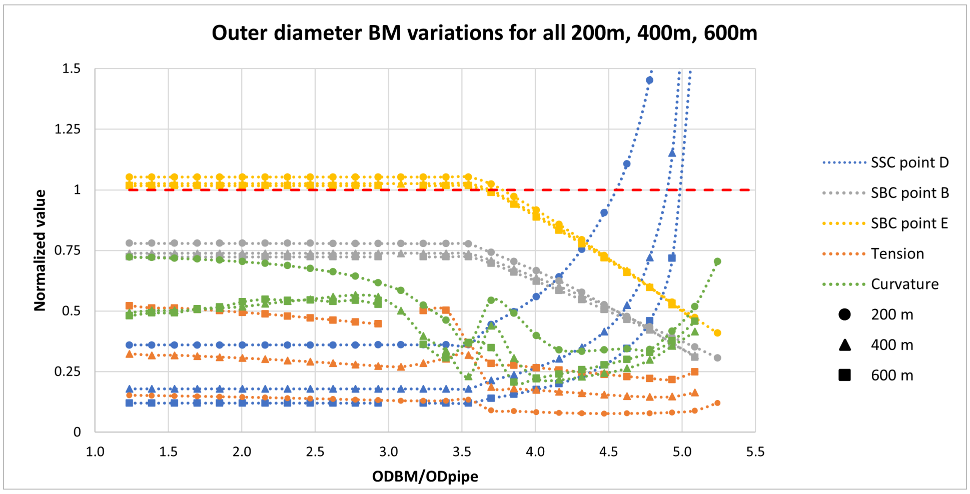

Figure D.3: Normalized evaluation criteria for all tested scenarios of OD_{BM} variation at 200m, 400m, 600m water depth

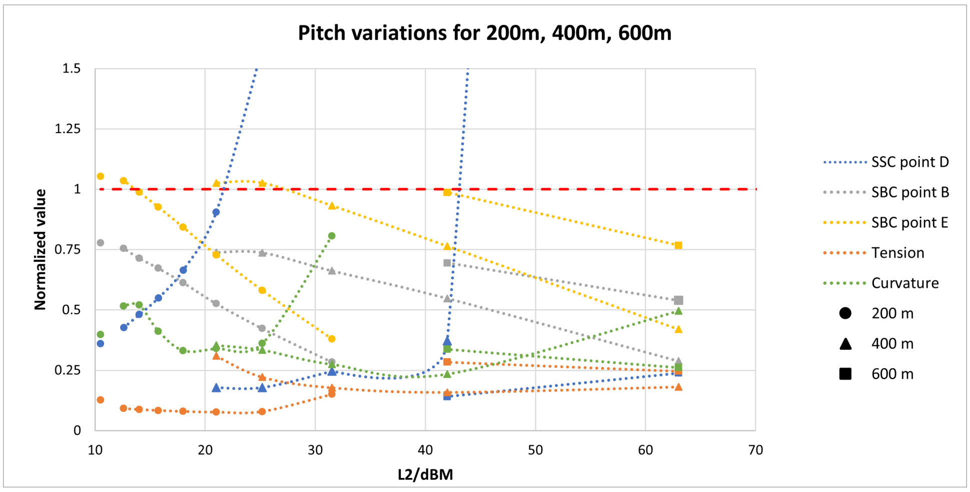

Figure D.4: Normalized evaluation criteria for all tested scenarios of d_{BM} variation at 200m, 400m, 600m water depth

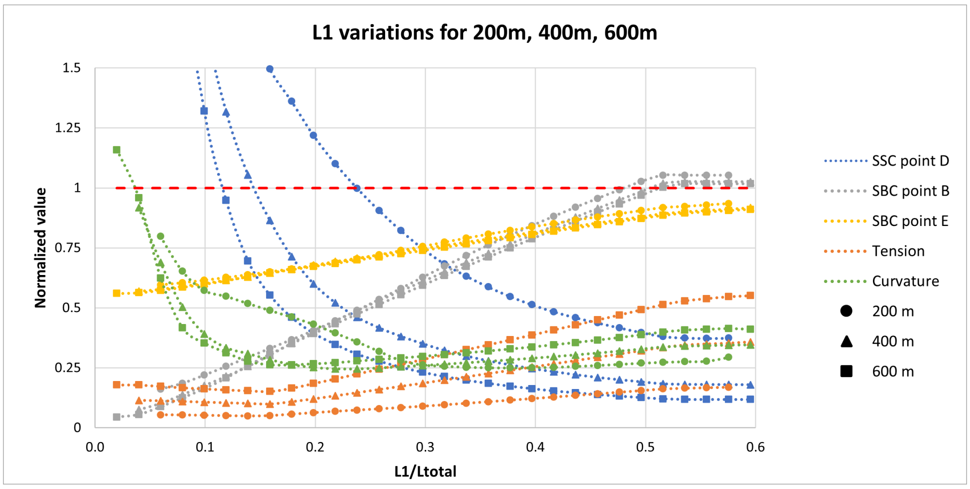

Figure D.5: Normalized evaluation criteria for all tested scenarios of L_1 variation at 200m, 400m, 600m water depth

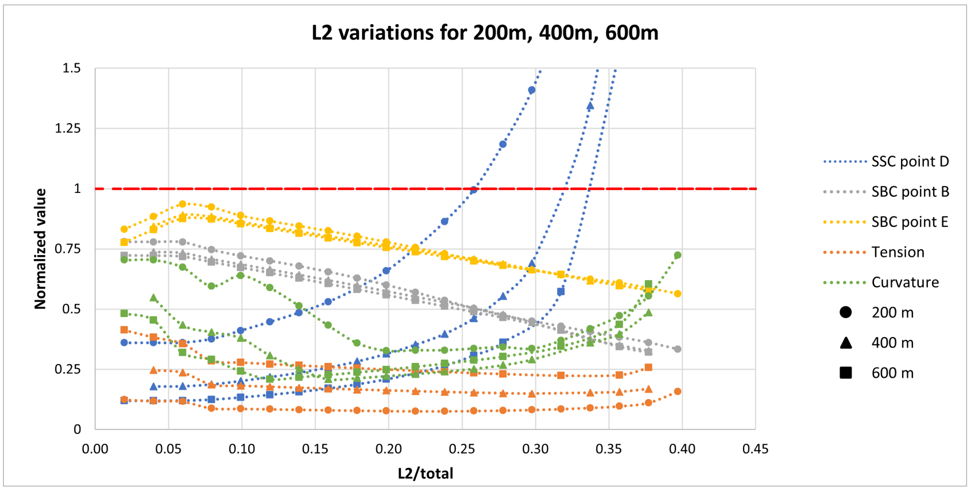

Figure D.6: Normalized evaluation criteria for all tested scenarios of L_2 variation at 200m, 400m, 600m water depth

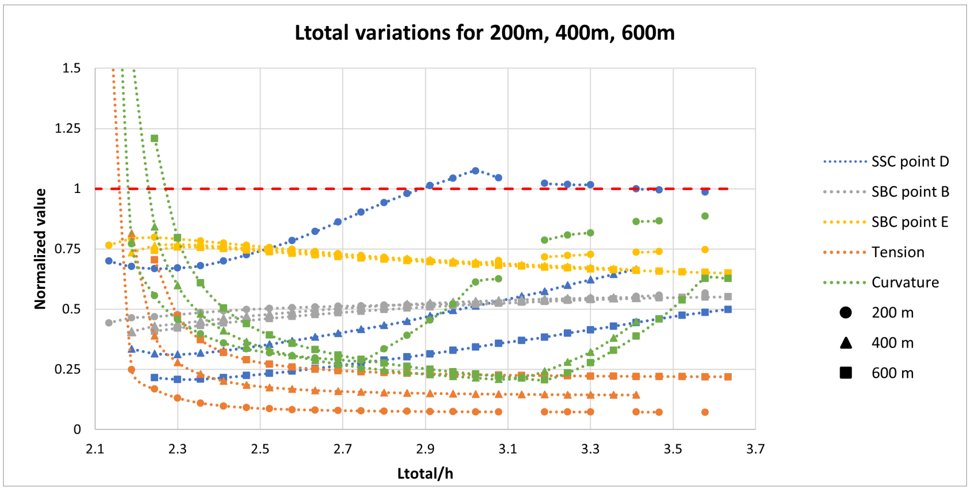

Figure D.7: Normalized evaluation criteria for all tested scenarios of L_{total} variation at 200m, 400m, 600m water depth

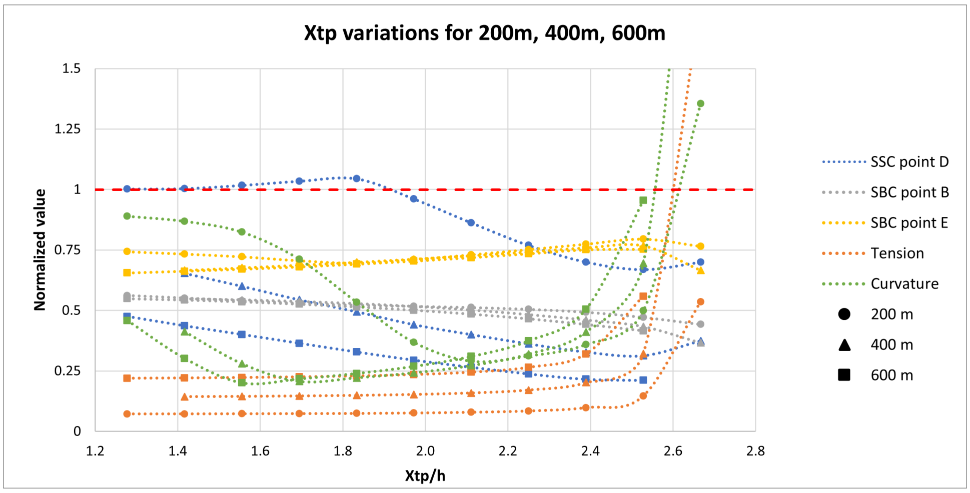

Figure D.8: Normalized evaluation criteria for all tested scenarios of x_{TP} variation at 200m, 400m, 600m water depth

D.3. Additional graphs paramateric study

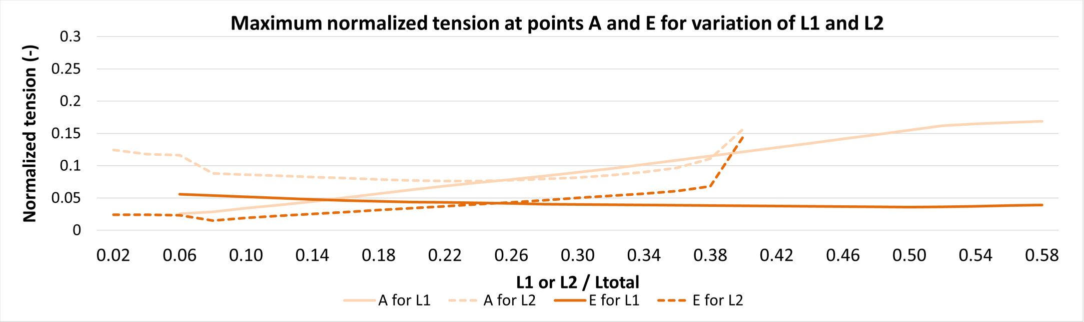

Figure D.9: Tension at point A and E

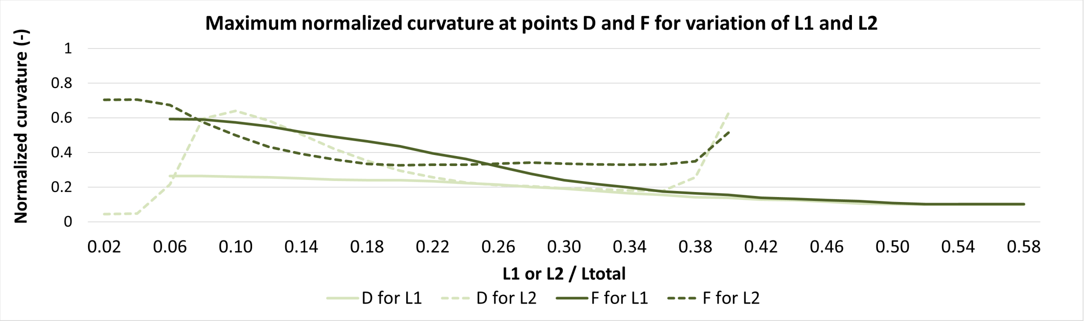

Figure D.10: Curvature at D and F

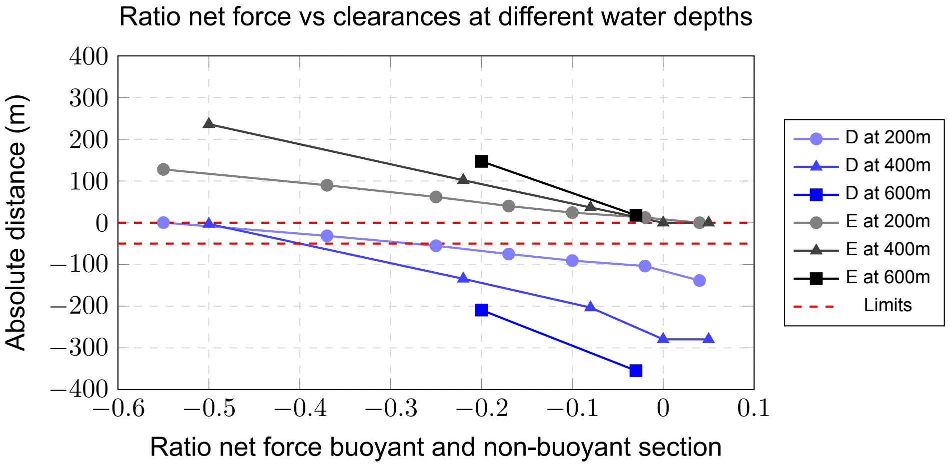

Figure D.11: Ratio net force buoyant and non-buoyant section vs clearances at 200m, 400m, and 600m

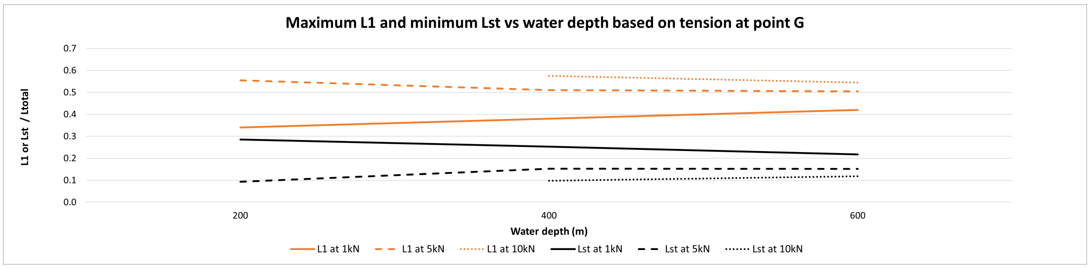

Figure D.12: Tension limits at point G based on L_1 variation across different water depths

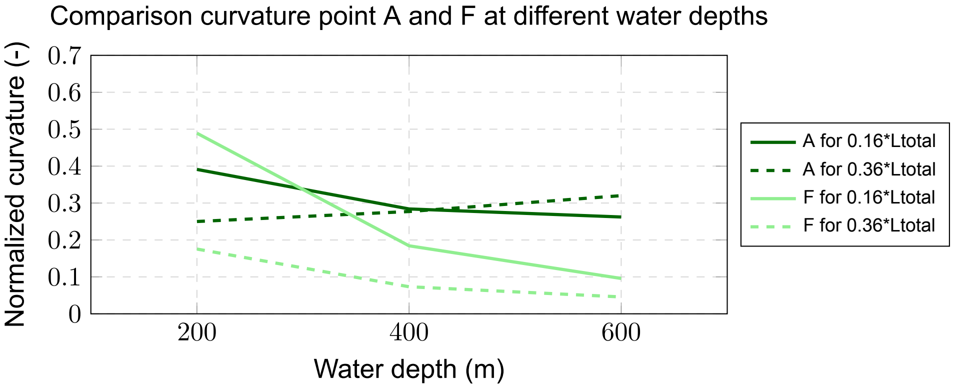

Figure D.13: Comparison of normalized curvature at points A and F for two ratios (0.16 and 0.36) at different water depths for L_1

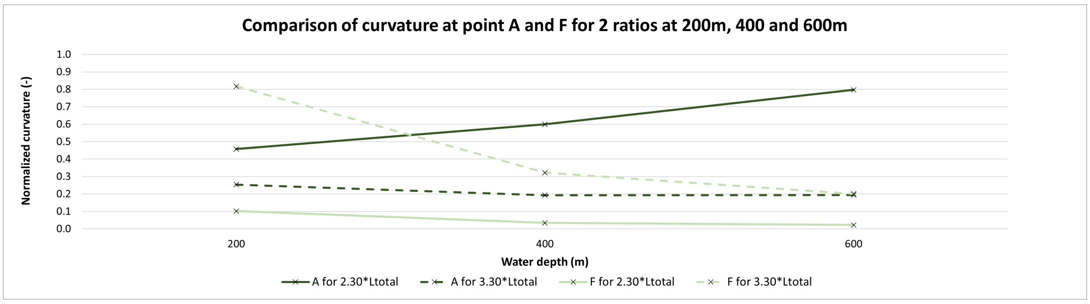

Figure D.14: Comparison and transition from point A and F for three ratios at different water depths for L_{total}

D.4. Failed scenarios

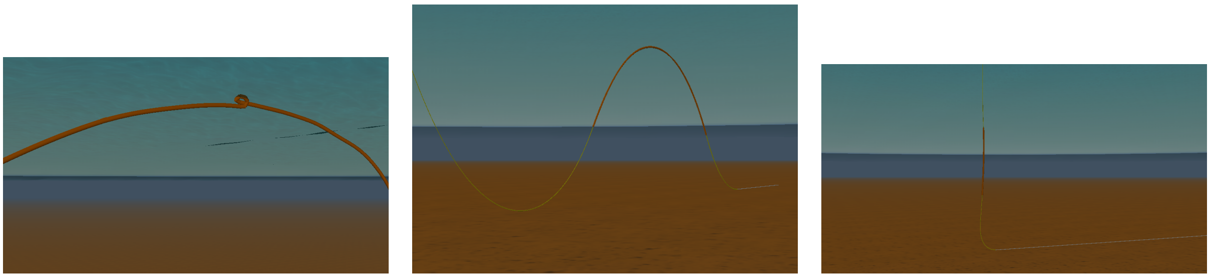

(a) BM reaching sea surface **(b)** BM reaching seabed **(c)** No net buoyancy force

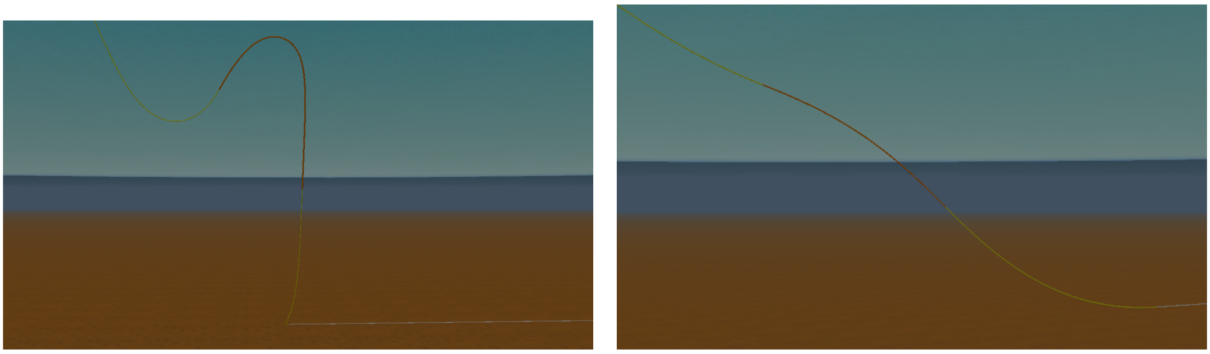

(d) Overbending at TDP **(e)** Over stretching along length

Figure D.15: Failed scenarios from tested scenarios in section 4.3

E

Additional Results Sensitivity

E.1. Base case scenarios

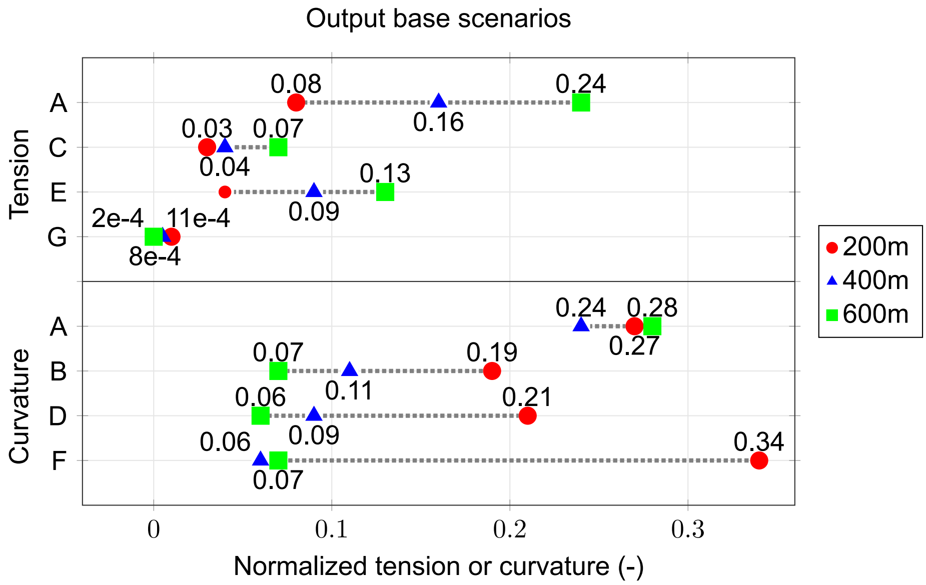

Figure E.1: Values of tension and curvature for the base scenarios at 200m, 400m and 600m depth in dynamic analysis

Table E.1: Data for base value of tension and curvature at 200m, 400m and 600m depth in static and dynamic analysis

(a) Static Analysis

		200	**400**	**600**
Tension	**A**	0.06	0.13	0.20
	C	0.02	0.04	0.06
	E	0.04	0.09	0.13
	G	0.0001	0.0008	0.0002
Curvature	**A**	0.23	0.15	0.17
	B	0.13	0.11	0.07
	D	0.17	0.08	0.05
	F	0.30	0.06	0.07

(b) Dynamic Analysis

		200	**400**	**600**
Tension	**A**	0.08	0.16	0.24
	C	0.03	0.04	0.07
	E	0.04	0.09	0.13
	G	0.00011	0.0008	0.0002
Curvature	**A**	0.28	0.24	0.28
	B	0.19	0.11	0.07
	D	0.21	0.09	0.06
	F	0.34	0.06	0.07

E.2. Static analysis range limits

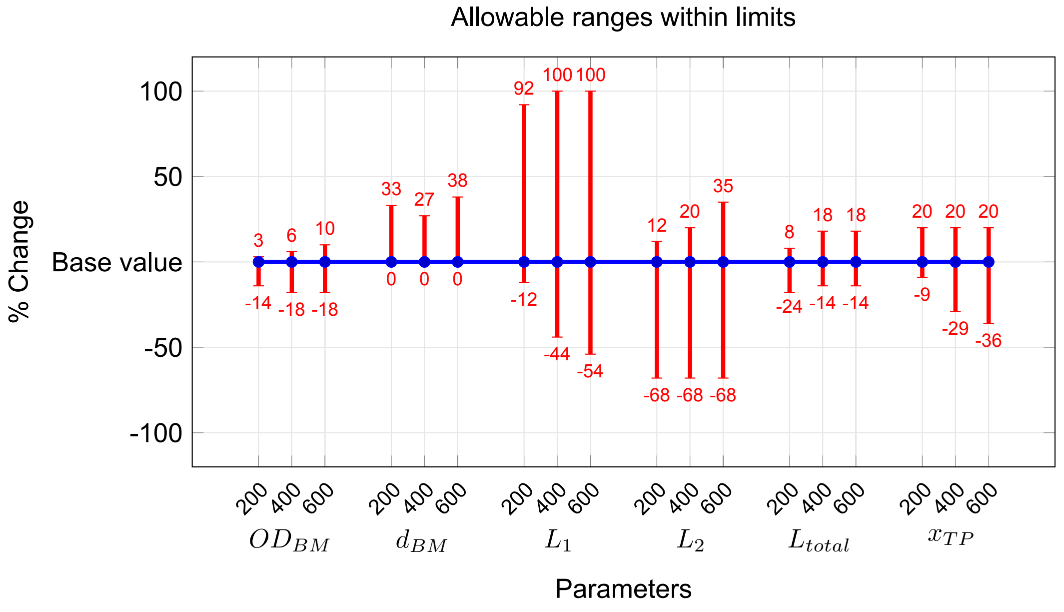

Figure E.2: Plot showing allowable increase or decrease for parameters from its base value at 200m, 400m, and 600m depth in static analysis

Table E.2: Data for whisker plot showing ranges of percentage decrease and increase for each parameter at 200m, 400m, and 600m depth in static and dynamic analysis

	ODBM			**dBM**			**L1**			**L2**			**Ltotal**			**Xtp**		
	200	400	600	200	400	600	200	400	600	200	400	600	200	400	600	200	400	600
Base ratio		4.5		21	44	68		0.25			0.25			2			2.8	
	Static analysis																	
Min. ratio	3.85	3.70	3.70	14	32	42	0.22	0.14	0.12	0.08	0.08	0.08	2.36	2.41	2.41	1.83	1.42	1.28
Max. ratio	4.62	4.78	4.93	21	44	68	0.48	0.50	0.50	0.28	0.30	0.34	3.02	3.30	3.30	2.39	2.39	2.39
	Dynamic analysis																	
Min. ratio	3.85	3.70	3.70	14	32	42	0.22	0.14	0.12	0.08	0.08	0.08	2.36	2.41	2.41	1.83	1.42	1.28
Max. ratio	4.47	4.78	4.93	14	32	42	0.49	0.50	0.52	0.28	0.30	0.34	2.90	3.30	3.30	2.39	2.39	2.39

E.3. Data and heatmaps for 200, 400m and 600m depth

Table E.3: Influence on tension and curvature for a 10% averaged decrease of parameter magnitude at 200, 400m and 600m depth for static and dynamic analysis

		OD_{BM}			d_{BM}			L_1			L_2			L_{total}			x_{TP}		
		200	400	600	200	400	600	200	400	600	200	400	600	200	400	600	200	400	600
		Static analysis																	
Tension	**A**	13	14	14	-4	-4	-3	-12	-10	-11	3	3	3	11	6	5	-5	-4	-4
	C	-55	-49	-53	20	30	25	-7	-8	-8	-19	-15	-15	35	25	14	-15	-12	-6
	E	-51	-59	-55	59	51	124	3	2	2	-8	-8	-9	12	8	6	-8	-6	-4
	G	-47	-76	-73	64	99	62	-36	-34	-40	-26	-33	-28	415	503	558	-72	-54	-41
Curvature	**A**	-29	-35	-37	15	16	23	19	1	-3	-9	-9	-9	17	39	51	-11	-21	-28
	B	96	108	112	-15	-16	-15	1	9	10	21	17	16	-30	-46	-49	32	62	73
	D	4	9	-12	-3	5	10	10	11	11	18	16	16	-45	-50	-50	62	72	75
	F	10	208	92	-8	-14	-8	17	14	12	4	11	14	-55	-47	-47	88	66	68
		Dynamic analysis																	
Tension	**A**	9	12	11	-3	-3	-3	-11	-10	-10	1	2	2	16	9	6	-10	-7	-7
	C	-56	-47	-52	42	46	23	-5	-7	-7	-21	-16	-15	46	28	19	-23	-16	-10
	E	-51	-59	-55	57	51	123	3	2	2	-9	-8	-9	14	12	7	-8	-7	-4
	G	-42	-76	-74	74	95	62	-35	-34	-40	-24	-33	-28	638	514	574	-71	-55	-42
Curvature	**A**	-27	-28	-30	19	15	18	15	-2	-4	-7	-6	-7	16	30	35	-10	-15	-19
	B	90	111	117	-16	-16	-15	7	10	10	19	17	16	-18	-42	-48	25	48	58
	D	6	10	-8	-1	2	4	13	12	12	16	15	14	-25	-43	-45	40	60	65
	F	8	210	90	-4	-14	-8	21	13	12	4	12	15	-50	-46	-47	85	63	65

Table E.4: Influence on tension and curvature for a 10% increase of parameter magnitude at 200, 400m and 600m depth for static and dynamic analysis

		OD_{BM}			d_{BM}			L_1			L_2			L_{total}			x_{TP}		
		200	400	600	200	400	600	200	400	600	200	400	600	200	400	600	200	400	600
		Static analysis																	
Tension	**A**	-11	-11	-10	6	6	5	11	11	11	-3	-3	-2	-6	-4	-4	4	4	4
	C	157	81	94	-13	-27	-17	7	8	8	21	18	18	-15	-12	-9	20	18	9
	E	136	149	125	-31	-25	-26	-2	-2	-2	8	9	9	-9	-7	-6	7	6	4
	G	124	257	256	-38	-31	-23	46	49	72	28	49	43	-82	-83	-77	212	126	72
Curvature	**A**	40	47	49	-14	-14	-16	-12	0	3	10	10	10	-12	-28	-34	10	21	37
	B	-47	-47	-45	29	45	92	-2	-7	-8	-16	-14	-14	35	85	96	-19	-29	-37
	D	-1	-1	13	4	-6	-10	-7	-9	-9	-14	-14	-14	62	99	99	-30	-34	-38
	F	-11	-63	-41	14	34	19	-13	-11	-10	-5	-10	-12	89	88	88	-36	-32	-35
		Dynamic analysis																	
Tension	**A**	-8	-9	-8	2	4	5	10	10	11	-1	-2	-2	-9	-8	-6	9	7	8
	C	147	78	89	-9	-20	-18	6	8	8	24	19	19	-21	-19	-15	28	23	12
	E	133	147	125	-25	-23	-24	-2	-2	-2	9	9	9	-8	-10	-6	8	7	4
	G	100	223	258	-30	-26	-25	44	49	72	25	48	43	-82	-83	-77	195	132	74
Curvature	**A**	30	35	38	-10	-10	-12	-10	2	4	7	7	7	-11	-22	-25	10	14	23
	B	-44	-47	-46	25	39	105	-7	-8	-9	-15	-14	-14	28	73	94	-17	-24	-33
	D	-6	-4	7	3	-2	-6	-10	-10	-10	-13	-13	-12	45	77	84	-25	-29	-32
	F	-10	-63	-40	5	28	24	-14	-11	-10	-5	-10	-13	74	85	87	-35	-31	-34

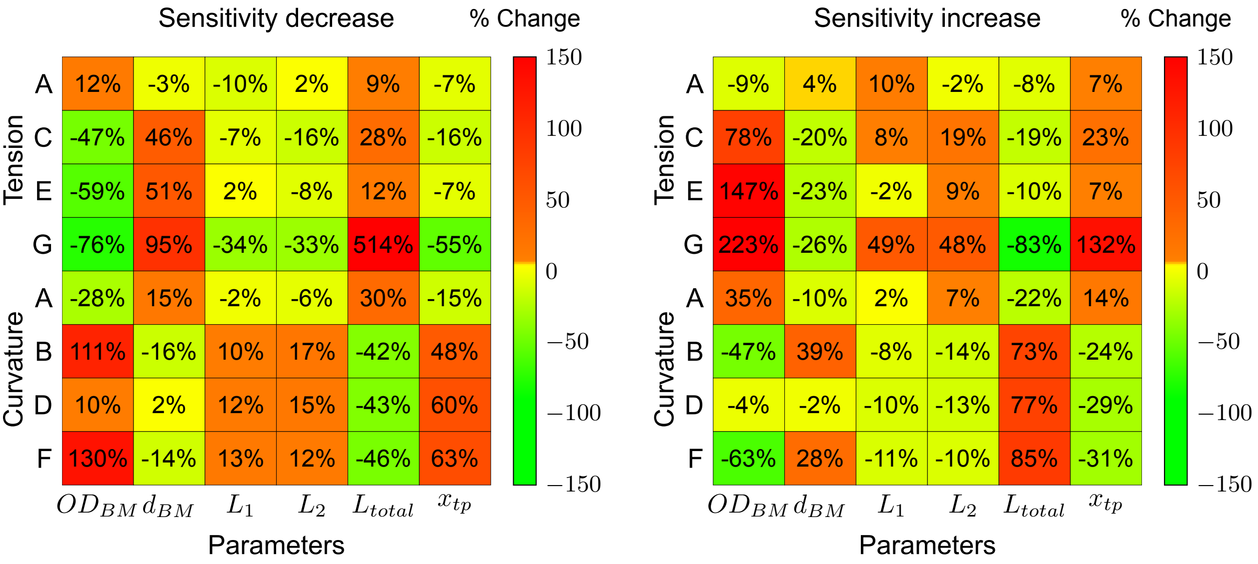

Sensitivity decrease

		OD_{BM}	d_{BM}	L_1	L_2	L_{total}	x_{tp}
Tension	A	12%	-3%	-10%	2%	9%	-7%
	C	-47%	46%	-7%	-16%	28%	-16%
	E	-59%	51%	2%	-8%	12%	-7%
	G	-76%	95%	-34%	-33%	514%	-55%
Curvature	A	-28%	15%	-2%	-6%	30%	-15%
	B	111%	-16%	10%	17%	-42%	48%
	D	10%	2%	12%	15%	-43%	60%
	F	130%	-14%	13%	12%	-46%	63%

Sensitivity increase

		OD_{BM}	d_{BM}	L_1	L_2	L_{total}	x_{tp}
Tension	A	-9%	4%	10%	-2%	-8%	7%
	C	78%	-20%	8%	19%	-19%	23%
	E	147%	-23%	-2%	9%	-10%	7%
	G	223%	-26%	49%	48%	-83%	132%
Curvature	A	35%	-10%	2%	7%	-22%	14%
	B	-47%	39%	-8%	-14%	73%	-24%
	D	-4%	-2%	-10%	-13%	77%	-29%
	F	-63%	28%	-11%	-10%	85%	-31%

(a) Effect on tension and curvature for a 10% decrease of parameter

(b) Effect on tension and curvature for a 10% increase of parameter

Figure E.3: Comparison of heat maps for parameter sensitivity on tension and curvature at 400m depth in dynamic analysis

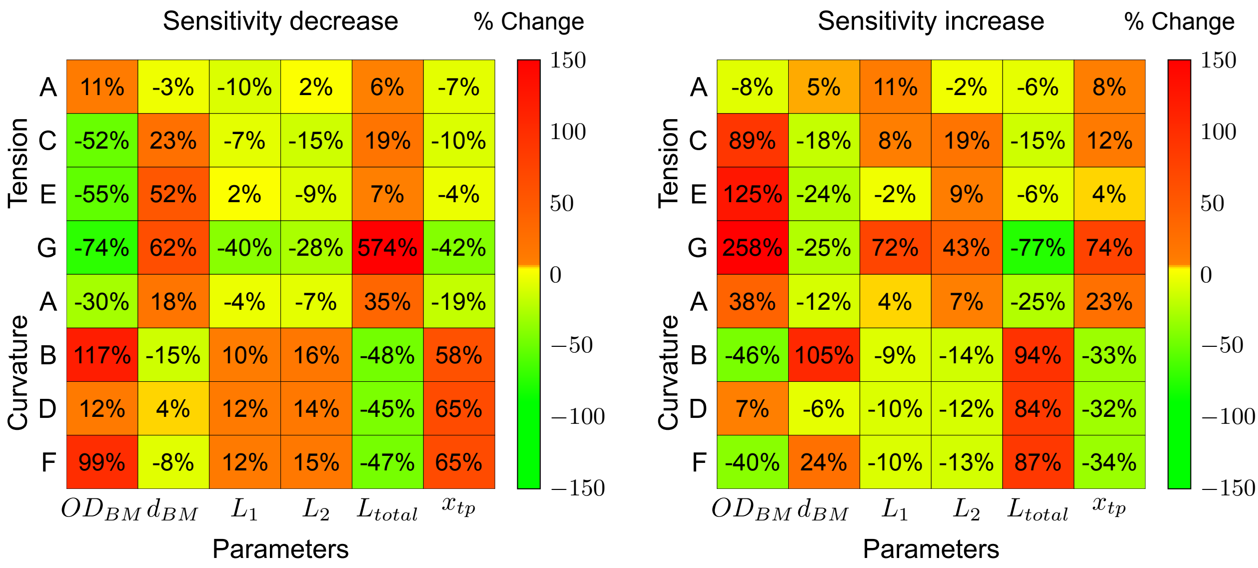

Sensitivity decrease

		OD_{BM}	d_{BM}	L_1	L_2	L_{total}	x_{tp}
Tension	A	11%	-3%	-10%	2%	6%	-7%
	C	-52%	23%	-7%	-15%	19%	-10%
	E	-55%	52%	2%	-9%	7%	-4%
	G	-74%	62%	-40%	-28%	574%	-42%
Curvature	A	-30%	18%	-4%	-7%	35%	-19%
	B	117%	-15%	10%	16%	-48%	58%
	D	12%	4%	12%	14%	-45%	65%
	F	99%	-8%	12%	15%	-47%	65%

Sensitivity increase

		OD_{BM}	d_{BM}	L_1	L_2	L_{total}	x_{tp}
Tension	A	-8%	5%	11%	-2%	-6%	8%
	C	89%	-18%	8%	19%	-15%	12%
	E	125%	-24%	-2%	9%	-6%	4%
	G	258%	-25%	72%	43%	-77%	74%
Curvature	A	38%	-12%	4%	7%	-25%	23%
	B	-46%	105%	-9%	-14%	94%	-33%
	D	7%	-6%	-10%	-12%	84%	-32%
	F	-40%	24%	-10%	-13%	87%	-34%

(a) Effect on tension and curvature for a 10% decrease of parameter

(b) Effect on tension and curvature for a 10% increase of parameter

Figure E.4: Comparison of heat maps for parameter sensitivity on tension and curvature at 600m depth in dynamic analysis